

U

AFTT/DS/ENP/93-04

AD-A273 795
■■■■■■■■■■

DTIC
ELECTE
DEC 16 1993
S E D

SPECTROSCOPIC AND VIBRATIONAL ENERGY
TRANSFER STUDIES IN MOLECULAR BROMINE
DISSERTATION

Courtney D. Holmberg, B.S., M.S.

Captain, USAF

AFTT/DS/ENP/93-04

93-30483
■■■■■■■■■■

Approved for public release; distribution unlimited

93 12 15099

**SPECTROSCOPIC AND VIBRATIONAL ENERGY
TRANSFER STUDIES IN MOLECULAR BROMINE**

DISSERTATION

**Presented to the Faculty of the School of Engineering
of the Air Force Institute of Technology**

Air University

**In Partial Fulfillment of the
Requirements for the Degree of
Doctor of Philosophy**

**Courtney D. Holmberg, B.S., M.S.
Captain, USAF**

August 1993

Approved for public release; distribution unlimited

Accession For	
NTIS	CRA&I
DTIC	TAB
Unannounced	
Justification	
By	
Distribution /	
Availability Codes	
Dist	Avail and / or Special
A-1	

DTIC QUALITY INSPECTED 1

SPECTROSCOPIC AND VIBRATIONAL ENERGY TRANSFER STUDIES IN MOLECULAR BROMINE

Courtney D. Holmberg, B.S., M.S.
Captain, USAF

Approved:

[Handwritten signature]

18 Nov 93

Wm. F. Bailey

18 Nov 93

David Roh

18 Nov 23

Clay V. Lavin

18 Nov 93

Ernest G Parks

15 NOV 23

Accepted:

Bob + Helen L

Dean, School of Engineering

Preface

The study of the spectroscopy and kinetics of molecular bromine has been both interesting and rewarding. Having the opportunity to conduct the independent research for this paper has provided me with experimental skills and technical insight that cannot be mastered in a classroom alone. However, without the extensive assistance of several important people during the course of this work, this dissertation would not have been possible. I would first like to thank my advisor, Maj Glen Perram, to whom I am deeply indebted for proposing the topic and having the confidence in me to allow me to attempt it. His knowledge of the theoretical background and experimental techniques needed for this project were invaluable. His accessibility, patience and friendship were greatly appreciated. I also wish to thank Mr. Bill Evans and his laboratory support staff for helping to keep the experimental apparatus running. In particular Mr. Jim Reynolds was of considerable help during the build-up of the experimental apparatus and computer diagnostics. I also thank Mr. Mike Ray of the Wright Labs for contributing his glass blowing expertise. I want to also thank Capts Ray Johnson and Brian Minor for their friendship and computer expertise, especially during the writing of this dissertation. I especially thank my God for the ability, motivation and endurance He provided during this project. Finally, I thank my wife Connie and my children, Dustin, Andrew and Brianne. Were it not for their continued love and support this work would certainly have not been successful.

Courtney D. Holmberg

Table of Contents

Preface.....	ii
List of Figures.....	vii
List of Tables.....	xiv
List of Symbols.....	xv
Abstract.....	xvii
I. Introduction.....	1
1. Overview.....	1
2. Halogens and Interhalogens.....	2
3. Bromine.....	5
4. Problem Statement.....	10
5. Organization.....	11
II. Background Theory.....	11
1. Molecular Theory.....	11
1.1 Halogen and Interhalogen Structure.....	11
1.2 Hund's Cases.....	12
1.3 Predissociation.....	15
1.4 Spectroscopy of Bromine.....	17
2. Laser Induced Fluorescence.....	19
3. Kinetic Analysis.....	22
3.1 Energy Transfer Processes.....	23
3.2 Master Rate Equation.....	28
3.3 Time-Dependent Solutions.....	29

3.3.1 Electronic Quenching / Total Removal	29
3.3.2 Vibrational Transfer.....	31
3.3.2.1 Low Pressure / Radioactive Decay	
Approximation	31
3.3.2.2 The Montroll-Shuler Model.....	33
4. Experimental Approach.....	35
4.1 Laser Excitation Spectra.....	35
4.2 Emission Spectra.....	37
4.3 Spectrally Resolved, Temporally Resolved	
Fluorescence	37
III. Spectroscopy of High v'' Levels in $\text{Br}_2(\text{X})$	38
1. Introduction.....	38
2. Experimental Setup.....	40
2.1 Spectroscopic Experiment.....	42
3. Laser Excitation Spectra	43
4. Experimental Results and Discussion	46
IV. Vibrational Energy Transfer in $\text{Br}_2 \text{ B}^3\Pi(0_u^+)$	59
1 Introduction.....	59
2 Experimental Arrangement.....	60
2.1 Isotopically Enriched Br_2 and Gas Handling	60
2.2 Excitation System	61
2.3 Detection System.....	61
3 Experimental Procedures	62
4 Experimental Results	66
4.1 Laser Excitation Spectra.....	66
4.2 $\text{V} \rightarrow \text{T}$ Transfer With $\text{Br}_2(\text{X})$ as Collision Partner.....	68

4.2.1	Montroll-Shuler Fits.....	75
4.2.2	Total Removal from Initially Excited Levels.....	75
4.2.3	Stern-Volmer Analysis of Montroll-Shuler Data.....	82
4.3	V→T Transfer With Rare Gas Collision Partners	88
4.3.1	Argon.....	89
4.3.2	Helium, Neon, Krypton and Xenon	90
5	Discussion of Br ₂ (B) Vibrational Transfer Results	91
5.1	Validity of Montroll-Shuler Model for Br ₂	92
5.2	Deficiencies of the Montroll-Shuler Model for Br ₂	94
5.3	V→T Scaling Theories.....	109
5.4	Uniqueness of Solution	114
5.4.1	Double Exponential Fits.....	116
5.4.2	Analysis of the Double Exponential Fits.....	117
5.5	Comparisons with Previous Studies.....	123
V.	Conclusions.....	127
1	Summary of Spectroscopy of High v" Levels in Br ₂ (X)	127
2	Summary of Collisional Energy Transfer Studies in Br(B)	128
3	Further Studies.....	129
	Bibliography.....	131
	Appendix A. Br ₂ Spectroscopy	136
1	Spectroscopic Constants	136
2	Franck-Condon Factors	136
	Appendix B. Basic Energy Transfer Theories	141
1	Gas Kinetic Collision Rates.....	141
2	Landau Teller Theory.....	142

3 SSH Theory	143
4 Montroll-Shuler Model	145
5 Montroll-Shuler Model TableCurve Implementation	146
6 Development of the Eigenvalue Solution to a Five-level Montroll-Shuler System	148
Appendix C. Experimental Calibrations and Calculations	152
1 Monochromator Resolution.....	152
2 Spectral Overlap Calculations.....	152
Appendix D. Rare Gas Vibrational Transfer Data.....	155
Appendix E. Systematic Error	172
Vita	174

List of Figures

1	Ground state diatomic halogen electronic configuration	12
2	Hund's cases correlation diagram	14
3	Br ₂ potential energy curves	16
4	Simplified representation of laser induced fluorescence from collisionally populated satellite states	22
5	Example of pulsed laser induced fluorescence technique	23
6	Block diagram of the experimental apparatus	40
7	Low resolution laser excitation spectra using Rhodamine 575 dye.....	44
8	High resolution laser excitation spectra using Rhodamine 575 dye	45
9	Emission spectra from $v' = 16$ and 17	48
10	Emission spectra from $v' = 18$ and 19	49
11	LIF intensity versus wavelength near the (16,6) bandhead of ⁷⁹ Br ⁸¹ Br	50
12	Plot of experimentally obtained second-differences and calculated values	56
13	Vibrational transfer emission spectrum	63
14	Total fluorescence excitation spectrum for LDS 698	67
15	Vibrationally resolved excitation spectra for $v' = 3$	69
16	Vibrationally resolved excitation spectra for $v' = 2$	70
17	Vibrationally resolved excitation spectra for $v' = 1$	71
18	Spectrally, temporally resolved fluorescence profile for $v' = 2$	73
19	Spectrally resolved, temporally resolved fluorescence profiles for $v' = 1$ and 3	74

20	Montroll-Shuler fit to emissions from the (2-13) band transition after initial excitation of $v'=3$ with a Br_2 pressure of 1.68 Torr.....	76
21	Montroll-Shuler fit to emissions from the (2-11) band transition after initial excitation of $v'=3$ with a Br_2 pressure of 724 mTorr	77
22	Montroll-Shuler fit to emissions from the (3-9) band transition after initial excitation of $v'=2$ with a Br_2 pressure of 1.97 Torr.....	78
23	Montroll-Shuler fit to emissions from the (3-9) band transition after initial excitation of $v'=2$ with a Br_2 pressure of 660 mTorr	79
24	Montroll-Shuler fit to emissions from the (1-13) band transition after initial excitation of $v'=2$ with a Br_2 pressure of 2.06 Torr.....	80
25	Montroll-Shuler fit to emissions from the (1-13) band transition after initial excitation of $v'=2$ with a Br_2 pressure of 780 mTorr	81
26	Single exponential decay fit to emissions from $v' = 3$ parent state for Br_2 pressure of 656 mTorr	83
27	Double exponential decay fit to emissions from $v' = 2$ parent state for Br_2 pressure of 576 mTorr	84
28	Stern-Volmer plot of the Montroll-Shuler vibrational transfer fits to the combined p3v2 data with $\text{Br}_2(\text{X})$ collision partner.....	85
29	Stern-Volmer plot of the Montroll-Shuler electronic removal fits to the combined p3v2 data with $\text{Br}_2(\text{X})$ collision partner.....	86
30	Stern-Volmer $\text{V} \rightarrow \text{T}$ transfer plots for five level, seven level and Montroll-Shuler models for p3v2, Br_2 collision partner data	98
31	Stern-Volmer electronic removal plots for five level, seven level and Montroll-Shuler models for p3v2, Br_2 collision partner data	99

32	Montroll-Shuler, seven level, six level, five level, and four level model fits to p3v2 data with 1.7 Torr argon	100
33	Montroll-Shuler (1), seven level (2), six level (3), five level (4), and four level (5) model fits to p3v2 data with 1.7 Torr argon	101
34	Stern-Volmer vibrational transfer plots for four level, five level, six level, seven level and Montroll-Shuler model fits to p3v2 data with 1.7 Torr argon	103
35	Stern-Volmer electronic removal plots for four level, five level, six level, seven level and Montroll-Shuler model fits to p3v2 data with 1.7 Torr argon	104
36	Four level system and seven level system with state-dependent electronic removal rates fits to p3v2 data in argon	108
37	Vibrational transfer probabilities for Br ₂ , BrCl, BrF and IF with rare gas collision partners	111
38	Interaction length as a function of collision pair reduced mass for Br ₂ , IF, BrF and BrCl with rare gas collision partners.....	113
39	Vibrational transfer probabilities ($\Delta v = -1$) for halogen and interhalogen collisions with argon as a function of the diatomic vibrational energy spacing to the 2/3 power	115
40	Vibrational transfer probabilities ($\Delta v = -1$) for Br ₂ and rare gas collision partners.....	115
41	Double exponential fit to emissions from the (2-13) band after excitation of $v'=3$ with a Br ₂ pressure of 1.68 Torr	118
42	Double exponential fit to the emissions from the (2-13) band after excitation of $v'=3$ with a Br ₂ pressure of 724 mTorr	119

43	Stern-Volmer plots for double exponential fits to the emissions from the (2-13) band after excitation of $v'=3$	120
C.1	Spectral resolution of the ISA HR-640 0.64 m monochromator.....	153
D.1	Montroll-Shuler fit to emissions from the (2-11) band transition after excitation of $v'=3$ with 540 mTorr of Br_2 and 440 mTorr of Argon	156
D.2	Montroll-Shuler fit to emissions from the (2-11) band transition after excitation of $v'=3$ with 540 mTorr of Br_2 and 3.4 Torr of Argon	156
D.3	Montroll-Shuler fit to emissions from the (1-12) band transition after excitation of $v'=2$ with a 790 mTorr of Br_2 and 300 mTorr of Argon	157
D.4	Montroll-Shuler fit to emissions from the (1-12) band transition after excitation of $v'=2$ with 790 mTorr of Br_2 and 1.8 Torr of Argon	157
D.5	Montroll-Shuler fit to emissions from the (3-9) band transition after excitation of $v'=2$ with 810 mTorr of Br_2 and 330 mTorr Argon	158
D.6	Montroll-Shuler fit to emissions from the (3-9) band transition after excitation of $v'=2$ with 810 mTorr of Br_2 and 3.1 Torr of Argon	158
D.7	Stern-Volmer plot of the Montroll-Shuler vibrational transfer fits to the combined pump $v'=3$ view $v'=2$ data with Argon buffer gas	159
D.8	Stern-Volmer plot of the Montroll-Shuler vibrational transfer fits to the combined pump $v'=2$ view $v'=1$ data with Argon buffer gas	159

D.9 Stern-Volmer plot of the Montroll-Shuler vibrational transfer fits to the combined pump $v'=2$ view $v'=3$ data with Argon buffer.....	160
D.10 Stern-Volmer plot of the Montroll-Shuler electronic quenching fits to the combined pump $v'=3$ view $v'=2$ data with Argon buffer gas	160
D.11 Montroll-Shuler fit to emissions from the (2-11) band transition after initial excitation of $v' = 3$ with a Br_2 pressure of 650 mTorr and 560 mTorr of Helium	161
D.12 Montroll-Shuler fit to emissions from the (2-11) band transition after initial excitation of $v' = 3$ with a Br_2 pressure of 650 mTorr and 2.1 Torr of Helium.....	161
D.13 Stern-Volmer plot of the Montroll-Shuler vibrational transfer fits to the combined pump $v' = 3$ view $v' = 2$ data with Helium buffer	162
D.14 Stern-Volmer plot of the Montroll-Shuler electronic quenching fits to the combined pump $v' = 3$ view $v' = 2$ data with Helium buffer gas	162
D.15 Montroll-Shuler fit to emissions from the (2-11) band transition after initial excitation of $v' = 3$ with a Br_2 pressure of 700 mTorr and 360 mTorr of Neon	163
D.16 Montroll-Shuler fit to emissions from the (2-11) band transition after initial excitation of $v' = 3$ with a Br_2 pressure of 700 mTorr and 2.4 Torr of Neon	163
D.17 Stern-Volmer plot of the Montroll-Shuler vibrational transfer fits to the combined pump $v' = 3$ view $v' = 2$ data with Neon buffer gas	164
D.18 Stern-Volmer plot of the Montroll-Shuler electronic quenching fits to the combined pump $v' = 3$ view $v' = 2$ data with Neon buffer.....	164

D.19 Montroll-Shuler fit to emissions from the (2-11) band transition after initial excitation of $v' = 3$ with a Br ₂ pressure of 640 mTorr and 410 mTorr of Krypton	165
D.20 Montroll-Shuler fit to emissions from the (2-11) band transition after initial excitation of $v' = 3$ with a Br ₂ pressure of 640 mTorr and 2.3 Torr of Krypton	165
D.21 Stern-Volmer plot of the Montroll-Shuler vibrational transfer fits to the pump $v'=3$ view $v'=2$ data with Krypton buffer gas	166
D.22 Stern-Volmer plot of the Montroll-Shuler electronic removal fits to the pump $v'=3$ view $v'=1$ data with Krypton buffer gas	166
D.23 Montroll-Shuler fit to emissions from the (2-11) band transition after initial excitation of $v' = 3$ with a Br ₂ pressure of 420 mTorr and 500 mTorr of Xenon	167
D.24 Montroll-Shuler fit to emissions from the (2-11) band transition after initial excitation of $v' = 3$ with a Br ₂ pressure of 420 mTorr and 2.3 Torr of Xenon	167
D.25 Stern-Volmer plot of the Montroll-Shuler vibrational transfer fits to the pump $v'=3$ view $v'=2$ data with Xenon buffer gas	168
D.26 Stern-Volmer plot of the Montroll-Shuler electronic removal fits to the pump $v'=3$ view $v'=1$ data with Xenon buffer gas	168
D.27 Montroll-Shuler fit to emissions from the (2-11) band transition after initial excitation of $v' = 3$ with a Br ₂ pressure of 650 mTorr and 2.1 Torr of Helium.....	169
D.28 Montroll-Shuler fit to emissions from the (2-11) band transition after initial excitation of $v' = 3$ with a Br ₂ pressure of 700 mTorr and 2.4 Torr of Neon	169

D.29 Montroll-Shuler fit to emissions from the (2-11) band transition after initial excitation of $v' = 3$ with a Br ₂ pressure of 540 mTorr and 3.4 Torr of Argon	170
D.30 Montroll-Shuler fit to emissions from the (2-11) band transition after initial excitation of $v' = 3$ with a Br ₂ pressure of 640 mTorr and 2.3 Torr of Krypton	170
D.31 Montroll-Shuler fit to emissions from the (2-11) band transition after initial excitation of $v' = 3$ with a Br ₂ pressure of 420 mTorr and 2.3 Torr of Xenon	171

List of Tables

1	Dye laser excitation wavelengths	46
2	Observed Br ₂ bandhead assignments for the B→X Transitions.....	51
3	Spectroscopic Constants for the ⁷⁹ Br ⁸¹ Br Ground State	57
4	RKR Potential Energies and Turning Points.....	58
5	Spectral overlap fractions and observation wavelengths.....	64
6	Rate coefficients for collisions with Br ₂	88
7	Rate coefficients for collisions with argon.....	90
8	Rate coefficients for rare gas collision partners.....	91
9	Summary of collisional transfer rate coefficients	92
10	Rate coefficients for n-level systems.....	105
11	Double exponential fit rate coefficients.....	121
A.1	Bromine molecular constants	137
A.2	Term values for Br ₂ ground state.....	138
A.3	Franck-Condon factors.....	140
B.1	Br ₂ gas kinetic collision parameters	143

List of Symbols

v', J'	Vibrational and rotational quantum levels for electronically excited molecules
v'', J''	Vibrational and rotational quantum levels for ground state molecules
$R, V \rightarrow T$	Collisional transfer of rotational or vibrational energy into translational energy
$V \rightarrow V$	Collisional transfer of vibrational energy from one collision species to another
μ	Collision pair reduced mass
Δv	Change in vibrational quantum number due to collisions
k_B	Boltzmann's constant
T	Temperature
$X^1\Sigma_g^+$	Molecular term symbol for the ground electronic state in the diatomic halogens
$B^3\Pi(0_u^+)$	Molecular term symbol for the electronically excited B state in the diatomic halogens
$1/\tau_r$	Collisionless radiative lifetime from an excited electronic state
k_v	Vibrational level dependent rate coefficient for predissociation from an excited electronic state
$^2P_{3/2}$	Atomic term symbol for ground state halogen atoms
$^2P_{1/2}$	Atomic term symbol for first excited state of halogen atoms
$B \rightarrow X$	Electronic transition from the electronically excited B state to the ground X state
LIF	Laser induced fluorescence
$\delta_{v v_0}$	Kronecker delta function
$\tau_{TR}(p)$	Lifetime for total population removal from quantum level p

$k_V^Y(1,0)$	Fundamental V→T transfer rate coefficient for collision species Y
k_q^Y	Electronic quenching rate coefficient for collision species Y
$x_p(t)$	Normalized time-dependent population distribution of quantum state p
$\omega_e/k_B T$	Vibrational energy spacing with respect to average thermal energy at temperature T
$\Delta G_{v''}$	Difference in energy between two adjacent vibrational levels in a ground electronic state molecule
(v', v'')	Electronic transition between excited state vibrational level v' and ground state vibrational level v''
$p(a)v(b)$	Notation for experimental procedure where the $v' = a$ is the initially excited state vibrational level and $v' = b$ is the observed excited state vibrational level
Γ_v	Fundamental vibrational transfer rate obtained as a fit parameter from the Montroll-Shuler model
Γ_0	Electronic removal rate from and excited electronic state; obtained as a fit parameter from the Montroll-Shuler model
$\sigma_v(1,0)$	Thermally averaged fundamental vibrational transfer cross section
σ_g	Thermally averaged gas kinetic cross section
P_{10}	Fundamental probability of vibrational transfer from $v' = 1$ to $v' = 0$; experimentally equivalent to $\sigma_v(1,0)/\sigma_g$
L	Characteristic interaction length between collision partners

Abstract

The spectroscopy of high vibrational levels in the $^{79}\text{Br}^{81}\text{Br } X^1\Sigma_g^+$ ground electronic state was investigated using spectrally resolved, pulsed laser induced fluorescence from low J' levels in the $B^3\Pi(0_u^+)$ state. Over 100 bandheads were identified for transitions from $15 \leq v' \leq 21$ to $1 \leq v'' \leq 27$. The calculated spectroscopic constants, $\omega_e'' = 323.1 \pm 1.5 \text{ cm}^{-1}$, $\omega_e\chi_e'' = 1.02 \pm 0.1 \text{ cm}^{-1}$ and $\omega_e y_e'' = -3.77 \pm 0.2 \times 10^{-3} \text{ cm}^{-1}$, are valid for $v'' \leq 27$.

Vibrational transfer and electronic quenching in the lower vibrational levels ($v' \leq 3$) of the $B^3\Pi(0_u^+)$ state of $^{79}\text{Br}_2$ were investigated using spectrally resolved, temporally resolved laser induced fluorescence techniques. Spectrally resolved emissions from collisionally populated $\text{Br}_2(B)$ vibrational levels were observed for Br_2 and rare gas collision partners. Vibrational transfer was efficient in the non-predissociative vibrational levels and was adequately described by the Montroll-Shuler model for harmonic oscillators. A single fundamental rate coefficient for vibrational transfer from $v' = 1$ to $v' = 0$, $k_v(1,0)$, is used to characterize vibrational relaxation. For Br_2 , the value was $k_v(1,0) = 3.6 \pm 0.4 \times 10^{-11} \text{ cm}^3/\text{molec}\cdot\text{sec}$. Rate coefficients were slightly lower for rare gas collisions, ranging from $k_v(1,0) = 2.5 \pm 0.3 \times 10^{-11} \text{ cm}^3/\text{molec}\cdot\text{sec}$ for helium to $k_v(1,0) = 3.1 \pm 0.4 \times 10^{-11} \text{ cm}^3/\text{molec}\cdot\text{sec}$ for xenon. Electronic quenching rates for the observed vibrational levels were obtained from the same data. For Br_2 , the quenching rate coefficient was $k_q = 3.7 \pm 1.2 \times 10^{-11} \text{ cm}^3/\text{molec}\cdot\text{sec}$. The quenching rate coefficients for the rare gases were smaller, $k_q = 8.0 \pm 1.2 \times 10^{-12} \text{ cm}^3/\text{molec}\cdot\text{sec}$.

Spectroscopic and Vibrational Energy Transfer Studies in Molecular Bromine

I. Introduction

1. Overview

Collisional energy transfer in electronically excited bound states of diatomic molecules and free radicals is an area of continuing interest (10). The development of narrow linewidth, tunable pulsed or CW lasers has greatly facilitated these studies by allowing excitation of single rovibrational states (v' , J') in electronically excited molecules. Fluorescence from these electronically excited, rovibrational energy levels can be spectrally and/or temporally resolved and used to investigate molecular energy level structure for both ground and excited states, excited state radiative lifetimes (τ_r), collisional energy transfer rate coefficients (k 's) and cross sections (σ 's) for rovibrational-translational (R,V \rightarrow T) transfer, vibrational-vibrational (V \rightarrow V) transfer and electronic quenching of the parent molecule. For example, the dependence of collisional energy transfer rates on initially populated quantum states (v' , J') has been well characterized for both Na₂ and Li₂ (10). Other similar studies have been accomplished for NO A²Σ⁺, OH A²Σ⁺, I₂ B³Π(0_u⁺), HD B¹Σ⁺, and S₂ B³Σ_u⁻ (10).

The choice of molecules available for this type of study is limited by both the spectral characteristics of the pump laser and the absorption and emission characteristics of the target molecule. Tunable dye lasers allow excitation wavelengths from the ultraviolet to near infrared. Target molecules must also absorb the laser radiation and re-emit a sufficient number of photons within the response range of the detection system, usually the visible or near infrared, to overcome low signal-to-noise ratios. In general, the diatomic halogens and interhalogens fit these criteria well.

2. Halogens and Interhalogens

Both the spectroscopy and kinetics of the diatomic halogens and interhalogens have been investigated for many years (17). Interest stems from the various energy transfer mechanisms occurring in this class of molecule. A great deal of the work accomplished has been driven by the potential of the diatomic halogens and interhalogens as chemically pumped, electronic transition, visible laser sources (33). These studies are quite varied and include many experimental techniques: absorption spectroscopy, chemiluminescence, laser induced fluorescence (LIF), optical pumping, and laser demonstrations. Perram's work (32) includes an excellent bibliography of these various studies.

The diatomic halogens and interhalogens have several interesting features that make them attractive as possible visible chemical lasers (32). Several possible chemical pumping schemes exist for pumping the B-states of I_2 , Br_2 , Cl_2 , IF , BrF and $BrCl$ (14). In addition, the equilibrium internuclear spacing of the electronically excited B-state is much larger than that of the

ground state. The difference in internuclear spacing, along with the Franck-Condon principle, dictates essentially vertical electronic transitions from low lying excited state vibrational levels to higher lying, sparsely populated ground state vibrational levels. For pulsed excitation systems, establishment of the population inversion needed for lasing is virtually guaranteed in the halogens. Finally, the relatively long radiative lifetimes of the halogens and interhalogens (0.2 - 80 μ sec) and low electronic quenching rates (10^{-14} - 10^{-10} $\text{cm}^3/\text{molec-sec}$) are also important for maintaining population inversion (14). Pulsed and CW optically pumped B \rightarrow X lasers have been demonstrated in I_2 (3), Br_2 (33, 45) and IF (14, 16).

Chemically pumped electronic transition lasers use exothermic chemical reactions to provide the energy needed to populate the upper laser electronic state. This can be accomplished through either direct excitation of the lasant species, such as in the HF laser, or via collisional energy transfer to the lasant species from a metastable species, such as in the Chemical Oxygen-Iodine Laser (COIL). In diatomic or polyatomic molecules, the excited state population induced by the chemical reaction may be distributed in a highly non-thermal manner over many possible rovibrational levels. Therefore, a good lasant molecule should thermalize rapidly without losing electronic excitation. Therefore, when choosing potential laser candidates, it is important to know not only the transition probabilities and energies from a spectroscopic viewpoint but also understand the important collisional energy transfer mechanisms that may be involved.

Of more general scientific interest is the extent to which collisional energy transfer in the diatomic halogens and interhalogens follow currently accepted energy transfer models. Two relatively simple collisional energy

transfer theories are the Landau-Teller (L-T) (23) and Schwartz, Slawsky and Herzfeld (SSH) (37) theories. The SSH theory uses time-dependent perturbation theory to calculate the probability of a collisional energy transfer process taking an harmonic oscillator from an initial state i to a final state j . Both theories assume weak interactions and single quantum level vibrational transitions. The SSH theory predicts that the probability for vibrational transfer should scale with reduced mass of the collision partners, μ , as $\approx A \exp(-B\mu^{1/3})$. In studies involving diatomic halogens and interhalogens with rare gas collision partners, it is interesting to note that while IF(B) (46) and BrF(B) (29,35) V→T transfer rates both exhibit the $\mu^{1/3}$ reduced mass dependence, both I₂(B) (42, 30) and BrCl(B) (32) V→T transfer rates deviate significantly from this dependence. The differences in reduced mass dependence for the various interhalogens have been related to the degree to which the assumption of only single quantum vibrational transitions occurring ($\Delta v = \pm 1$) is valid. In IF(B) and BrF(B), the vibrational energy spacings are relatively large compared to $k_B T$ (400 cm⁻¹ and 372 cm⁻¹, respectively) (29); implying multi-quantum transfer is unlikely. In I₂(B) and BrCl(B), the spacings are much smaller (128 and 200 cm⁻¹, respectively) (32) and multi-quantum transfer is more probable. In Br₂(B), the vibrational energy spacing is between that of I₂ and BrCl so the $\mu^{1/3}$ dependence would not be expected in Br₂.

3. Bromine

While an optically pumped Br₂ laser has been demonstrated (33), the presence of an extremely strong predissociation in vibrational levels above

$v' \geq 4$ in the $\text{Br}_2 \text{ B } ^3\Pi(0_u^+)$ state eliminates it from serious consideration as an efficient laser molecule. Other considerations, most notably the relatively small rotational and vibrational spacings within the $\text{Br}_2(\text{B})$ state, spontaneous predissociation and strong absorption and emission in the visible and near IR region, make Br_2 an excellent subject for the study of collisional energy transfer within a strongly coupled system, i.e., where energy level spacings are $\leq k_B T$.

A wealth of spectroscopic data on $\text{Br}_2 (\text{B} \rightarrow \text{X})$ transition has been obtained through the years. Clearly, the most thorough study to date was the high resolution absorption work performed by Barrow, et. al. (2) and the complementary work by Coxon (11), which yielded rotationally resolved spectroscopic data over the range $0 \leq v'' \leq 10$ in the $\text{Br}_2 \text{ X } ^1\Sigma_g^+$ ground state and nearly all of the bound vibrational levels $0 \leq v' \leq 55$ of the $\text{Br}_2 \text{ B } ^3\Pi(0_u^+)$ state of the $^{79}\text{Br}_2$ and $^{81}\text{Br}_2$ isotopes. An extensive set of rotational and vibrational term values for $^{79}\text{Br}_2$ and $^{81}\text{Br}_2$ and calculated molecular constants for the $^{79}\text{Br}^{81}\text{Br}$ isotope were also reported (2). Barrow's absorption work provides the best recorded spectroscopic constants, potential energy curves and Franck-Condon factors currently available.

Several studies investigating radiative and collisional processes in the $\text{Br}_2 \text{ B } ^3\Pi(0_u^+)$ state have been undertaken using laser induced fluorescence (LIF) techniques. McAfee and Hozack observed spectrally resolved fluorescence from several rovibrational levels near the $\text{Br}_2(\text{B})$ dissociation limit as a function of Br_2 pressure using an opto-acoustically chopped Ar^+ laser excitation source. They reported collision-free lifetimes that decreased as the energy of the levels increased and quenching cross sections that increased as the dissociation limit was approached (27). They also reported observation of

fluorescence from collisionally populated states, but did not report any state-to-state transfer rates. Systematic lifetime studies performed by Clyne and Heaven (1984) for various J' levels in $v' = 11, 14, 19, 20, 23$ and 24 confirmed the existence of a rotationally dependent predissociation. Clyne, Heaven and Martinez also conducted similar studies for $v' = 2$ (8) and $v' = 3, 4, 5$ and 7 (9). In each of these studies, single rovibrational levels of $\text{Br}_2(\text{B})$ were excited using narrow linewidth, pulsed dye lasers. Unresolved fluorescence decay time profiles were collected as a function of v' , J' and test cell pressure. Inverse lifetimes were plotted as a function of $J'(J'+1)$ and fit to the equation

$$\frac{1}{\tau_o} = \frac{1}{\tau_r} + k_{v'} J'(J'+1) \quad (1)$$

where τ_o is the measured exponential decay lifetime, τ_r is the rotationless radiative lifetime and $k_{v'}$ is the predissociative decay rate coefficient (1984, 8). All vibrational levels $v' \geq 3$ fit Eq (1) quite satisfactorily. Of the vibrational levels studied by Clyne and coworkers, only $v' = 2$ was found to be totally free of the rotational dependence in Eq (1) (8). The measured predissociation rate coefficient for $v' = 3$ was two orders of magnitude smaller than for any other v' level and was therefore considered to be stable for the current study. Rovibrational level dependent quenching rates were also reported in the studies above. Clyne, Heaven and Tellinghuisen (9) determined through iterative Franck-Condon factor calculations that the predissociation was induced by a crossing of the $^3\Pi(0_u^+)$ curve by a $^1\Pi_u$ repulsive state between $v' = 4$ and $v' = 5$. Using experimental results from the works of Clyne and coworkers just described, they were able to derive the parameters of a simple repulsive curve representing the $^1\Pi_u$ repulsive state. Their results also

provided a quantitative description for anomalous isotopic predissociation observed for the $v' = 7$ level.

Other studies have also investigated radiative lifetimes and electronic quenching rates of $\text{Br}_2(\text{B})$ with $\text{Br}_2(\text{X})$, He, N_2 , and the rare gases as collision partners (10, 25, 39, 44, 47). Each of these studies was complicated by the predissociation discussed above. Self-quenching cross sections measured by Luypaert and coworkers (25) decreased with increases in v' or J' while radiative lifetimes decreased with increasing J' or decreasing v' . Total quenching rates reported in studies in $v' = 7, 11$ and 14 by Van de Burgt and Heaven (44) and $v' = 11, 12$ and 14 by Clyne, Heaven and Davis (10) also exhibited rotational level dependence. Both studies observed negative curvature in Stern-Volmer plots for low J' levels which was attributed to rotational energy transfer from the parent J' levels toward higher J' levels for a more thermalized distribution. The transfer to higher J' levels resulted in more efficient spontaneous predissociation. Yamasaki and Leone systematically examined the total quenching rate rotational dependence in $v' = 24$ for various J' levels with argon as collision partner (47). They observed a marked decrease in total quenching rate constants with increasing J' up to $J' = 41$. Higher J' energy levels in $v' = 24$ exhibited negative quenching rate coefficients. In other words, the observed fluorescence decay lifetimes increased with increasing buffer gas concentrations. Since the energy for $v' = 24, J' > 41$ is greater than that of $v' = 25, J' = 0$, they proposed a $V \leftrightarrow R$ energy transfer mechanism from $v' = 24, J' > 41$ to $v' = 25$, low J' levels where decreased spontaneous predissociation would account for the anomalous quenching rates. Similar abrupt changes in

total quenching rates with J' levels were reported by Smedley and coworkers for studies in $\text{Br}_2(\text{B})$, $v' = 27$ (39).

Even with the wealth of information on collisional removal from the $\text{Br}_2(\text{B})$ state, little data exists on state-to-state energy transfer rates. Several of the studies above indicated observation of emissions from collisionally populated states, however, few significant quantitative results have been previously reported. Clyne, Heaven and Davis reported a vibrational transfer rate coefficient for N_2 of $k(\text{N}_2, \text{V} \rightarrow \text{T}) = 2.5 \pm 1.0 \times 10^{-11} \text{ cm}^3/\text{molec}\cdot\text{sec}$ for transfer from $\text{Br}_2(\text{B})$ $v'=11$ to $v'=10$ (10) from a steady state analysis of spectrally resolved fluorescence intensities from CW laser induced fluorescence experiments. They also reported a mean value for total rotational energy removal out of parent levels for $v' = 11$, $24 \geq J' \geq 13$ states for argon of $k(\text{Ar}, \text{R} \rightarrow \text{T}) \approx 2.5 \times 10^{-10} \text{ cm}^3/\text{molec}\cdot\text{sec}$. They were unable to determine specific state-to-state rotational transfer rates due to insufficient signal strength and spectral resolution. Lin and Heaven used CW LIF techniques to investigate state-to-state rotational energy transfer in $\text{Br}_2(\text{B}, v' = 11, 14)$ with $\text{Br}_2(\text{X})$ collision partners (24). Their study determined that $\text{R} \rightarrow \text{T}$ transition probabilities scale according to a statistical power gap law. Their $\text{R} \rightarrow \text{T}$ rates were not consistent with the quenching studies in $v' = 11$ and 14 described earlier (5, 10) which attributed curved Stern-Volmer plots for low J' levels to rapid $\text{R} \rightarrow \text{T}$ transfer to J' levels with significantly higher spontaneous predissociation rates. Lin and Heaven revisited the quenching issue and determined that the curvature was a result of multi-level excitation caused by amplified spontaneous emissions from the excitation source used in the earlier experiments. Perram, Massman and Davis also used steady-state analysis techniques and spectrally resolved CW LIF techniques to study

R→T transfer in Br₂(B, v'=11) with Br₂(X), He, Ar and Xe collision partners (34). They reported that the state-to-state rotational energy transfer rates were less than 6×10^{-11} cm³/molec·sec for all ΔJ and all collision partners. All of the studies discussed here determined that collisional energy transfer within the Br₂(B) state is inefficient and does not compete favorably with collisional and spontaneous predissociation.

As indicated by the previous discussion, temporally resolved emissions from collisionally populated satellite levels in the Br₂(B) state are difficult to observe experimentally. This is primarily caused by the spontaneous and collision-induced predissociation mechanisms described above. Spontaneous predissociation significantly shortens radiative lifetimes while collision induced predissociation, in effect, quenches both parent and satellite level populations, also reducing observable fluorescence intensity. Clyne, and coworkers reported that the effective electronic quenching rates for v' = 2 is approximately ten times smaller than those reported for v' ≥ 4 (8). They also noted no rotational dependence for the collision-free lifetimes in v' = 2. Therefore, to effectively investigate the temporal evolution of collisionally populated satellite states in the Br₂(B) state, experiments must be performed for rovibrational levels below the predissociative curve crossing, i.e., v' ≤ 4. Thus far, no such studies have been reported for the Br₂(B) state.

4. Problem Statement

Pulsed LIF techniques were used in this research to investigate fundamental spectroscopic properties and collisional dynamics of molecular bromine. This work was divided into two separate, yet related experimental

phases. First, spectroscopic investigations have been undertaken to identify and characterize higher lying vibrational levels of ground state $\text{Br}_2 \text{X}^1\Sigma_g^+$ by spectrally resolving emissions from the electronically excited $\text{Br}_2 \text{B}^3\Pi(0_u^+)$ state. Previously unreported bandheads have been identified and spectroscopic constants have been calculated and compared with previous works. Second, state-to-state vibrational energy transfer within the non-predissociative lower lying vibrational levels ($1 \leq v' \leq 3$) in the $\text{Br}_2 \text{B}^3\Pi(0_u^+)$ state has been observed using spectrally and temporally resolved laser induced fluorescence techniques. Vibrational energy transfer and electronic quenching rates have been determined from this data for $\text{Br}_2(\text{X})$ and rare gas collision partners using the Montroll-Shuler vibrational energy transfer model. Results have been compared with studies in other halogens and interhalogens.

5. Organization

Chapter II will present a review of halogen molecular theory, laser induced fluorescence techniques and kinetic energy transfer theory common to both experimental sections. Chapter III will discuss the theory, experiments and results of the spectroscopic study of high v'' levels of $\text{Br}_2(\text{X})$. Chapter IV will discuss the same topics for the LIF study investigating vibrational energy transfer in the lower v' states in $\text{Br}_2(\text{B})$. Chapter V will present the overall conclusions of this dissertation and discuss future research possibilities in the $\text{Br}_2(\text{B})$ state.

II. Background Theory

This chapter reviews the current spectroscopic and kinetic theory relevant to both phases of this research in molecular bromine (Br_2). A summary of the various types of spectra obtained in this research will also be presented. Additional theory relevant to the specific experiments is included in the appropriate experimental chapters.

1. Molecular Theory

1.1 Halogen and Interhalogen Structure

Ground state halogen atoms have an outer electron shell configuration of s^2p^5 that results in the spin-orbit split term symbols $^2P_{3/2}$ and $^2P_{1/2}$, the former having the lower energy. Molecular orbitals can be formed from a linear combination of atomic orbitals (MO-LCAO). Two atomic $^2P_{3/2}$ orbitals combine to form σ_g , σ_u , π_g and π_u molecular orbitals (17). The molecular term symbols arise from the possible permutations of the ten valence electrons within these four orbitals. The ground electronic state configuration shown in Figure 1 is denoted $(\sigma_g)^2(\pi_u)^4(\pi_g)^4(\sigma_u)^0$ or (2440), and is designated $X^1\Sigma_g^+$. Excited electronic states arise from the promotion of one or more outer-shell electrons to a higher lying level, such as 2431, 2341 or 2422.

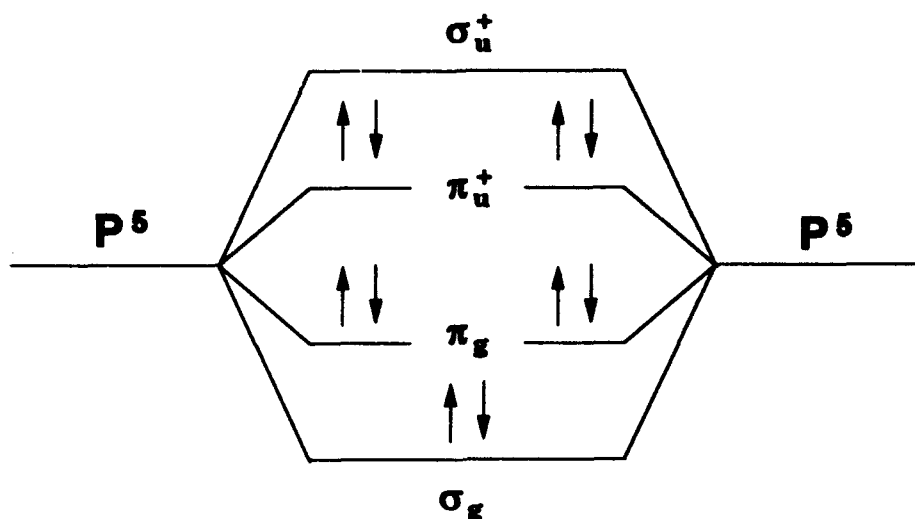


Figure 1. Ground state diatomic halogen electronic configuration

1.2 Hund's Cases

Hund has investigated several limiting cases of angular momentum coupling (Hund's cases (a)–(e)) that describe a large number of molecules (18, 41). Both coupling cases (a) and (c) are applicable to diatomic halogens and interhalogens. In the case (a) coupling scheme, the electron spin and orbital angular momentum are strongly coupled to the internuclear axis but very weakly to each other. The quantum number Ω is given as the sum of the projections of L and S along the internuclear axis, namely Λ and Σ , respectively, $\Omega = \Lambda + \Sigma$. The total angular momentum, J , can then be obtained by coupling Ω to the molecular rotational angular momentum, N , which is perpendicular to the internuclear axis. J can then take on values of $\Omega + N$, where $N = 0, 1, 2, \dots$. This coupling case yields $^1\Sigma_g^+$, $^{1,3}\Pi_u$ and $^{1,3}\Pi_g$

term symbols for the 2440, 2431 and 2341 configurations, respectively. The weak spin-orbit interaction then splits the $^3\Pi$ states into $^3\Pi(0, 1, \text{ or } 2)$ according to the total electronic angular momentum, Ω . The $\Omega = 1$ and 2 states are both doubly degenerate and the $\Omega = 0$ is also split further into plus (+) or minus (-) because of reflection symmetry. This finally leads to an entourage of states, $^3\Pi_{u,g}(2,1,0^+,0^-)$, $^1\Pi_{u,g}(1)$ and $^1\Sigma_g^+$.

In case (c) coupling, the spin-orbit interaction is so strong that it cannot be uncoupled as in the case (a) scheme which leaves Ω as the only good quantum number. This coupling results in the same manifold of levels as case (a) appearing as distinct electronic states rather than a splitting of levels within a single electronic state. It must be noted that the exact nature of the angular momentum coupling in the diatomic halogens and interhalogens is neither purely case (a) nor case (c). However, the absence of Q-branch transitions (allowed only in case (a) coupling) in the observed spectra of many interhalogens (12) indicates a tendency toward the case (c) coupling scheme. In case (c) coupling, the addition of two $^2P_{3/2}$ ground state atoms yields $(3_u, 2_u, 2_g, 1_u, 1_u, 1_g, 0_u^-, 0_u^-, 0_g^+, 0_g^+)$ states while addition of a $^2P_{3/2}$ atom and a $^2P_{1/2}$ atom yields $(2_u, 2_g, 1_u, 1_u, 1_g, 1_g, 0_g^+, 0_g^-, 0_u^+, 0_u^-)$. The rules for generating these terms for homonuclear diatomic molecules were developed by Mulliken (31). A summary of states and a correlation between the two coupling cases is shown in Figure 2.

It is known from both experimental and theoretical work that most of the states shown in Figure 2 are repulsive, or anti-bonding (17). Other than the $X^1\Sigma_g^+$ ground state, the most deeply bound states correlate to the 2431 configuration and are usually designated as the $B^3\Pi(0_u^+)$, $A^3\Pi(1_u)$ and $A^3\Pi(2_u)$ states. The visible and near infrared emission and absorption

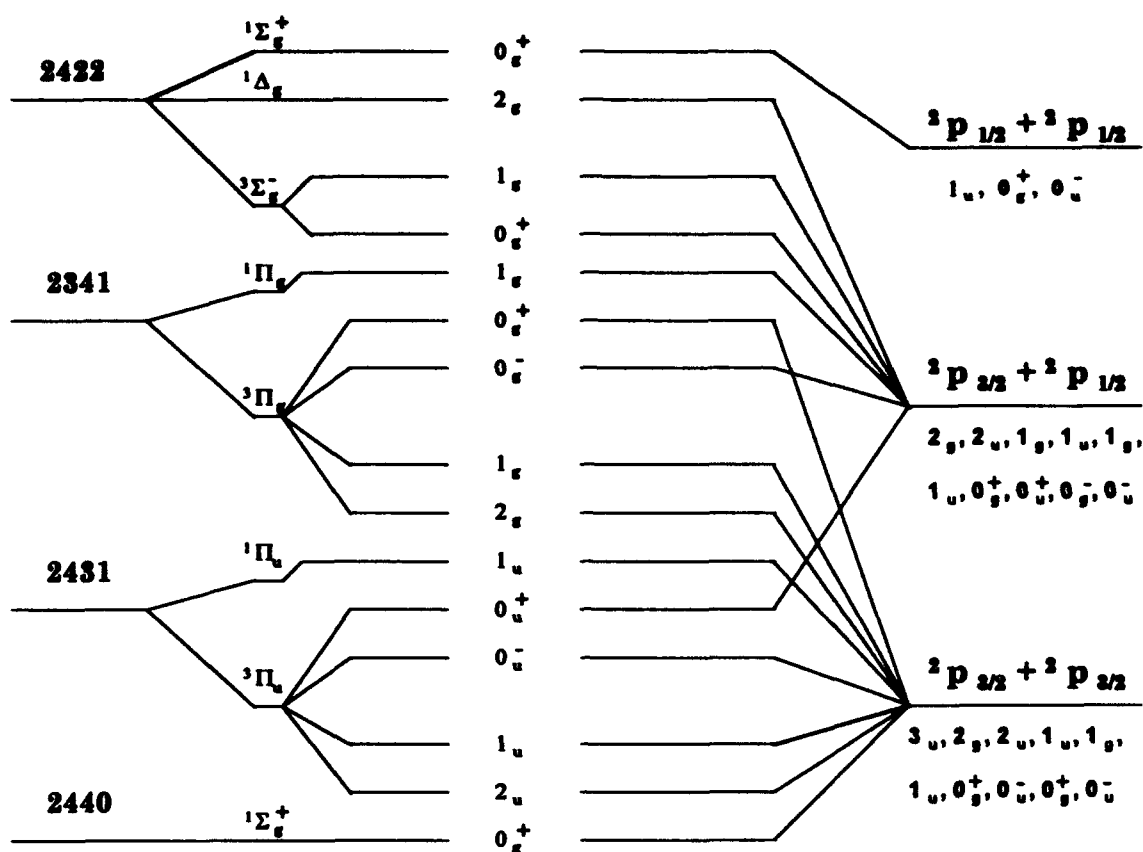


Figure 2. Hund's Cases Correlation Diagram

spectra of diatomic halogens is a result of transitions between the ground state and the A and B electronic states. Although these transitions are formally electric dipole forbidden, both the $B \rightarrow X$ and $A \rightarrow X$ transitions have been observed experimentally in the halogens and interhalogens (17). Radiative lifetimes for the diatomic halogen and interhalogen A-states are generally much longer than for the B states which are usually more intense. The B states also correspond to different separated atom states than the A states and $B \rightarrow X$ transition energies are higher than $A \rightarrow X$ transitions. Additionally, the kinetic properties of the B states are considerably more interesting because of processes such as predissociation. Consequently, the

B states of the diatomic halogens and interhalogens have been studied much more completely than the A states.

1.3 Predissociation

Collisionless, or spontaneous, predissociation can occur for any excited state vibrational level with greater energy than the ground state dissociation limit. This is certainly the case for the $\text{Br}_2(\text{B})$ state vibrational manifold as shown in Figure 3. Predissociation occurs when bound electronic state vibrational energy levels overlap with continuum energy levels from another electronic state, resulting in a non-radiative transition from the bound excited state into separated atom states associated with the continuum state. The $^3\Pi(0_u^+)$ ($v' > 4$) and $^1\Pi_u$ states in Figure 3 are such an overlapped pair. Predissociation results from the mixing of wavefunctions of the two states by a portion of the Hamiltonian operator neglected in the Born-Oppenheimer approximation (9). The non-radiative predissociation rate A_{nr} is given by Clyne, Heaven and Tellinghuisen (9) as

$$A_{\text{nr}} = (2\pi/\hbar) \left| \langle \psi_c | H' | \psi_b \rangle \right|^2 \quad (2)$$

where ψ_c and ψ_b are the wavefunctions of the continuous and bound states, respectively, and H' is the portion of the Hamiltonian noted above. A form for H' and a set of selection rules for the most important predissociation cases were initially developed by Kronig (21). In the case of bromine, the selection rules limit the possible states that may be responsible for predissociation to either or both the $A^3\Pi(1_u)$ bound state and the $^1\Pi_u$ repulsive state (9). Predissociation of this type ($\Delta\Omega = \pm 1$) is termed heterogeneous because the interactions are forbidden to a first approximation. Fully

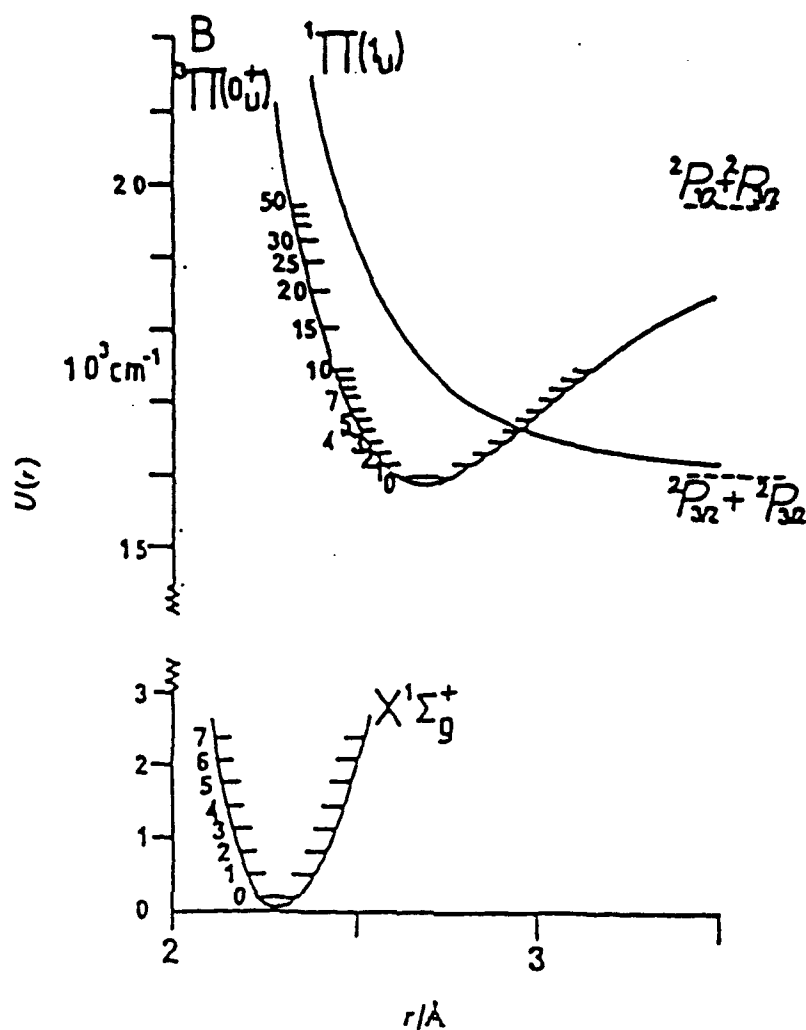


Figure 3. Br₂ potential energy curves from Clyne, Heaven and Martinez (8)

allowed homogeneous predissociation ($\Delta\Omega = 0$) results in avoided curve crossing and has been shown to occur in the interhalogens such as IBr, BrF and BrCl (17). Calculations performed by Clyne, Heaven and Tellinghuisen indicate the overlap probabilities are several orders of magnitude larger for the $1\Pi_u$ state than for the A state (9). This indicated that the former transition was the dominant predissociation path in Br₂. As noted earlier, the Clyne, et al., study determined that the $1\Pi_u$ state crosses the B state potential energy curve between $v'=4$ and $v'=5$ (9), leaving vibrational levels with $v'\leq 3$ to be relatively unaffected by predissociation.

The mechanism for the heterogeneous predissociation is rotational-electric coupling which results in an expression for A_{nr} which is proportional to $J'(J'+1)$ (9),

$$A_{nr} = k_v' J'(J'+1) \quad (3)$$

where J' is the rotational quantum number for the bound excited state and k_v' is the vibrational level dependent predissociation rate coefficient. This type of predissociation causes a shortening of observed fluorescence decay lifetime with increasing rotational quantum number according to Eq (3) and, as noted in the previous chapter, has been a topic of considerable study in Br_2 .

1.4 Spectroscopy of Bromine

Spectroscopic data on the Br_2 ($B \leftrightarrow X$) transition has been obtained through absorption, chemiluminescence and laser induced fluorescence (LIF). The visible and near infrared spectrum has been characterized in great detail (1984). Although the bands of this transition exhibit a relatively simple P and R branch structure, a great deal of overlap occurs between neighboring bands for several reasons. First, the relatively small vibrational and rotational constants in the B state and the near-integer multiple relative magnitudes of the X and B state vibrational constants (2) lead to an extremely dense spectrum. The complexity of the spectrum is further increased by the presence of three naturally occurring isotopomers $^{79}\text{Br}_2$, $^{79}\text{Br}^{81}\text{Br}$ and $^{81}\text{Br}_2$ with approximate relative abundances of 1:2:1. This complicates analysis and makes assignment of line structure a tedious process.

Several experimenters have used absorption techniques to study Br_2 . The best of these studies was the high resolution work performed by Barrow, et. al. (2) and the complementary work by Coxon (11) discussed earlier. In addition to the reported term values for the B and X states, Barrow also described the ground state energies ($0 \leq v'' \leq 10$) in a Dunham expansion in $(v'' + 1/2)$ and calculated Franck-Condon factors, \bar{r} centroids and RKR potentials (2). Barrow's spectroscopic constants are tabulated in Appendix A.

Other investigators have used chemiluminescence techniques to examine the emission spectrum of electronically excited Br_2 (5, 6, 7). Early work by Clyne and coworkers used recombination of two $^2\text{P}_{3/2}$ bromine atoms created in a flowing RF discharge as a source of electronically excited molecular bromine (5). Clyne estimated approximately 5% of the recombined Br_2 was in an electronically excited state. Spectral analysis of the afterglow emissions showed that nearly all emissions were from the $\text{Br}_2(\text{A})$ state. Later studies by Clyne and coworkers (7) showed that if the dissociated bromine atoms were recombined in the presence of metastable singlet oxygen, $\text{O}_2(^1\Delta_g, ^1\Sigma_g^+)$, the emission spectrum was dominated by $\text{Br}_2(\text{B} \rightarrow \text{X})$ transitions. Some of the transitions in the later chemiluminescence study were determined to terminate on $v'' = 15$ and 16.

The $^1\Sigma_g^+$ ground state potential energy curve shown in Figure 3 is known to dissociate into two ground state $^2\text{P}_{3/2}$ bromine atoms. However, the shape of the $^1\Sigma_g^+$ potential curve for $v'' \geq 7$ is not specified. This is due to the lack of available spectroscopic data for $v'' \geq 10$. Transitions from these levels, which occur primarily in the infrared, are quite difficult to observe in absorption spectroscopy because of the extremely small populations in these high v'' levels for a thermalized ground state at reasonable temperatures. A

laser induced fluorescence method used to examine these high v'' levels will be discussed later in this dissertation.

2. *Laser Induced Fluorescence*

Laser induced fluorescence (LIF) techniques have become extremely popular since the advent of narrow linewidth laser sources. LIF techniques involve selectively exciting, or "pumping", a specific rovibrational quantum level in an excited electronic state with a narrow linewidth pulsed or CW laser and observing the subsequent fluorescence from the excited "parent" state and/or any collisionally populated "satellite" states. This extremely versatile experimental technique, made popular by Zare and coworkers (38) has been used in applications varying from assignment of molecular spectra to determination of the internal state population distributions of chemical reaction products (32).

Figure 4 gives a simplified representation of LIF processes. A laser is tuned to optically pump the parent state, v' . Population is transferred to satellite states by inelastic collisions with buffer species. The excited states eventually relax back to the ground state due to collisional and radiative processes, the latter at wavelengths characteristic of the specific excited molecule quantum state. The fluorescence intensity of a given transition is directly proportional to the number density of the excited state, N_v ,

$$I_f = \sum_{v,w} I_{vw}^{obs} = \sum_{v,w} \left(64\pi^4/3 \right) c v_{vw}^4 q_{vw} |R_e|^2 (S_J/(2J+1)) D(v_{vw}) N_v \quad (4)$$

where

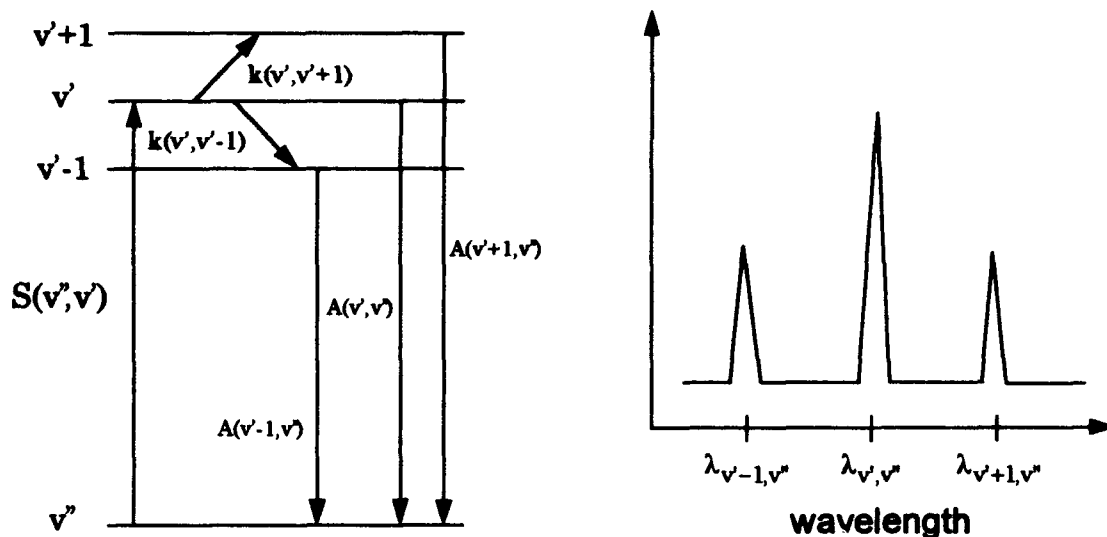


Figure 4. Simplified representation of laser induced fluorescence from collisionally populated satellite states

I_{vw}^{emm} = emission intensity from state v to state w

ν_{vw} = transition frequency from state v to state w

$q_{vw} = |\langle v | w \rangle|^2$ = Franck-Condon factor overlap for states v, w

$|R_e|$ = electric dipole moment

S_J = rotational linestrength factor

$D(\nu_{vw})$ = detection system wavelength dependence.

Detection system wavelength dependence is of considerable practical importance. For instance, in Br_2 , many of the strongest allowed emission transitions from low v' levels terminate on high v'' levels in the ground state, with transition wavelengths longer than $1 \mu m$. These wavelengths are

outside the detection limits of most photomultiplier tubes. Therefore, to observe transitions terminating on the upper v'' levels with typical photomultiplier tubes, higher v' levels in the upper electronic states must be initially populated.

Continuous wave LIF generates time-independent excited state populations that can be analyzed with steady state techniques. Collisional energy transfer rates between parent and satellite levels can be derived from the relative intensities of spectrally resolved fluorescence data using steady-state analysis techniques. Pulsed LIF creates excited state populations on a very short timescale, typically 5-10 nsec. The temporal evolution of excited states can be monitored by collecting either unresolved or spectrally resolved emissions on the same timescales as the actual energy transfer mechanisms. Equations derived in the next section can be used to extract excited state lifetimes and state-to-state energy transfer rates from the raw data. Examples of spectrally resolved and temporally resolved LIF techniques are shown in Figure 5. Clyne and coworkers have studied many of the halogens and interhalogens using both CW and pulsed LIF techniques, amassing a substantial amount of information on the radiative and kinetic properties of this interesting family of molecules (17).

3. *Kinetic Analysis*

A major goal of the current work was to experimentally investigate collisional energy transfer processes within the non-predissociative vibrational levels ($0 \leq v' \leq 4$) of the Br_2 $B^3\Pi(0_u^+)$ electronic state using pulsed LIF techniques. To properly interpret the results of LIF experiments, an

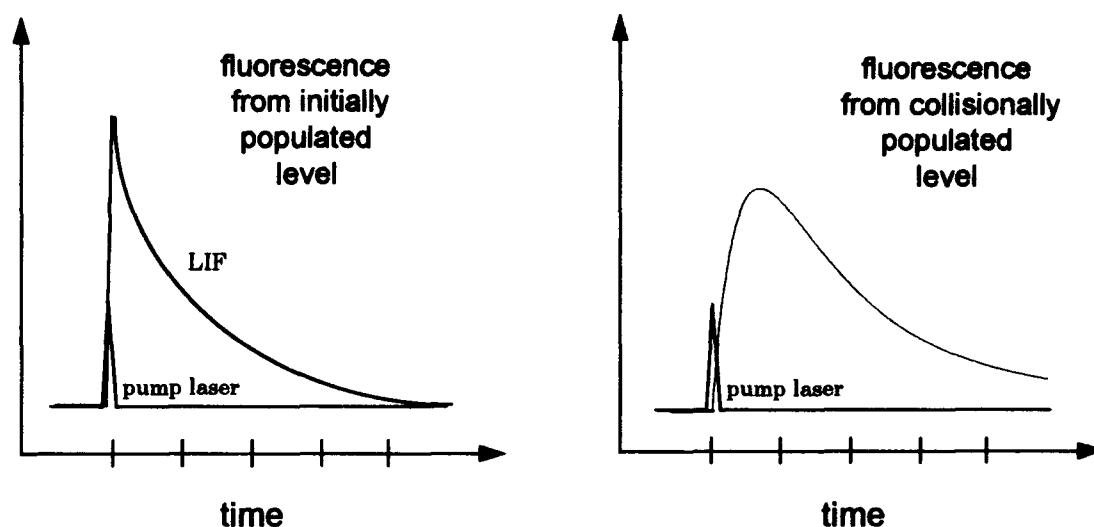


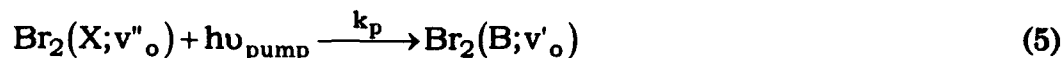
Figure 5. Example of pulsed laser induced fluorescence technique from parent and collisionally populated satellite states.

understanding of the relevant kinetic processes that affect observable quantities within the system is needed. The following sections will discuss the radiative, collisionless and collisional processes that account for energy transfer within the $\text{Br}_2 \text{B}^3\Pi(0_u^+)$ state. The time dependent master rate equation (MRE) that describes vibrational energy transfer for the $\text{Br}_2(\text{B})$ state will also be discussed. Simple solutions to the MRE that are relevant to the current study are also discussed. The particular problem of extracting state-to-state vibrational energy transfer rates from pulsed LIF data will also be discussed.

3.1 Energy Transfer Processes

This section describes several fundamental radiative, collisionless and collisional energy transfer processes that apply to all vibrational levels of the $\text{Br}_2 \text{ B}^3\Pi(0_u^+)$ state. They can be described mathematically as follows:

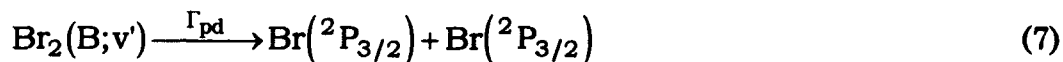
Optical excitation;



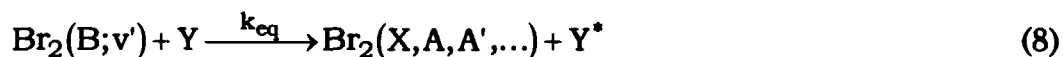
Spontaneous emission;



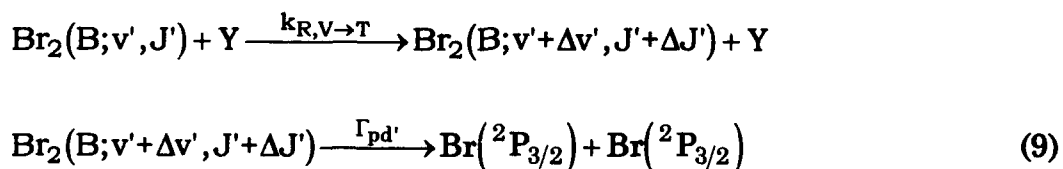
Spontaneous predissociation;



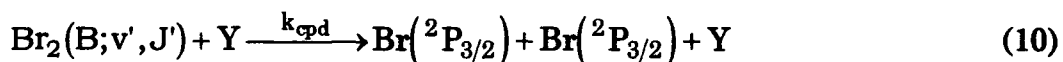
Electronic quenching;



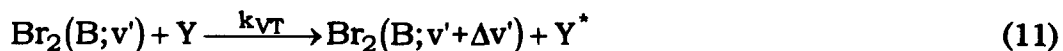
Collisional predissociation;



or



Vibrational transfer (V \rightarrow T);



Vibrational-Vibrational Transfer ($V \rightarrow V$);



In the preceding equations, "Y" denotes an arbitrary atomic or molecular collision partner while "Y*" denotes an electronically, vibrationally or translationally excited collision partner.

Optical excitation, Eq (5), is a mechanism which describes the coupling of incident laser photon energy to the $\text{Br}_2(\text{X})$ molecules, thereby perturbing the system. The specific $\text{Br}_2(\text{B}; v'_0)$ state initially populated is referred to as the parent state. The pump rate is proportional to the ground state Br_2 number density and the pump rate constant, k_p , which is given by the relation

$$k_p = (B_{01} I_0 / c) \int_0^\infty a(\nu) g_p(\nu) d\nu \quad (13)$$

where

B_{01} = Einstein coefficient for stimulated emission

I_0 = incident pump laser intensity

c = speed of light

$g_p(\nu)$ = pump laser linewidth function

$a(\nu)$ = absorption transition linewidth function

To insure selective pumping of a single rovibrational level, the pump laser linewidth, $\Delta\nu_p$, must be smaller than the absorption transition linewidth, $\Delta\nu_a$. Selectivity problems may still arise when absorption linewidths from multiple rotational transitions overlap each other. In spectrally dense molecules such as bromine, selectively pumping a single

rovibrational line, especially near (v', v'') bandheads where many absorption transitions overlap one another, is not always possible. Fortunately, for vibrational transfer studies, only the vibrational level of the excited state is of interest and in-band overlaps increase the excited state populations and intensify the observed signals. Care must still be taken to avoid absorption overlaps with other v' levels.

For pulsed laser excitation sources, if the pulsewidth is short compared to the shortest energy transfer process timescale, the pumping term can be approximated by a delta function centered at $t = 0$, with amplitude S . An alternative is to eliminate the source function and apply the initial condition

$$N(v')_{t=0} = \delta_{v'v_0} N(v_0')_{t=0} \quad (14)$$

Spontaneous emission, Eq (6), denotes the radiative decay from the excited level. The radiative lifetime from state v' is proportional to the sum of Einstein A coefficients from v' to all v''

$$1/\tau_r(v') = A(v') = \sum_{v'', J''} A(v', J' \rightarrow v'', J'')$$

Since the spontaneous emission from an excited state is directly proportional to the population in the state, the temporal evolution of parent and satellite state populations can be monitored optically. Comparisons with various kinetic models can then be made to evaluate possible energy transfer mechanisms.

Spontaneous predissociation, Eq (7), is a non-radiative loss process that results in a shortening of the measurable collision-free lifetime of a given excited state. In Br_2 , an allowed crossing of the $^3\Pi(0_u^+)$ bound state by

a repulsive $^1\Pi_u$ state between the $v' = 4$ and 5 B-state vibrational levels results in the rotationally dependent lifetimes described earlier by Eq (1). This strong predissociation is a major reason why vibrational transfer studies have not been accomplished in Br_2 .

Pure electronic quenching, Eq (8), is a collisional process that transfers population from the $\text{Br}_2(\text{B})$ electronic state to a lower Br_2 electronic state, $\text{Br}_2(\text{X}, \text{A}, \text{A}', \dots)$. Another collisional process can contribute to the overall observed electronic quenching rate. Collision-induced predissociation can occur through two mechanisms. First, as shown in Eq (9), rovibrational transfer within the B-state can occur to states with different rates for spontaneous predissociation than the parent level. The second, direct mechanism, is shown in Eq (10) where the interaction between collision partners causes the Br_2 molecule to directly dissociate on a much faster time scale than in the former mechanism. In any case, it is quite difficult to experimentally differentiate between the two collisional predissociation mechanisms. In the current vibrational transfer experiments, the effects of all predissociation mechanisms has been minimized by exciting parent levels below the predissociative crossing so only pure electronic quenching is considered.

Laser excitation of one or more rovibrational levels in an excited state produces a non-Boltzman, or non-thermal, rovibrational population distribution in the excited state. Rovibrational energy transfer, Eq (11), is the mechanism responsible for "thermalizing" the rotational and vibrational distributions within the excited state. $V \rightarrow V$ transfer, Eq (12), can occur with molecular buffer gases. This also results in thermalization of the

$\text{Br}_2(\text{B})$ state. For the purposes of the current work, the vibrational transfer rate can be written as

$$k_V = k_{VT} + k_{VV} \quad (15)$$

Before reviewing the master rate equation, it is important to note a few more energy transfer relations. The equations above describe state to state transitions for a single collision partner specie. The total vibrational transfer rate out of a single vibrational state to all other vibrational levels for collision partner Y is described by the equation

$$K_V^Y(v) = \sum_{\Delta v} k_V^Y(v \rightarrow v + \Delta v) \quad (16)$$

The total removal rate constant from a single vibrational state for collision partner Y includes quenching as well as vibrational transfer and can be expressed as

$$K_{CR}^Y(v) = K_V^Y(v) + k_q^Y(v) \quad (17)$$

where the CR subscript denotes collisional removal.

3.2 Master Rate Equation

Using the terms described in the previous section, a master rate equation that describes the time evolution of the population in a non-predissociative vibrational state $(\text{B}; v)$ can be written as

$$\begin{aligned} dN(\text{B}; v)/dt = & S\delta_{v0} - \Gamma_0(v) N(\text{B}; v) \\ & - \sum_Y k_q^Y(v) Y N(\text{B}; v) \\ & - \sum_Y \sum_{\Delta v} k_V^Y(v \rightarrow v + \Delta v) Y N(\text{B}; v) \\ & + \sum_Y \sum_{\Delta v} k_V^Y(v + \Delta v \rightarrow v) Y N(\text{B}; v + \Delta v) \end{aligned} \quad (18)$$

where the summation over Y allows for energy transfer collisions with multiple buffer species. The last term in Eq (18) allows for collisional transfer into state v from all other states v + Δv. Eq (18) can be written more concisely using notation from Perram (32) with the following definitions:

$p = (B;v)$, label for the observed vibrational level

$p_0 = (B;v_0)$, label for the parent vibrational level

$q = (v + \Delta v)$ label for the indexed vibrational level

$w_{pq} = \sum_Y k_V^Y(q \rightarrow p) Y$, the V→T rate constant from q→p

$R_{pq} = w_{pq} - \delta_{pq} \left(\sum_l w_{lp} + \Gamma_o(p) + \sum_Y k_q^Y(p) Y \right)$ the energy

transfer rate matrix connecting state q to state p

δ_{pq} = Kronecker delta function

Applying these definitions to Eq (18), the master rate equation can be written in tensor notation as

$$dN_p/dt = S\delta_{pp_0} + R_{pq}N_q \quad (19)$$

3.3 Time-Dependent Solutions

As discussed briefly earlier, for a pulsed excitation source with narrow pulsewidth, the source term in Eq (19) can be omitted and replaced by the initial condition

$$N(v')_{t=0} = \delta_{vv_0} N(v_0')_{t=0} \quad (20)$$

thus yielding the relationship

$$\begin{aligned} dx_p/dt &= R_{pq}x_q \\ x_p(0) &= \delta_{pp_0} \end{aligned} \quad (21)$$

where

$$x_p = N_p / N_{p_0} (t = 0) \quad (22)$$

is the normalized number density with respect to the initially populated state. Eqs (21) and (22) describe the time evolution of an excited state, x_p , after an initial population is created in state x_{p_0} by laser excitation. A few examples are in order.

3.3.1 Electronic Quenching / Total Removal

The most common pulsed LIF experiment involves measuring total fluorescence emissions from an excited state as a function of buffer gas pressure. This yields electronic quenching rates from the excited electronic state as a function of buffer gas species. If the excited state thermalizes rapidly, fluorescence is observed from all rovibrational levels in the excited electronic state. Defining the total observed fluorescence, x_T , as

$$x_T = \sum_p x_p \quad (23)$$

with Eq (18)

$$\begin{aligned} dx_T/dt &= - \sum_p \Gamma_o(p) x_p - \sum_Y \sum_p k_q^Y(p) Y x_p \\ &\quad - \sum_Y \sum_p \sum_q k_v^Y(p \rightarrow q) Y x_p \\ &\quad + \sum_Y \sum_p \sum_q k_v^Y(q \rightarrow p) Y x_p \end{aligned} \quad (24)$$

If the detection system collects emissions from all excited state vibrational levels equally well (i.e., regardless of transition wavelength), the last two expressions in Eq (24) cancel exactly. A further simplification can be made if the excited state radiative lifetime and electronic quenching rate are

independent of rovibrational level. Eq (24) becomes,

$$dx_T/dt = - \left(\Gamma_o + \sum_Y k_q^Y Y \right) x_T \quad (25)$$

which has the simple solution

$$\begin{aligned} x_T &= \exp(-t/\tau); \ln(x_T) = -t/\tau \\ 1/\tau &= \Gamma_o(p) + \sum_Y k_q^Y Y \end{aligned} \quad (26)$$

Plotting Eq (26) as a function of buffer gas concentration, Y, (known as the Stern-Volmer technique) yields both the total quenching rate and collision-free lifetime of the excited state.

In the case of Br₂ (B), the assumption of quantum state independent quenching rates and collision-free lifetimes, especially for v' ≥ 4 where rotational predissociation is strong, is inappropriate. If the additional constraints of spectrally resolved fluorescence and single collision conditions apply, Stern-Volmer techniques are still useful for determining total removal rates from the observed quantum state. Under single collision conditions, the master rate equation for a single state, x_p, becomes

$$dx_p/dt = - \left(\Gamma_o(p) + \sum_Y (k_q^Y(p) + K_V^Y(p)) Y \right) x_p \quad (27)$$

which has the same solution as before, namely Eq (26), with

$$\begin{aligned} 1/\tau_{TR} &= \Gamma_o(p) + \sum_Y (k_q^Y(p) + K_V^Y(p)) Y \\ &= \Gamma_o(p) + \sum_Y K_{CR}^Y(p) Y \end{aligned} \quad (28)$$

Eq (28) can be applied to vibrationally (p = (v)) resolved emissions under

single collision conditions, to obtain state-dependent collision-free lifetimes and total collisional removal rates.

3.3.2 Vibrational Transfer

In the previous section, various assumptions were made to determine reasonably simple solutions to the master rate equation that associate experimentally observable quantities to the important kinetic properties of quenching and total removal. Obtaining state-to-state vibrational transfer rates from experimental data requires considerably more effort. For instance, a strongly coupled n -level system may have as many as $n^2 - n$ allowed transitions but only n observable states. Numerical methods can be used to solve for elements of the transition matrix, R_{pq} , by simultaneously fitting to the n spectrally resolved, temporally resolved emission traces. However, these methods are computationally laborious and there is no guarantee for uniqueness of the obtained rates (32). Clearly, reasonable approximations and/or scaling laws are needed to obtain tractable analytic solutions.

3.3.2.1 Low Pressure / Radioactive Decay Approximation

The master rate equation from Eq (18) can be written in normalized form,

$$\begin{aligned} dx_p/dt = & S\delta_{pp_0} - \Gamma_o(p) x_p - \sum_Y k_q^Y(p) Y x_p \\ & - \sum_Y \sum_q K_V^Y(p \rightarrow q) Y x_p \\ & + \sum_Y \sum_q K_V^Y(q \rightarrow p) Y x_q \end{aligned} \quad (29)$$

When the observed state p is a satellite state, the source term $(S\delta_{pp_0})$ is zero.

Additionally, if the buffer gas pressure is sufficiently low and/or observations occur at "early times", the summation over q in the final term of Eq (29) is only appreciable for $q = p_o$, the parent v' state. Combining the second, third and fourth terms in Eq (29) simply results in the reciprocal lifetime, $1/\tau_{TR}$, for total removal from state p as defined in Eq (28). Using the relationships just described, Eq (29) can be rewritten as

$$\begin{aligned} dx_p/dt &= -(1/\tau_{TR}(p)) x_p + k_{p_o \rightarrow p} Y x_{p_o} \\ k_{p_o \rightarrow p} &= k_V^Y(p_o \rightarrow p) \end{aligned} \quad (30)$$

It is clear that x_{p_o} also decays with a total removal rate characteristic of p_o , that is

$$x_{p_o} = \exp(-t/\tau_{TR}(p_o))$$

so

$$dx_p/dt = -(1/\tau_R(p)) x_p + k_{p_o \rightarrow p} Y \exp(-t/\tau_R(p_o)) \quad (31)$$

The solution for this equation is

$$\begin{aligned} x_p(t) &= \left(\frac{k_{p_o \rightarrow p} Y}{(1/\tau_{TR}(p)) - (1/\tau_{TR}(p_o))} \right) \times \\ &\quad [\exp(-t/\tau_{TR}(p_o)) - \exp(-t/\tau_{TR}(p))] \end{aligned} \quad (32)$$

where $\tau_{TR}(p)$ and $\tau_{TR}(p_o)$ are the total removal rates for the observed vibrational level and parent vibrational level, respectively. This equation reproduces the general features of spectrally resolved, temporally resolved emissions from collisionally populated vibrational levels. The fluorescence intensity initially increases exponentially according to the faster of the two

total removal rates, usually that of the higher v' level, and eventually decays away at the lower v' level removal rate. Another mechanism that only allows transfer from each vibrational level to the next lower level (analogous to radioactive decay) yields a solution of the same form as Eq (32) where the two exponential rates correspond directly to the energy transfer rates into and out-of the observed state (33).

3.3.2.2 *The Montroll-Shuler Model*

The underlying assumptions that make the closed form solutions just described possible are probably not valid for the current work. In the case of the radioactive decay analogy, energy transfer occurs sequentially from one vibrational level to the next lower level only, so that no vibrational ladder climbing is allowed. Smedley found that approximately 8% of Br_2 molecules excited to within 5 kT of the B-state dissociation limit dissociate into Br^* and Br (39), the B-state dissociation products, indicating significant vibrational ladder climbing is possible in $\text{Br}_2(\text{B})$. While the solution in Eq (32) allows for vibrational ladder climbing, it neglects transfer into the observed state from anywhere except the parent level. In the strongly coupled $\text{Br}_2(\text{B})$ state where $\Delta E_{p \rightarrow q}/k_B T < 1$, if vibrational transfer competes favorably with electronic quenching, it is likely that a significant amount of vibrational transfer into the observed level could come from levels other than the parent state.

The Montroll-Shuler model for harmonic oscillators (30) provides a more rigorous approach to solving the master rate equation than the method discussed in the previous section. Montroll-Shuler also yields an analytic solution and allows extraction of state-to-state vibrational transfer rates. In

this model, four basic assumptions are made:

1. Transitions involving only $|\Delta v| = 1$ are allowed;
2. Landau-Teller scaling of V→T transfer rates with vibrational quantum number is applied;
3. Detailed balance is used for inverse transfer rates;
4. Radiative lifetimes and electronic quenching rates are independent of vibrational level.

The fourth assumption uncouples electronic removal processes and V→T transfer processes. The first three assumptions relate all V→T transfer rates to a single fundamental rate constant, $k_V^Y(1,0)$, the rate of transfer from $v' = 1$ to $v' = 0$. The closed form solution for population in state p is given by

$$x_p(t) = \frac{(1 - e^{-\Theta}) e^{\Theta} e^{-\Gamma_0 t}}{(e^{-t'} - e^{-\Theta})} \left(\frac{e^{-t'} - 1}{e^{-t'} - e^{-\Theta}} \right)^{p+q} F(-p, -q, 1; u^2) \quad (33)$$

where

$$\Gamma_0 = 1/\tau_0 = 1/\tau_r + \sum_Y k_q^Y Y$$

$$\Theta = \omega_e/k_B T$$

ω_e = the fundamental vibrational frequency

$$t' = t (1 - e^{-\Theta}) \Gamma_v$$

$$\Gamma_v = \sum_Y k_V^Y(1,0) Y$$

$$u = \sinh(\Theta/2)/\sinh(t'/2)$$

F = hypergeometric function

A distinct advantage of the Montroll-Shuler model is that if the electronic removal rates are known, only a single temporal profile from a

collisionally populated state is required to obtain a value for $k_V^Y(1,0)$, and thus, the entire rate matrix, R_{pq} . A more detailed description of the Montroll-Shuler model is presented in Appendix B.

The validity of the Montroll-Shuler assumptions for the $\text{Br}_2(\text{B})$ state is certainly open to question. The anharmonicity in the $\text{Br}_2(\text{B})$ state, $\omega_e \chi_e / \omega_e = 0.01$, is nearly as low those of IF and BrF, 0.007 and 0.009, respectively. $V \rightarrow T$ transfer is described adequately in both of these molecules by Montroll-Shuler. It may also be reasonable to assume that the radiative lifetimes and electronic quenching rates in the non-predissociative v' levels of $\text{Br}_2(\text{B})$ are independent of v' . The two primary uncertainties in applying the Montroll-Shuler model to vibrational energy transfer in $\text{Br}_2(\text{B})$ are (1) assuming only $|\Delta v| = 1$ transitions as $\Delta E_{p \rightarrow q} / k_B T \approx 2/3$ for the heated cell ($T = 370 \text{ K}$) studies performed here, and (2) the invariance of the electronic quenching rates and radiative lifetimes with vibrational level.

4. Experimental Approach

A careful, systematic experimental approach is necessary to properly interpret results of LIF experiments. To this end, several different pulsed LIF experimental techniques were used in the current work. This section describes how the various LIF techniques described earlier were applied to the current studies.

4.1 Laser Excitation Spectra

In each of the two studies discussed in the following chapters, the first task was to determine appropriate pump laser wavelengths to selectively

excite the desired $\text{Br}_2(\text{B};v', J')$ excited state. Laser excitation spectra were taken by observing spectrally unresolved side-fluorescence from the Br_2 sample with a fast photomultiplier tube (PMT) as a function of pump laser wavelength while the dye laser frequency was scanned across the laser dye curve. A gated boxcar integrator was used to provide a continuous, time-averaged value for the pulsed LIF intensity. The analog voltage output from the boxcar integrator was digitized, stored on computer and calibrated to the dye laser wavelength readout. The LIF intensity versus pump wavelength spectra obtained with this method are equivalent to conventional absorption spectra. The resolution obtained with this method is a convolution of the pump laser linewidth, laser scanning speed and boxcar time constant. The highest attainable resolution is limited by the pump laser linewidth, in this case, 0.07 Å. High resolution scans are obtained by using slow scan speeds and short boxcar time constants such that the pump wavelength changes less than the laser linewidth during a boxcar sampling period, or

$$\tau_{\text{boxcar}}(\text{sec}) \ll \frac{\text{laser linewidth } (\lambda)}{\text{laser scan speed } (\lambda/\text{sec})} \quad (34)$$

For the vibrational transfer experiments, limitations in the spectral response of the total fluorescence detection system for particular $\text{Br}_2(\text{B})$ vibrational states limited the usefulness of typical laser excitation spectra just described. Vibrational state dependent excitation spectra were recorded by spectrally resolving the emissions detected by the PMT through a monochromator. Excitation spectra from different vibrational levels could be compared over similar pump wavelength ranges to identify suitable pump laser wavelengths for selectively exciting individual vibrational bands.

4.2 Emission Spectra

The next task conducted in each study was to spectrally resolve emissions from particular $\text{Br}_2(\text{B})$ rovibrational states identified from the laser excitation spectra. The dye laser was tuned to a particular $\text{Br}_2(\text{B} \leftarrow \text{X})$ transition. Fluorescence was observed with a PMT through a wavelength scanning monochromator, integrated by the boxcar integrator and stored as a function of monochromator wavelength. For the spectroscopic study, these spectra were used to identify the relative energy spacings of high vibrational levels in the ground state. In the kinetic work, these spectra verified the existence of vibrational energy transfer within the $\text{Br}_2(\text{B})$ state and aided in selection of appropriate observation wavelengths for the spectrally resolved, temporally resolved vibrational transfer experiments.

4.3 Spectrally Resolved, Temporally Resolved Fluorescence

The final experimental task was to obtain spectrally resolved, temporally resolved LIF emission profiles for both parent and collisionally populated satellite vibrational levels. For these experiments, the pump laser was tuned to excite a single vibrational level. The monochromator was also tuned to pass emissions from either the parent level or a collisionally populated satellite level only. The spectrally resolved emissions were detected by the PMT, amplified, and sent to a digital oscilloscope where the emission time profiles were averaged over many laser pulses (typically 1000-2000 shots) until the signal-to-noise ratio was determined to be acceptable.

III. Spectroscopy of High v'' Levels in $\text{Br}_2(\text{X})$

1. Introduction

Spectroscopic data for the $\text{Br}_2(\text{B} \rightarrow \text{X})$ electronic transition has been obtained using many different techniques (18). Spectroscopic constants from the high resolution absorption work of Barrow, and coworkers (2) and Coxon (13) for $v'' \leq 10$ in the ground state and nearly the entire range of bound vibrational $0 \leq v' \leq 55$ levels of the $\text{Br}_2(\text{B})$ state have been used to calculate turning points, RKR potentials and Franck-Condon factors (2) for both the $^{79}\text{Br}_2$ and $^{81}\text{Br}_2$ isotopic species. Because of the large shift in internuclear separation between the X and B states of Br_2 , many intense transitions from $\text{Br}_2(\text{B}, v')$ levels occur to highly excited vibrational levels in $\text{Br}_2(\text{X}, v'' \geq 10)$. Transitions from the high v'' levels are difficult to observe in typical absorption experiments because of the extremely small populations in these levels at reasonable temperatures. Researchers studying $\text{Br}_2(\text{B})$ kinetic processes have noted the presence of P-R doublet emissions extending to 890 nm from individually pumped rovibrational levels in the $\text{Br}_2(\text{B})$ state manifold (25). However, no spectroscopic analyses of these transitions to high v'' levels have been reported. It is of interest, therefore, to know whether the $\text{Br}_2(\text{X})$ ground state molecular constants from Barrow's study (2), adequately describe these higher v'' levels. Rao and Venkateswarlu (37) observed a single series of resonance fluorescence doublets in the vacuum ultraviolet region. The emissions were assigned as P-R doublets from an excited electronic state of the $^{79}\text{Br}^{81}\text{Br}$ mixed isotope to ground state vibrational levels up to $v'' = 36$.

Consistent with the Franck-Condon principle, many ground state vibrational levels were not observed. Irreconcilable differences with later work (12) suggests the need for additional investigations.

The present study was undertaken to expand the spectroscopic database for the $\text{Br}_2(\text{X})$ ground state and to determine whether the spectroscopic constants from the extensive work of Barrow and coworkers (2) are sufficient for describing high vibrational levels ($v' > 10$) in the $\text{Br}_2(\text{X})$ ground state. Spectrally resolved laser induced fluorescence (LIF) emissions to high v'' levels from the electronically excited $\text{Br}_2(\text{B})$ state in the $^{79}\text{Br}^{81}\text{Br}$ isotopomer were observed from several B state vibrational levels. Vibrational bandhead assignments have been made and spectroscopic constants have been calculated and compared with the extensive analysis reported by Barrow (2).

2. Experimental Setup

A single experimental apparatus was used for the spectroscopic and kinetic studies performed for this dissertation. This section provides an overview of the experimental setup as used in the spectroscopic study. Particular changes specific to the kinetics study will be discussed in the next chapter.

A block diagram of the experimental setup is shown in Figure 6. The actual test cell was a 7.2 cm diameter, 20 cm long glass cell equipped with two 1/2" diameter glass tube ports located at opposite ends of the cell for the laser path and two 5 cm diameter observation ports for side fluorescence collection. Three additional 1/2" ports were available for the vacuum and gas handling systems. All vacuum system connections were made with 1/2" Cajon Ultratorr connectors. Both laser path ports were fitted with 2.5 cm

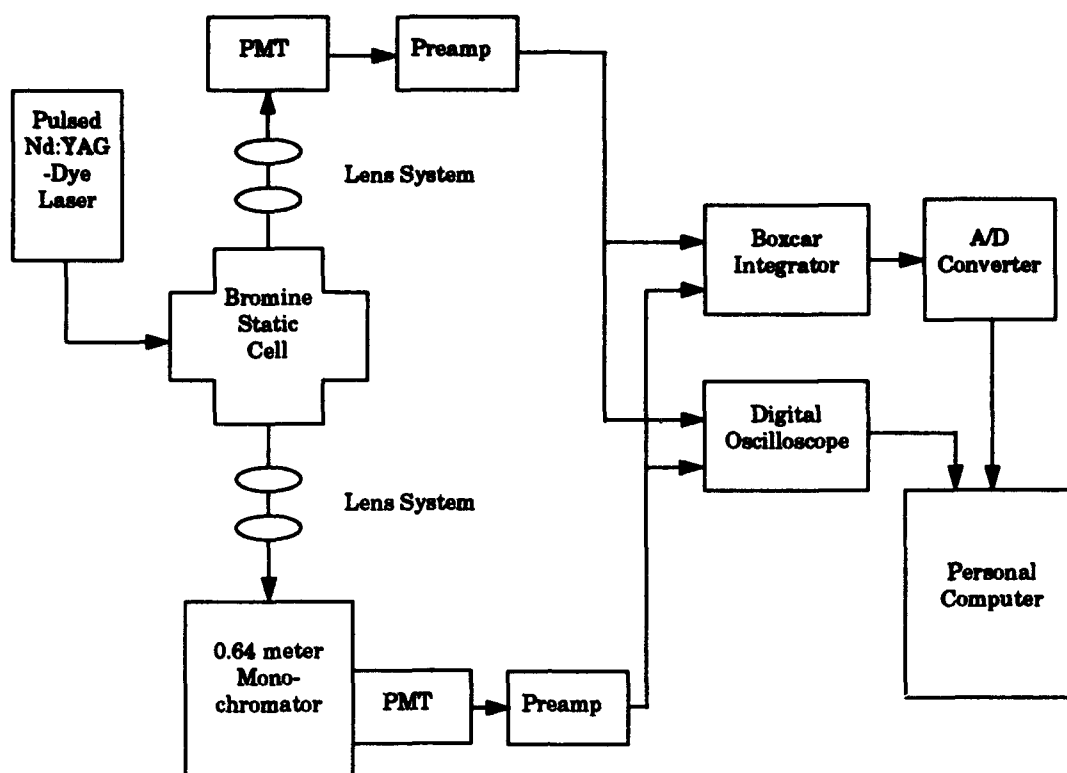


Figure 6. Block diagram of the experimental apparatus used to observe LIF in Br_2

diameter quartz Brewster angle windows to reduce reflection losses. The cell was evacuated by an Alcatel model 200 direct drive chemical plasma pump preceded by a liquid nitrogen cold trap to capture the used Br_2 . Cell pressure was monitored at an exit port by both an MKS model 390, 1 Torr capacitance manometer and an MKS model 122a, 10 Torr capacitance manometer. Test cell leak rates were measured at less than 3 mTorr/hr.

All spectroscopic experiments were conducted in a static cell filled with small amounts of gaseous Br_2 . For the spectroscopic study, liquid bromine (Spectrum Chemical, 99.5%) with natural isotopic abundances was

distilled by repeated freeze-thaw cycles. Typical Br_2 pressures for the spectroscopic study were 1–10 Torr.

Laser excitation was provided by a Spectra-Physics model PDL-3 pulsed dye laser pumped by a 20 Hz, frequency-doubled Quanta-Ray DCR-3 pulsed Nd:YAG laser. Rhodamine 575, Rhodamine 590 and LDS 698 dyes were used to excite various $\text{Br}_2(\text{B})$ vibrational levels. The Nd:YAG pumped dye laser system typically provided 10 nsec, 40 mJ pulses for the Rhodamine dyes. The beam was focused to approximately a 1 mm diameter spot size at the center of the cell. The dye laser linewidth was 0.07 cm^{-1} .

Side fluorescence (LIF) emissions were detected through the two observation ports located on opposite sides of the fluorescence cell. Each was equipped with a 5 cm Pyrex window. A two-lens system was used to collect the emissions from the Br_2 sample. The first was a 2" diameter, 10 cm focal length lens placed next to the Pyrex window, one focal length from the center of the fluorescence line. The second was a 2" diameter, 5 cm focal length lens that focused the collected light onto a variable slit (typically set at 1 mm width) mounted in front of a long-pass filtered RCA C31034 Photomultiplier Tube (PMT). Both the slit and filter were used to minimize collection of scattered laser light from the dye laser. For the spectroscopic work, two Corian 600 nm longpass colored glass filters were used. The PMT output was fed through a PARC Model 115 wide band preamplifier into one channel of a PARC Model 165 dual channel boxcar integrator for signal averaging. Emissions were collected through the second observation window by another two lens system (the second lens of this pair had a focal length of 15 cm) and focused onto the entrance slit of an Instruments SA, Inc. HR640 0.64 meter monochromator with a 1200 groove/mm grating blazed at 1 micron. Another

RCA C31034 PMT detected the spectrally resolved emissions in the 560-880 nm wavelength range. The output from the PMT was fed through a second wide band preamplifier to the second channel of the boxcar integrator. The monochromator wavelength readout was calibrated using Oriel neon, argon and krypton calibration lamps and the tables of atomic spectral lines of Striganov and Sventitskii (44). Calibration procedures are discussed in Appendix C.

Outputs from the boxcar integrator were sent to a Zenith 248 personal computer equipped with a Metrabyte DAS-8 analog-digital data acquisition board where the averaged intensities were digitized and stored to disk. The files were then transferred to a 50 MHz DigiView 486DX personal computer for analysis and data reduction. For the temporally resolved LIF experiments, the boxcar integrator was replaced by a LeCroy 9450, 350 MHz bandwidth, Digital Oscilloscope. Oscilloscope traces were transferred directly to the 486DX PC through a National Instruments AT-GPIB board driven by a National Instruments LabWindows QuickBasic program.

2.1 Spectroscopic Experiment

In the spectroscopic experiments, the pulsed dye laser with Rhodamine 575 and Rhodamine 590 dyes was used to excite $\text{Br}_2(\text{B})$ vibrational levels with $15 \leq v' \leq 21$ at wavelengths of 550–620 nm. Typically, narrow linewidth lasers allow for selective excitation of single rovibrational transitions in particular Br_2 isotopes. However, in the present work, the dye laser was tuned to wavelengths very near the bandheads of the $\text{Br}_2(v', v'')$ transitions of interest so that the laser linewidth overlapped several low- J transitions. This effectively increased the emission signal levels from the $^{79}\text{Br}^{81}\text{Br}$ isotope

and aided in discriminating them from emissions from other excited isotopic species. The spectrally resolved emissions were detected with the RCA C31034 PMT in the 560-880 nm wavelength range and an RCA 9684B PMT with an S20 spectral response curve in the 880-980 nm range. The monochromator slit width for the 560-880 nm range was 50 μm with a resolution of 0.16 nm. Slit widths for the 880-980 nm range were 125 μm yielding a resolution of 0.4 nm.

3. *Laser Excitation Spectra*

Low resolution laser excitation spectra (described in chapter II) for $\text{Br}_2(\text{B} \rightarrow \text{X})$ transitions were taken across both dye curves to identify isotopic bandheads and to determine pump wavelengths for the spectrally resolved experiments. A typical low resolution excitation spectrum taken for the Rhodamine 575 laser dye is shown in Figure 7. Barrow's vibrational constants (2) were used to identify the $^{79}\text{Br}^{81}\text{Br}$ bandheads. This figure clearly demonstrates the complexity of the $\text{Br}_2(\text{B} \rightarrow \text{X})$ spectrum. Higher resolution excitation spectra were also taken near the $^{79}\text{Br}^{81}\text{Br}$ bandhead regions to accurately locate pump wavelengths for the best possible emission spectra. These spectra were obtained by decreasing the laser scan speed by a factor of eight from the low resolution spectra. Figure 8 shows the bandhead region of the $(\text{v}', \text{v}'') = (17, 0)$ transition for both the $^{79}\text{Br}_2$ and $^{79}\text{Br}^{81}\text{Br}$ isotopes. The pump wavelength identified from Figure 8 was 5519.6 \AA . The resolution of the excitation spectra in Figure 8 can be estimated in the following manner. The spectral feature assigned to the 79-81(17,0) P(10)R(13) overlap transition also overlaps the 79-79(17,0) P(19)R(22) transition. All four of these

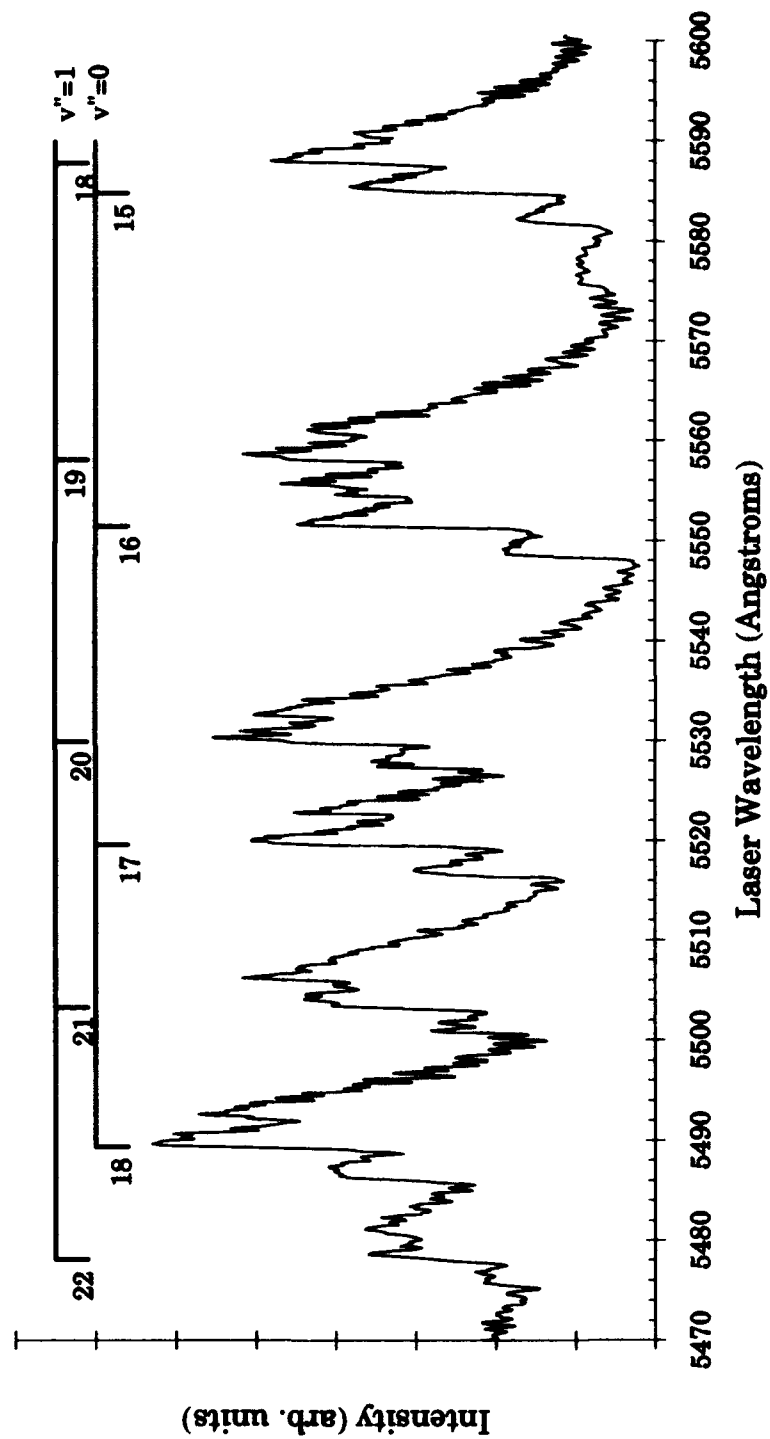


Figure 7. Low resolution laser excitation spectra using Rhodamine 575 laser dye. B \rightarrow X transition bandheads are labeled (v',v'') for the ^{79}Br - ^{81}Br isotope

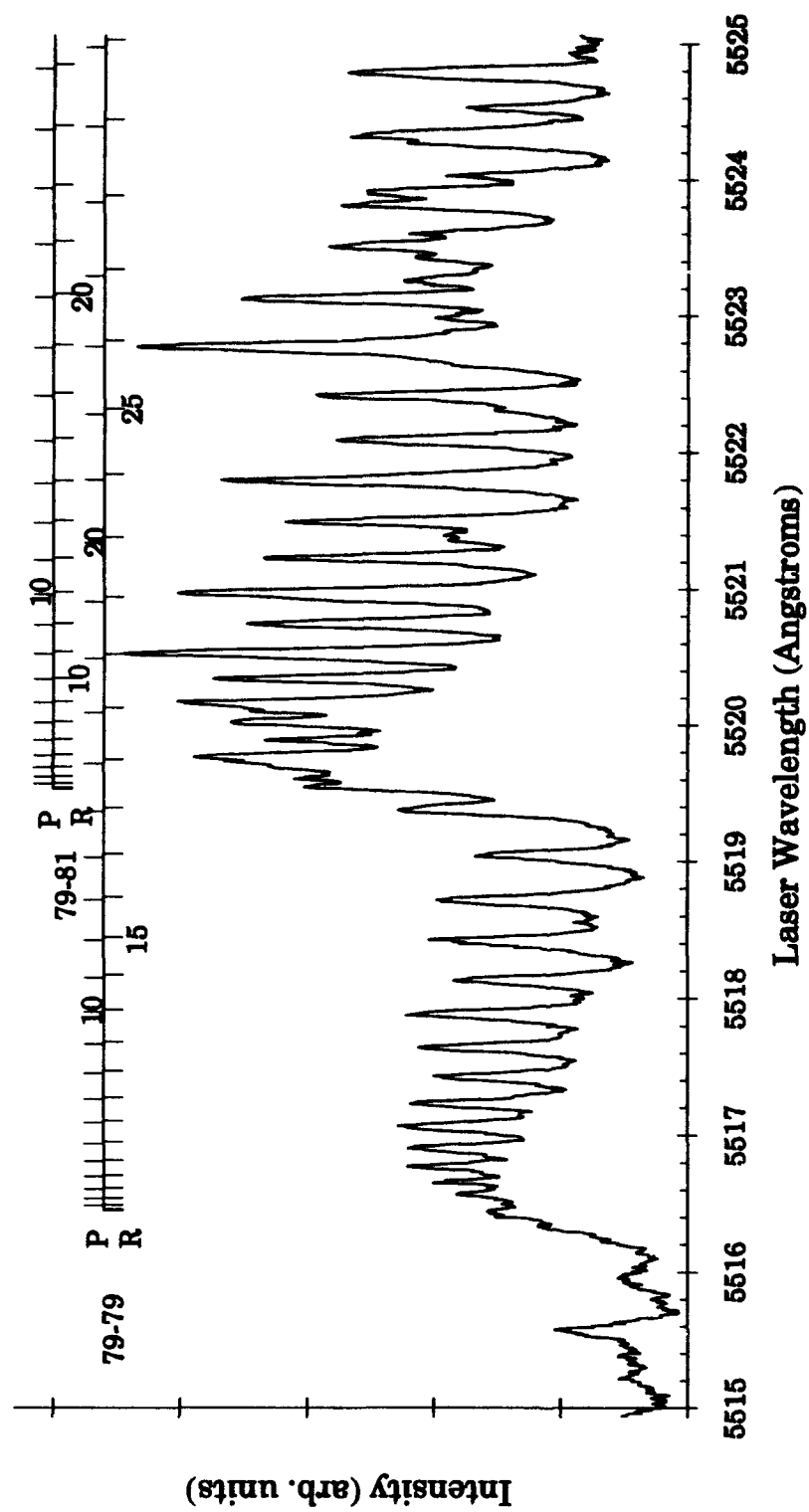


Figure 8. High resolution laser excitation spectra using Rhodamine 575 laser dye near the (17,0) transition bandhead for the $^{79}\text{Br}-^{81}\text{Br}$ and $^{79}\text{Br}_2$ isotopes

transitions are within 0.1 Angstrom of one another and are not resolved separately in Figure 8. However, the line positions for the 79-81 (17,0) P(15) and 79-79(17,0) R(25) lines which are separated by 0.1 Å are resolved in Figure 8. Therefore, the minimum resolvable difference in Figure 8 is estimated at 0.1 Å. Pump wavelengths for the Br₂(B ← X) transitions used in this study were determined from excitation spectra similar to those in Figures 7 and 8 and are listed in Table 1.

Table 1

Dye laser wavelengths used for excitation of
⁷⁹Br⁸¹Br(B→X) (v',v'') transitions

(v',v'')	wavelength (Å)
(15,0)	5584.9
(16,0)	5551.4
(17,0)	5519.6
(18,0)	5489.3
(19,1)	5558.1
(20,1)	5529.9
(21,1)	5503.3

4. *Experimental Results and Discussion*

To obtain the desired emission spectra, the dye laser wavelength was tuned to one of the ⁷⁹Br⁸¹Br transitions listed in Table 1 while the monochromator was scanned across the wavelength detection range of the appropriate PMT. Emission spectra were obtained with both PMTs for each

pump transition in Table 1. Figures 9 and 10 show typical emission spectra over a portion of the observed wavelength range for three different (v',v'') pump transitions. Missing transitions followed the predictions of the $^{79}\text{Br}^{81}\text{Br}$ Franck-Condon factor calculations of Coxon (13) which he had extrapolated to high v'' . Figure 11 shows an expanded view of the emissions near the (16,6) bandhead. Note that the full-width at half-maximum (fwhm) of the spectral feature labeled as the (16,6) bandhead is approximately 2 Å. This is slightly wider than the monochromator resolution of 1.6 Å for a slit width of 50 μm (see Appendix C). The rotational distribution of the observed (16,6) emissions is virtually unrelaxed, even at pressures of up to a few Torr. However, because the linewidth of the dye laser overlaps several (16,0), P(J) and R(J) transitions near the bandhead, it is probable that multiple J' levels are directly excited by the pump laser. Overlap comparisons between the dye laser linewidth and P-R absorption transition line positions calculated from Barrow's spectroscopic constants indicate that excitation of $0 \leq J' \leq 6$ are possible for all of the (v',v'') transitions studied here. Observed emissions are generally consistent with these comparisons as emissions from low J' values in $\text{Br}_2(\text{B},v')$ occur at wavelengths within 1–2 Å of the bandhead. The additional emission lines evident in Figure 11 arise from accidental absorption overlaps between P-R transitions in the $^{79}\text{Br}_2(16,0)$ transition, the $^{79}\text{Br}^{81}\text{Br}(20,1)$ transition and the bandhead region of $^{79}\text{Br}^{81}\text{Br}(16,0)$ transition. Most of the additional emission lines can be identified for the $(v',v'' \leq 10)$ transition regions in a similar manner using Barrow's spectroscopic constants (2). Identifiable bandhead progressions were observed from all $15 \leq v' \leq 21$ levels to $0 \leq v' \leq 21$ levels except for $v' = 21$ where overlap from high J' levels of the $^{79}\text{Br}_2(18,v'')$ transitions made accurate identification

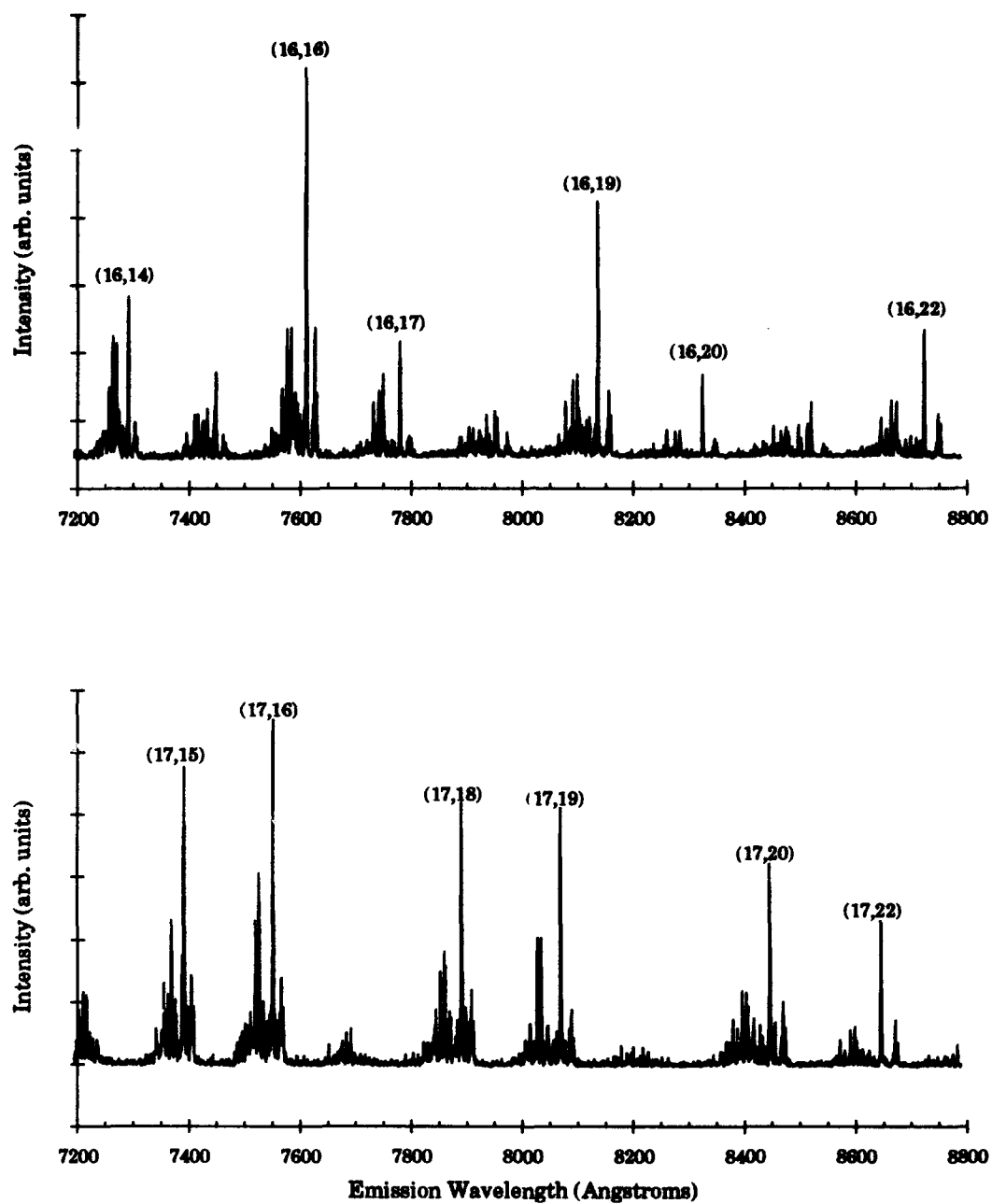


Figure 9. Emission spectra from $v' = 16$ and 17 with (v', v'') transitions labeled

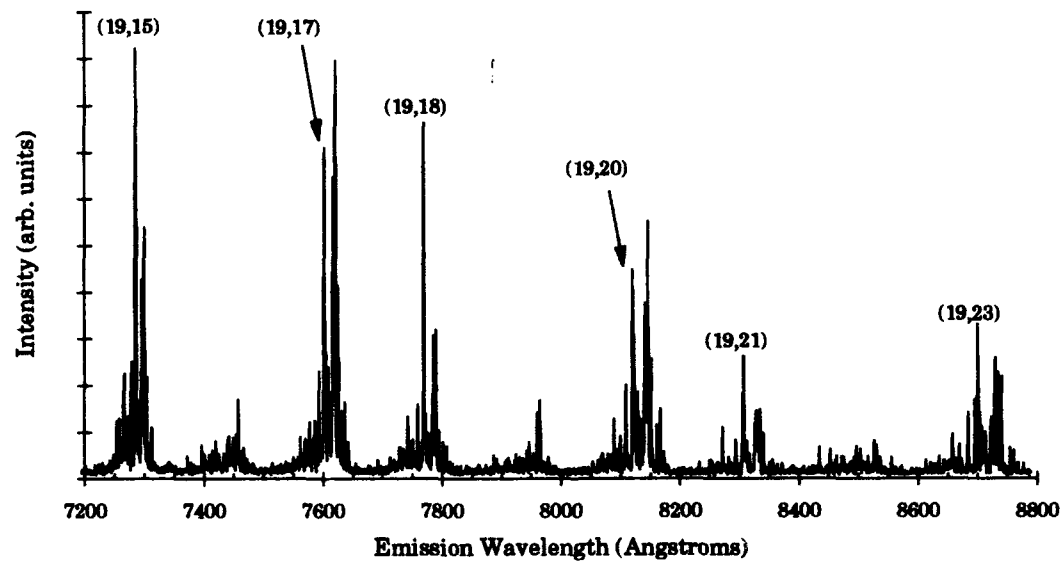
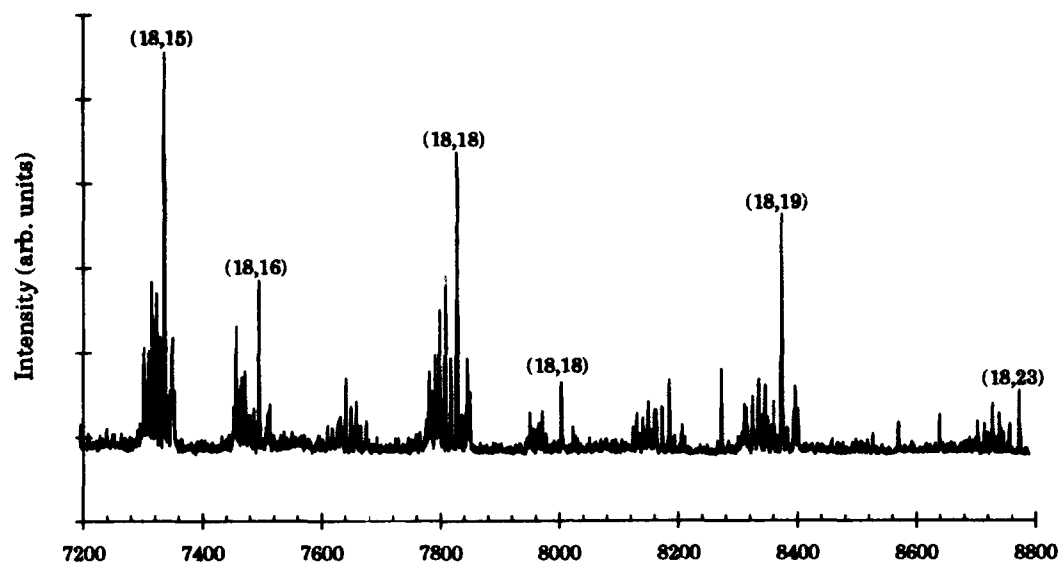


Figure 10. Emission spectra from $v' = 18$ and 19 with (v', v'') transitions labeled

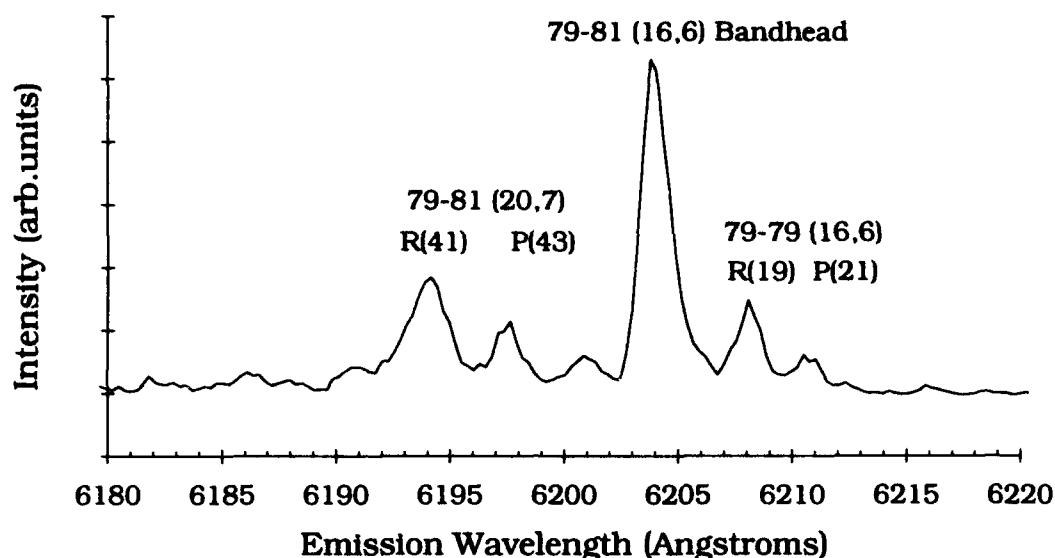


Figure 11. Plot of LIF intensity versus wavelength near the (16,6) bandhead of $^{79}\text{Br}^{81}\text{Br}$ ($B \rightarrow X$) transition

impossible. The transition that terminated on the highest observed v'' level was the (17, 27) transition. Bandhead positions for the $B \rightarrow X$ transitions were identified from the emission spectra for each of the various pumped B state levels, converted to vacuum wavenumbers (cm^{-1}) and arranged in a Deslandres table. All observed bandhead positions are reported in Table 2. The rotationless bandhead positions listed for comparison were calculated using Barrow's molecular constants (2). Differences between the experimentally determined bandhead positions and the calculated values are also included along with the bandhead assignments. The differences between observed and calculated values give a mean value of 1.4 cm^{-1} , which is within the experimental resolution of the current work.

Table 2
Observed Br₂ bandhead assignments for the B→X Transitions

Wavelength in air (Å)	Vacuum Wavenumbers (cm ⁻¹)	Calculated (from Barrow) (cm ⁻¹)	Residual (cm ⁻¹)	Vibrational Assignment (v',v'')
5686.6	17580.3	17579.4	0.9	(15,1)
5791.6	17261.8	17260.4	1.4	(15,2)
5900.2	16944.0	16943.5	0.5	(15,3)
6011.8	16629.3	16628.8	0.5	(15,4)
6126.1	16319.1	16316.3	2.8	(15,5)
6246.2	16005.3	16006.1	-0.7	(15,6)
6367.8	15699.6	15698.0	1.6	(15,7)
6494.7	15393.0	15392.2	0.8	(15,8)
6760.2	14788.4	14787.2	1.1	(15,10)
6901.0	14486.7	14488.2	-1.5	(15,11)
7194.2	13896.3	13897.0	-0.6	(15,13)
7348.7	13604.1	13604.8	-0.7	(15,14)
7844.0	12745.1	12742.4	2.6	(15,17)
7673.3	13028.5	13027.5	1.0	(15,16)
8206.3	12182.4	12179.4	3.1	(15,19)
8397.5	11905.0	11901.5	3.6	(15,20)
8806.6	11352.0	11352.9	-0.9	(15,22)
9020.0	11083.5	11082.2	1.2	(15,23)
9476.2	10549.9	10548.4	1.5	(15,25)
9717.6	10287.8	10285.2	2.6	(15,26)
5651.0	17691.0	17687.3	3.8	(16,1)
5754.9	17371.6	17368.2	3.3	(16,2)
5863.1	17051.0	17051.4	-0.4	(16,3)
5972.7	16738.3	16736.7	1.6	(16,4)
6203.8	16114.7	16113.9	0.8	(16,6)
6324.6	15807.0	15805.9	1.1	(16,7)
6711.2	14896.3	14895.1	1.2	(16,10)
7137.7	14006.3	14004.8	1.5	(16,13)
7290.5	13712.7	13712.7	0.0	(16,14)

Table 2 (continued)

Wavelength in air (Å)	Vacuum Wavenumbers (cm ⁻¹)	Calculated (from Barrow) (cm ⁻¹)	Residual (cm ⁻¹)	Vibrational Assignment (v',v'')
7610.3	13136.4	13135.4	1.0	(16,16)
7778.4	12852.6	12850.3	2.3	(16,17)
8135.0	12289.1	12287.3	1.8	(16,19)
8323.4	12011.0	12009.3	1.7	(16,20)
8722.2	11461.9	11460.7	1.1	(16,22)
8932.6	11191.8	11190.1	1.7	(16,23)
9379.6	10658.5	10656.3	2.2	(16,25)
5618.6	17793.1	17791.2	1.9	(17,1)
5722.0	17471.7	17472.1	-0.5	(17,2)
5828.3	17153.0	17155.3	-2.3	(17,3)
5935.9	16841.9	16840.6	1.3	(17,4)
6164.1	16218.6	16217.8	0.7	(17,6)
6284.8	15907.0	15909.8	-2.8	(17,7)
6533.8	15300.8	15300.3	0.5	(17,9)
6665.8	14997.9	14999.0	-1.2	(17,10)
6940.7	14403.8	14403.2	0.6	(17,12)
7086.6	14107.3	14108.7	-1.4	(17,13)
7390.9	13526.3	13526.8	-0.4	(17,15)
7551.0	13239.6	13239.3	0.2	(17,16)
7889.9	12670.9	12671.5	-0.6	(17,18)
8068.2	12390.9	12391.2	-0.2	(17,19)
8444.7	11838.4	11837.7	0.7	(17,21)
8644.4	11564.9	11564.6	0.3	(17,22)
9066.8	11026.2	11025.8	0.3	(17,24)
9290.4	10760.8	10760.2	0.7	(17,25)
9762.6	10240.4	10236.3	4.1	(17,27)

Table 2 (continued)

Wavelength in air (Å)	Vacuum Wavenumbers (cm ⁻¹)	Calculated (from Barrow) (cm ⁻¹)	Residual (cm ⁻¹)	Vibrational Assignment (v',v'')
5689.3	17572.0	17572.0	0.0	(18,2)
5793.5	17256.0	17255.1	0.9	(18,3)
6126.0	16319.2	16317.7	1.6	(18,6)
6245.5	16007.2	16009.6	-2.4	(18,7)
6492.0	15399.2	15400.2	-1.0	(18,9)
6620.8	15099.7	15098.9	0.9	(18,10)
6893.6	14502.2	14503.0	-0.8	(18,12)
7036.2	14208.2	14208.6	-0.4	(18,13)
7335.5	13628.6	13626.6	2.0	(18,15)
7494.2	13340.0	13339.2	0.8	(18,16)
7827.3	12772.2	12771.3	0.9	(18,18)
8002.9	12492.1	12491.0	1.1	(18,19)
8372.9	11940.0	11937.6	2.4	(18,21)
8772.9	11395.7	11393.9	1.8	(18,23)
8984.2	11127.6	11125.7	1.9	(18,24)
5658.3	17668.4	17667.7	0.6	(19,2)
5761.7	17351.3	17350.9	0.4	(19,3)
6090.9	16413.5	16413.4	0.1	(19,6)
6451.6	15495.7	15495.9	-0.3	(19,9)
6848.2	14598.3	14598.8	-0.5	(19,12)
7285.2	13722.7	13722.4	0.3	(19,15)
7602.4	13150.2	13149.8	0.4	(19,17)
7768.8	12868.4	12867.1	1.3	(19,18)
8121.0	12310.3	12308.8	1.5	(19,20)
8307.0	12034.7	12033.3	1.4	(19,21)
8700.0	11491.1	11489.6	1.4	(19,23)
8909.0	11221.5	11221.5	0.0	(19,24)
9346.8	10695.9	10692.6	3.3	(19,26)

Table 2 (continued)

Wavelength in air (Å)	Vacuum Wavenumbers (cm ⁻¹)	Calculated (from Barrow) (cm ⁻¹)	Residual (cm ⁻¹)	Vibrational Assignment (v',v'')
5629.3	17759.2	17759.4	-0.2	(20,2)
5731.1	17443.8	17442.6	1.3	(20,3)
6057.6	16503.7	16505.1	-1.4	(20,6)
6413.7	15587.2	15587.6	-0.4	(20,9)
6805.2	14690.6	14690.5	0.2	(20,12)
7088.4	14103.6	14103.9	-0.3	(20,14)
7236.7	13814.6	13814.1	0.5	(20,15)
7713.8	12960.2	12958.8	1.4	(20,18)
8244.3	12126.3	12125.0	1.3	(20,21)
8631.3	11582.6	11581.3	1.3	(20,23)
9047.7	11049.5	11047.4	2.1	(20,25)
9268.0	10786.8	10784.2	2.6	(20,26)
5601.4	17847.7	17847.0	0.7	(21,2)
5703.5	17528.2	17530.1	-1.9	(21,3)
5914.9	16901.8	16903.0	-1.2	(21,5)
6025.6	16591.4	16592.7	-1.3	(21,6)
6631.7	15074.8	15074.8	0.0	(21,11)
6764.9	14778.2	14778.0	0.1	(21,12)
7045.5	14189.5	14191.4	-2.0	(21,14)

Ground state vibrational constants were calculated from the bandhead assignments in Table 2. A brief survey of Table 2 reveals that while band progressions were observed terminating on v'' levels $1 \leq v'' \leq 27$, because of unfavorable Franck-Condon overlaps, progressions originating from one v' level may be missing every other or every third v'' level. This makes for a rather sparse Deslandres table and severely limits the use of traditional

second-differencing methods for obtaining vibrational constants. In the current work, a "term value" was calculated for each observed transition by taking the difference between observed transition wavenumber value and the wavenumber value for the parent $v' \rightarrow (v'' = 2)$ transition. As an example, the $v' = 15, v'' = 13$ term was assigned a value of 3365.5 cm^{-1} by subtracting 13896.3 cm^{-1} (from the (15,13) transition in Table 2) from 17261.8 cm^{-1} (from the (15,2) transition in Table 2). This allowed all of the observed bandhead transitions to be used in calculating the vibrational constants. The term values for each v'' level were then averaged together across v' levels and second-differences ($\Delta G_{v''}$) were calculated. A weighted least-squares curve fitting routine was used to fit the $\Delta G_{v''}$ values as a function of $(v'' + 1/2)$ to the three term rotationless Dunham expansion

$$E_{\text{vib}} = \omega_e(v''+1/2) - \omega_e x_e(v''+1/2)^2 + \omega_e y_e(v''+1/2)^3 \quad (35)$$

The spectroscopic constant ω_e is simply the vibrational frequency of the quantized energy levels for a harmonic oscillator. The spectroscopic constants $\omega_e x_e$ and $\omega_e y_e$ are added to empirically describe the anharmonicity of the molecular potential energy curve (42). Figure 12 shows a plot of the experimentally determined second differences ($\Delta G_{v''}$) from this work as a function of v'' , the least-squares fit from the molecular constants derived here and a fit to the Barrow molecular constants extrapolated to high v'' . The similarity of fit between both sets of constants is evident.

The $^{79}\text{Br}^{81}\text{Br}$ ground state spectroscopic constants derived from the current effort are reported in Table 3 along with those for $v'' \leq 10$ from Barrow (2). As can be seen, the current constants agree with Barrow's

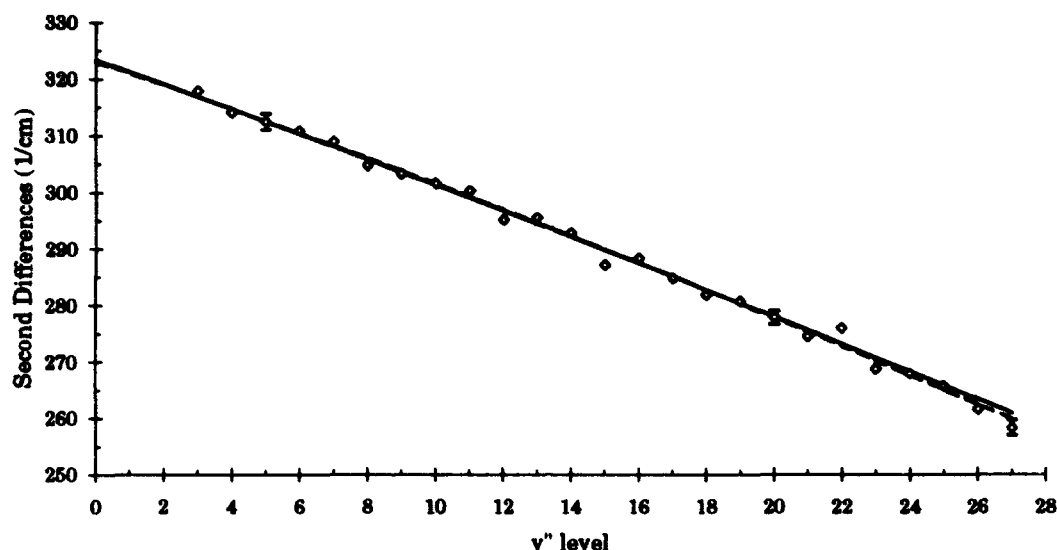


Figure 12. Plot of experimentally obtained second-differences \diamond and calculated values as a function of v'' . (—) current fit; (---) Barrow extrapolation

constants within the experimental error of the current work. Barrow and coworkers (2) did not report typical error bounds as such, however, they did state that the reported constants reproduce their rotationally resolved, high resolution absorption data to within 0.02 cm^{-1} .

The current effort was undertaken to extend the previously reported spectroscopic analyses to high v'' levels and determine if the previously reported ground state spectroscopic constants were adequate for describing the observed transitions. Vibrational analyses in the current work extended observed X state energy levels up to $v'' = 27$. The resolution achieved in the observed X state energy levels up to $v'' = 27$. The resolution achieved in the current study did not match that obtained by Barrow. However, the agreement between the two sets of molecular constants indicates that the values reported by Barrow can be extrapolated to high v'' levels. As an additional

Table 3

Spectroscopic constants for the $^{79}\text{Br}^{81}\text{Br}$ ground state from
the current work and Barrow and coworkers (2) (cm^{-1})

	Current Work	Barrow
ω_e	323.1 ± 1.5	323.3069
$\omega_e\chi_e$	1.02 ± 0.1	1.0641
$10^3 \omega_e y_e$	-3.77 ± 0.2	-2.2556

check on the agreement between the two sets of constants, especially for transitions to high v'' levels, energy levels and turning points for an RKR potential were calculated for both sets of molecular constants using the program from McFeeters (29). The results of these calculations are shown in Table 4. Agreement between the turning point values is excellent for the levels reported by Barrow. $G_{v''}$ levels vary somewhat but are within the experimental error of the current data, even to $v'' = 25$, where the larger $\omega_e y_e$ from the current work begins to affect the numbers significantly. The minor differences between the second difference fits and the general agreement of the RKR calculations strongly suggest that the Barrow values are also adequate for use even to high v'' . This result is not totally unexpected because the anharmonicity of the Br_2 ground state is small ($\omega_e\chi_e/\omega_e = 0.003$) and the $\omega_e y_e$ terms are also small. In similar experiments to these, McFeeters and coworkers found that high v'' levels in BrCl were also well described by molecular constants obtained for low v'' levels from high resolution absorption spectroscopy (29).

Table 4

RKR Potential Energies and Turning Points for the $^1\Sigma_g^+$ State of Br_2

v''	Current			Barrow		
	$G_{v'}$ cm^{-1}	r_{\min} (Å)	r_{\max} (Å)	$G_{v'}$ cm^{-1}	r_{\min} (Å)	r_{\max} (Å)
-1/2		2.2811			2.2811	
0	161.28	2.2320	2.3343	161.38	2.2320	2.3343
1	482.29	2.1984	2.3761	482.55	2.1984	2.3761
2	801.23	2.1763	2.4064	801.57	2.1764	2.4064
3	1118.08	2.1590	2.4320	1118.43	2.1590	2.4320
4	1432.81	2.1445	2.4549	1433.12	2.1445	2.4549
5	1745.41	2.1318	2.4760	1745.62	2.1318	2.4760
6	2055.85	2.1205	2.4957	2055.91	2.1205	2.4958
7	2364.10	2.1102	2.5145	2363.99	2.1102	2.5145
8	2670.15	2.1008	2.5324	2669.83	2.1007	2.5325
9	2973.97	2.0920	2.5497	2973.44	2.0920	2.5498
10	3275.53	2.0839	2.5665	3274.79	2.0838	2.5666
11	3574.83	2.0762	2.5829	3573.86	2.0761	2.5830
12	3871.83	2.0690	2.5989	3870.66	2.0689	2.5990
13	4166.51	2.0621	2.6146	4165.15	2.0620	2.6146
14	4458.84	2.0555	2.6300	4457.34	2.0554	2.6301
15	4748.82	2.0492	2.6451	4747.20	2.0492	2.6452
16	5036.41	2.0432	2.6601	5034.72	2.0432	2.6602
17	5321.59	2.0374	2.6749	5319.89	2.0374	2.6750
18	5604.33	2.0319	2.6896	5602.70	2.0319	2.6896
19	5884.62	2.0265	2.7041	5883.13	2.0265	2.7041
20	6162.44	2.0213	2.7186	6161.16	2.0213	2.7185
21	6437.75	2.0162	2.7329	6436.79	2.0163	2.7328
22	6710.55	2.0113	2.7472	6710.00	2.0114	2.7470
23	6980.80	2.0065	2.7614	6980.78	2.0067	2.7611
24	7248.48	2.0018	2.7756	7249.11	2.0020	2.7752
25	7513.57	1.9973	2.7897	7514.99	1.9975	2.7893
26	7776.04	1.9928	2.8038	7778.38	1.9931	2.8033
27	8035.89	1.9884	2.8179	8039.30	1.9888	2.8173
28	8293.07	1.9841	2.8320	8297.71	1.9846	2.8312
29	8547.57	1.9799	2.8461	8553.61	1.9805	2.8452
30	8799.37	1.9758	2.8602	8806.98	1.9764	2.8592

IV. Vibrational Energy Transfer in $\text{Br}_2 B^3\Pi (0_u^+)$

1 Introduction

Collisional energy transfer processes in the diatomic halogens and interhalogens have been studied extensively. $V \rightarrow T$ transfer studies in $\text{IF}(\text{B})$ (47), $\text{BrF}(\text{B})$ (30, 36) and $\text{BrCl}(\text{B})$ (33) have focused primarily on the potential of these species as short wavelength, chemically pumped lasing molecules. However, because of similarities in the three molecules, much can be learned by comparing experimentally determined vibrational transfer rates for different collision partners with various theoretical models such as the SSH theory and Landau-Teller theory described earlier. In this work, $V \rightarrow T$ energy transfer studies have been accomplished in $\text{Br}_2(\text{B})$ as an extension of the previous works. This chapter discusses state-to-state vibrational energy transfer studies in the non-predissociative vibrational levels ($v' \leq 3$) of the $\text{Br}_2(\text{B})$ electronic state with six different collision partners: $\text{Br}_2(\text{X})$, He, Ne, Ar, Kr and Xe. The spectrally resolved, temporally resolved fluorescence decay profiles from collisionally populated states observed in this study are adequately represented by the Montroll-Shuler model for vibrational transfer in an harmonic oscillator.

2 Experimental Arrangement

The experimental setup for the vibrational transfer experiments was essentially the same as in the spectroscopic experiments described in the

previous chapter. Only differences with the setup described in chapter II will be noted here.

2.1 Isotopically Enriched Br₂ and Gas Handling

As discussed in the previous chapter, the extremely dense absorption spectrum of Br₂ can be partly attributed to the presence of the three naturally occurring isotopic combinations in bromine, ⁷⁹Br₂, ⁸¹Br₂ and ⁷⁹Br⁸¹Br. The combination of overlapping vibrational bandheads for the various Br₂ isotopomers and the pump laser linewidth make the task of pumping single vibrational levels in the any of the three isotopomers quite difficult. To help reduce this problem, 100 ml of 90% atm. enriched ⁷⁹Br₂ was obtained to conduct the V→T studies. The isotopically enriched bromine was purified by repeated freeze-thaw cycles at 77 K. Because of the small initial amount of ⁷⁹Br₂ available, all experiments were performed at static cell pressures and additional vacuum system components including a second liquid N₂ cold trap were installed to recapture the ⁷⁹Br₂ for reuse. Buffer gases were added directly to the cell. All rare gases were research grade, 99.999% pure (Matheson).

2.2 Excitation System

Laser excitation for the vibrational transfer studies was provided by the same Spectra-Physics model PDL-3 pulsed dye laser and Quanta-Ray DCR-3 Nd:YAG pump laser combination described in the previous chapter. For these studies, the PDL-3 was reconfigured to use Exciton LDS 698 dye. The tuning range of this dye covered a wavelength range from 680–720 nm with an average output power of ≈ 20 mJ/pulse at 20 Hz. This was a significant increase in incident power compared with the ≈ 1 mJ/pulse used

by Clyne and coworkers (9) in their pulsed LIF study of the radiative lifetimes and collisional deactivation of the $\text{Br}_2 \text{ B}^3\Pi(0_u^+)$, $v' = 2$ state.

2.3 Detection System

The HR-640 monochromator was used exclusively with an RCA C31034 photomultiplier tube (PMT) to spectrally resolve the fluorescence as described in section 4.1 of chapter II. Unresolved fluorescence was also obtained as before except that the two 630 nm cutoff long-pass filters were replaced with two Corian 750 nm cutoff long-pass filters because of the longer pump wavelengths. Laser excitation spectra were collected with the PARC 165 Boxcar Integrator from both the unresolved and vibrationally resolved fluorescence PMTs. For the time resolved studies, both PMT outputs were connected to a LeCroy 9450, 350 MHz bandwidth, digitizing oscilloscope through two 100X PARC model 115 wide band preamplifiers. All temporal fluorescence waveforms were transferred to the DigiView 486DX50 personal computer for analysis via a National Instruments AT-GPIB board driven by a National Instruments LabWindows program.

3 Experimental Procedures

In this study, vibrational transfer within the non-predissociating levels ($v' \leq 3$) of $^{79}\text{Br}_2(\text{B})$ state was examined after excitation of two separate rovibrational levels via the $(v', v'') = (2, 4)$ and $(3, 5)$ vibrational transitions. Low populations in $v'' = 4$ and 5 ground state vibrational levels at room temperature limited the potential excited state population. Therefore, the fluorescence cell was heated with heat tape to between 95–100 °C in all $\text{V} \rightarrow \text{T}$ experiments. This increased the thermal population in the $v'' = 4$

level by a factor of 2 and significantly enhanced the observed emissions from the pumped and satellite vibrational states. A vibrational transfer emission spectrum recorded by scanning the monochromator from 7000 – 8500 Å using a fixed excitation wavelength is shown in Figure 13. This was used along with Coxon's Franck-Condon factors (14) to determine appropriate ($v' \rightarrow v''$) observation transitions that were sufficiently free of overlap from competing vibrational bands. It is clear from Figure 13 that transitions from odd numbered v' levels do not significantly overlap with even numbered v' level transitions, even at the 22.4 Angstrom resolution used in the current $V \rightarrow T$ transfer experiments. Selected (v', v'') transitions, computed overlap fractions and observation wavelengths are given in Table 5. No sufficiently isolated emissions from either the $v' = 0$ or 4 collisionally populated levels were observed in this study because of strong overlap with $v' = 2$ emissions within the spectral response range of the C31034 PMT. Overlap calculations are discussed further in Appendix C.

Spectrally and temporally resolved fluorescence waveforms were recorded over a variety of buffer gas pressures for each observation band. For the $v' = 3$ initially excited case, emissions were observed from $v' = 3$ and $v' = 2$. For the $v' = 2$ excited state, emissions were observed from $v' = 1, 2$ and 3. Waveforms were averaged over at least 1000 laser shots. Background subtraction was accomplished in two ways. First, 1000 laser shot averaged waveforms were collected with an empty cell and stored in the oscilloscope memory. Then, after each waveform with the Br_2 and buffer gas was collected, the background waveform was subtracted and the resulting waveform was stored on the computer. For the most part, this method worked well and eliminated most of the electrical noise generated by the

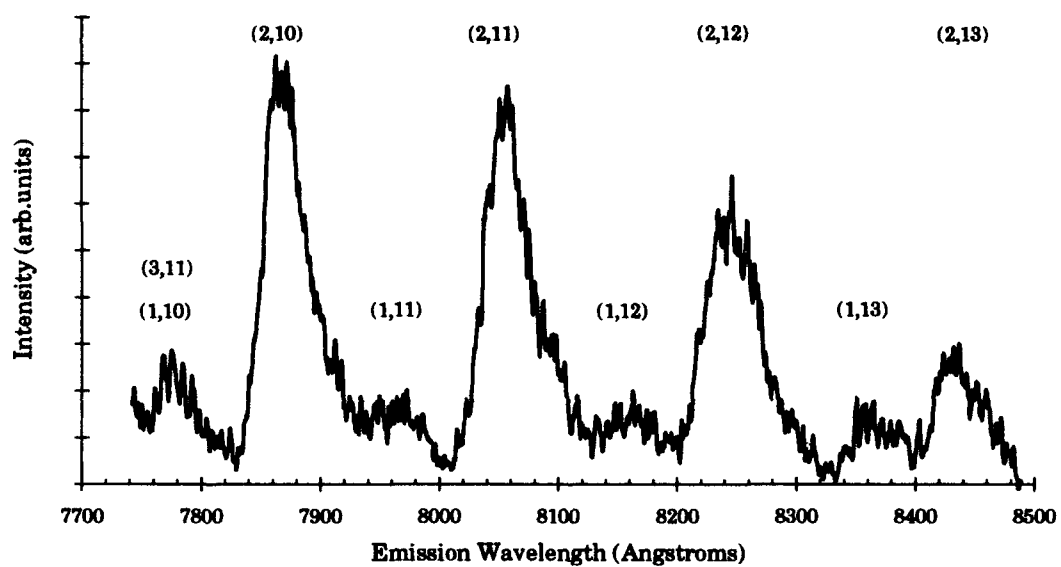
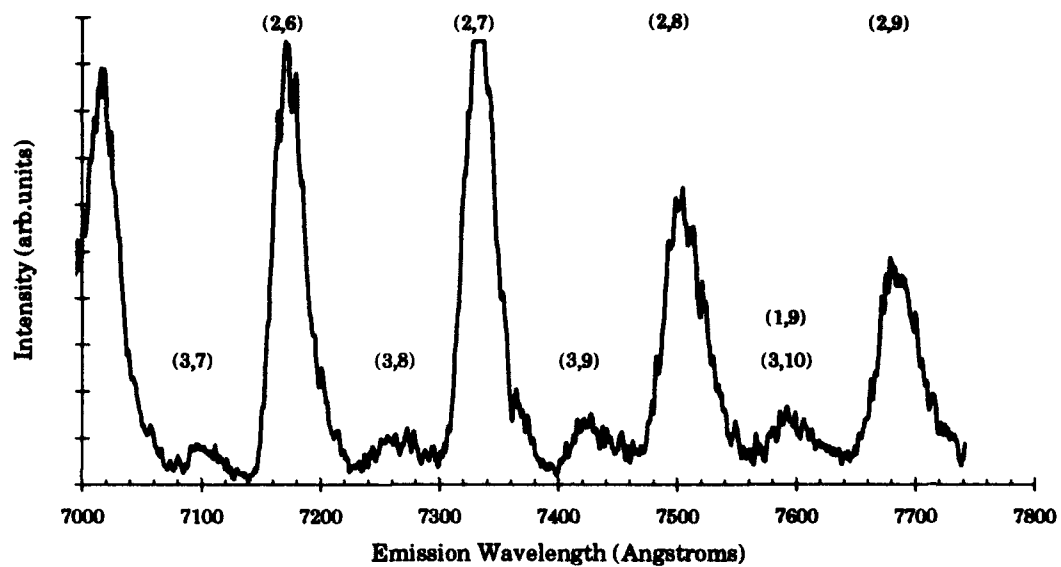


Figure 13. Vibrational transfer spectrum observed through 1 mm slits after populating $v' = 2$ at a pressure of 1.0 Torr Br_2 and 3.8 Torr Ar. Labels indicate (v', v'') transitions

Table 5

Spectral overlap fractions and observation wavelengths

Observed transition (v' , v'')	$v' =$	0	1	2	3	4	Monochromator Wavelength (\AA)
(1,12)		.00	.97	.00	.03	.00	8162
(2,11)		.09	.00	.90	.00	.01	7860
(3,9)		.00	.13	.00	.87	.00	7425

Nd:YAG laser operation. However, the empty-cell background noise traces did change somewhat over time and were usually only accurate for collecting a few $V \rightarrow T$ waveforms. This was a considerable inconvenience as multiple evacuations of the test cell were required while obtaining the thirty traces typically used to determine a single rate coefficient, significantly slowing the process. An alternative method was to obtain a background noise waveform for each $V \rightarrow T$ trace by tuning the laser away from the desired absorption line where the parent vibrational band could not be excited. This method provided more consistent subtraction of the electrical background noise, eliminated the need to continually reevacuate the test cell and was preferred over the first method. The signal-to-noise ratios for all of the vibrational transfer data were excellent. The minimum signal-to-noise ratio in any single waveform was four; typical values were greater than ten.

The Montroll-Shuler vibrational transfer model was implemented in the TableCurve software package from Jandel Scientific as a user defined

function (UDF) for the purpose of curve fitting (see Appendix B). The TableCurve implementation had several distinct advantages over the fitting routine used by Melton (30) and Perram et. al. (36) that outweigh the inability to fit to multiple vibrational bands simultaneously. The nonlinear least-squares fitting engine in TableCurve is extremely fast; fits to typical waveforms took only 2–3 minutes each for the Montroll-Shuler model. Fits were considerably faster for simple exponential and double exponential functional forms. The graphical interface also simplified the preparation each waveform required prior to fitting. Finally, statistical analyses were provided for all fit parameters to aid in error analysis. As discussed in the development of the Montroll-Shuler model in Appendix B, radiative and electronic deactivation effects can be accounted for by multiplying the analytic solution by a factor of $\exp(-\Gamma_0 t)$. Because of the lack of quenching data available for low v' levels in $\text{Br}_2(\text{B})$, Γ_0 was also included in the fitting routine as a fit parameter. Therefore, two energy transfer fitting parameters were provided from the TableCurve Montroll-Shuler model fitting routine, Γ_v and Γ_0 , for each fluorescence profile. Both Γ_v and Γ_0 were described earlier in chapter II as

$$\begin{aligned}\Gamma_v &= \sum_Y k_v^Y(1,0) Y \\ \Gamma_0 &= 1/\tau_0 = 1/\tau_r + \sum_Y k_q^Y Y\end{aligned}\tag{36}$$

4 Experimental Results

This section describes in detail the experiments conducted and results obtained in the current V→T transfer and electronic quenching study in the low v' levels of $\text{Br}_2(\text{B})$.

4.1 Laser Excitation Spectra

To properly determine collisional energy transfer rates from laser induced fluorescence traces, it is of critical importance to ensure initial excitation of only one excited electronic state vibrational level. Transfer into a collisionally populated state from multiple initially excited states can severely alter the observed fluorescence and render analysis techniques meaningless. Figure 14 shows a low resolution laser excitation spectrum of the $\text{Br}_2 (\text{B} \leftarrow \text{X})$ transition across a portion of the LDS 698 laser dye tuning curve at a cell pressure of 0.3 Torr. Vibrational transitions are labeled using spectroscopic constants from Barrow and coworkers (2).

It is clear from the ambiguous vibrational assignments in Figure 14 that greater resolution is needed to accurately determine suitable pump wavelengths for single vibrational band excitation. A problem occurs because the spectral response of the present total fluorescence detection system is non-uniform with respect to the different excited state vibrational levels. While the C31034 PMT used in this study has a relatively flat spectral response through the visible wavelengths out to 8800 Å, when combined with the long pass filters used to block scattered laser light, the total fluorescence detection system artificially emphasizes emissions from $v' = 1$ over $v' = 3$, making identification more difficult. This is caused by a large difference in the spectral overlap of the detection system pass band with strong emission

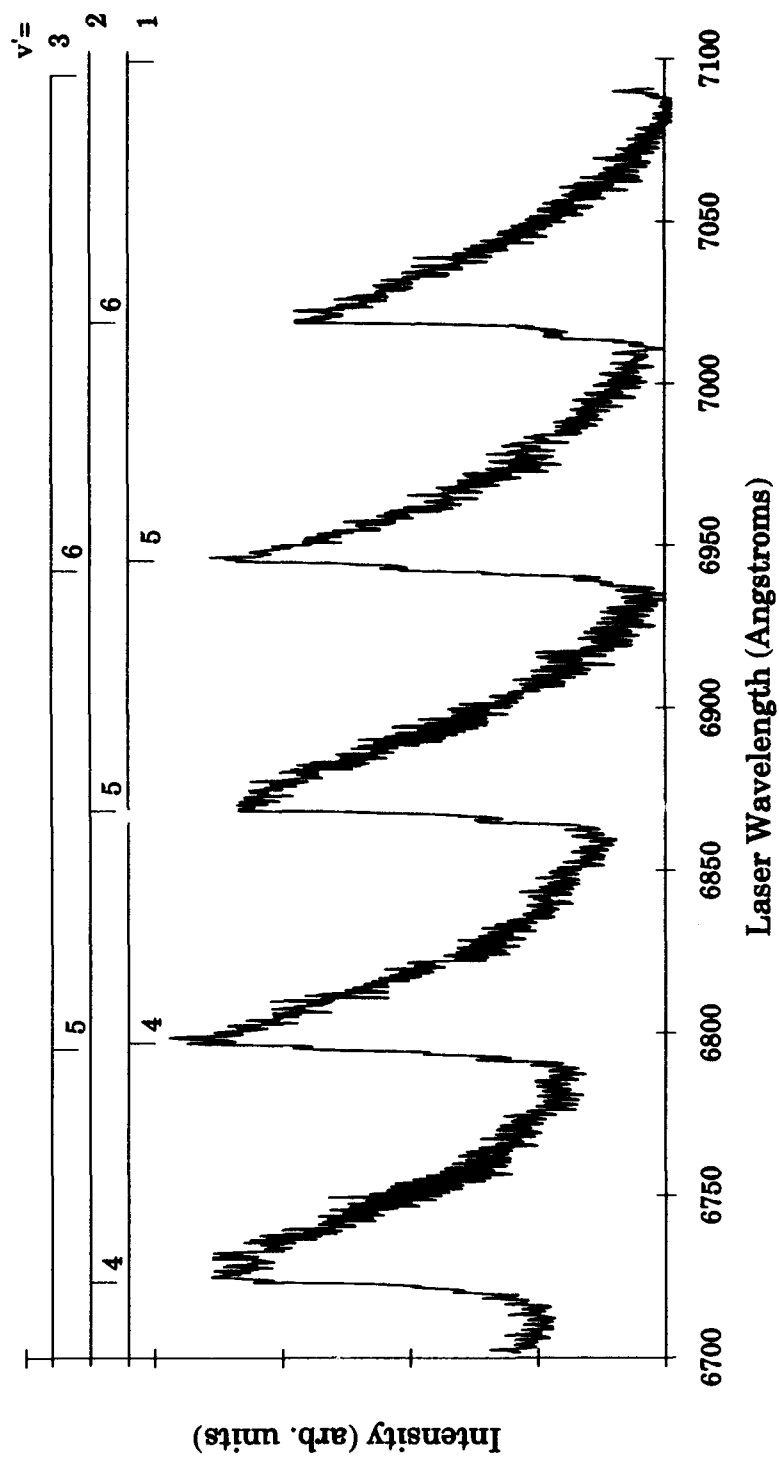


Figure 14. Total fluorescence laser excitation spectrum of the $\text{Br}_2(\text{B} \leftarrow \text{X})$ system from LDS 698 laser dye.

lines from each v' level. Another problem can arise from absorption overlaps with high J' levels of a preceding vibrational band. Therefore, to accurately identify vibrational states with acceptably isolated pump wavelengths, high resolution excitation spectra for the individual bandhead regions were collected by spectrally resolving the emissions through the monochromator using the transition wavelengths listed from Table 5. Example of this technique are shown in Figures 15-17. These figures examine excitation of $v' = 3, 2$ and 1 , respectively, for laser excitation wavelengths near the (3,5) and (1,4) vibrational bandheads. Note that even near the bandheads, the spectra show sufficient resolution for rotational assignment using Barrow's rotational constants (2). Figure 16 shows that high J' transitions of the (2,4) vibrational band, in particular the P(80) and R(85) transitions, must also be avoided to ensure selective excitation of a single excited state vibrational level. The (3,5) P(8) and R(13) transitions which overlap at 6796.4 \AA were used as the excitation transitions for the vibrational transfer studies from $v' = 3$. Similar spectra were used to identify the (2,4) P(6) and R(11) absorption lines which overlap at 6724.1 \AA as the excitation transition for the $v' = 2$ studies.

4.2 $V \rightarrow T$ Transfer With $\text{Br}_2(X)$ as Collision Partner

Vibrationally resolved fluorescence decay profiles were obtained from $v' = 2$ and 3 for the initially populated $v' = 3$ level and from $v' = 1, 2$ and 3 for the initially populated $v' = 2$ as a function of Br_2 pressure. Br_2 pressures for the pump $v' = 3$, view $v' = 2$ (or p3v2) data ranged from 400–2100 mTorr. For the p2v1 and p2v3 data, Br_2 pressures ranged from 520–3000 mTorr and 470–2650 mTorr, respectively. Low pressure limits were driven by poor signal-to-

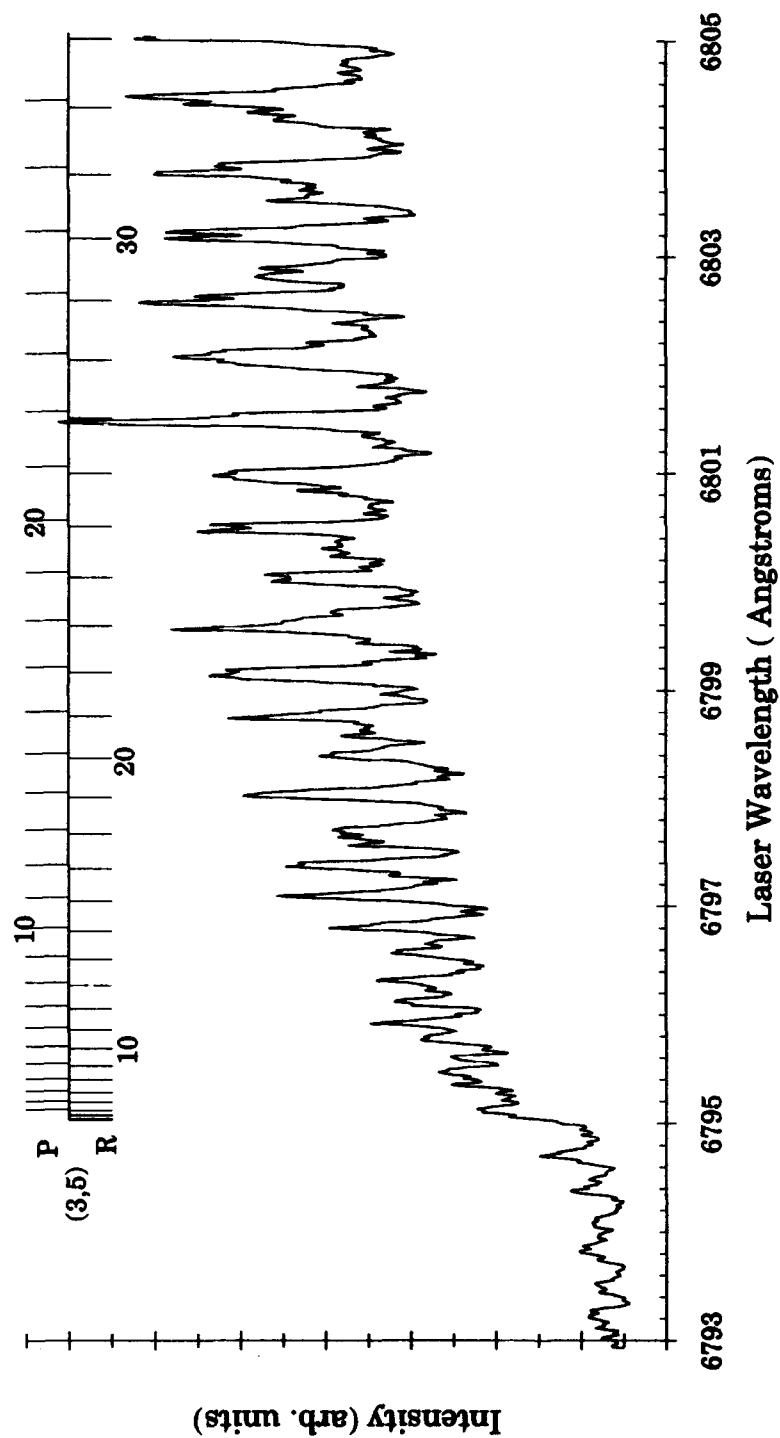


Figure 15. Vibrationally resolved excitation spectra of $v'=3$ near the (3,5) and (1,4) bandheads.

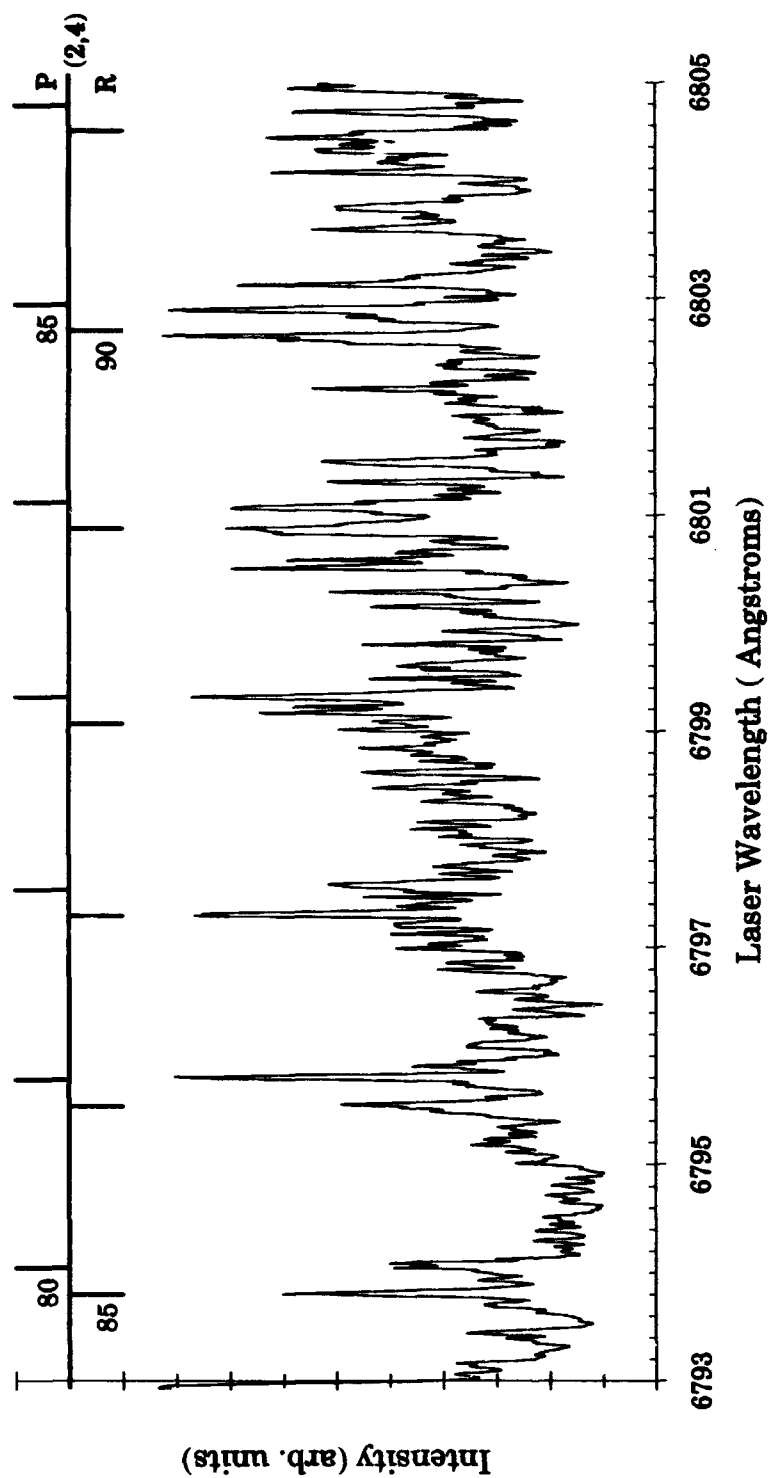


Figure 16. Vibrationally resolved excitation spectra of $v'=2$ near the (3,5) and (1,4) bandheads.

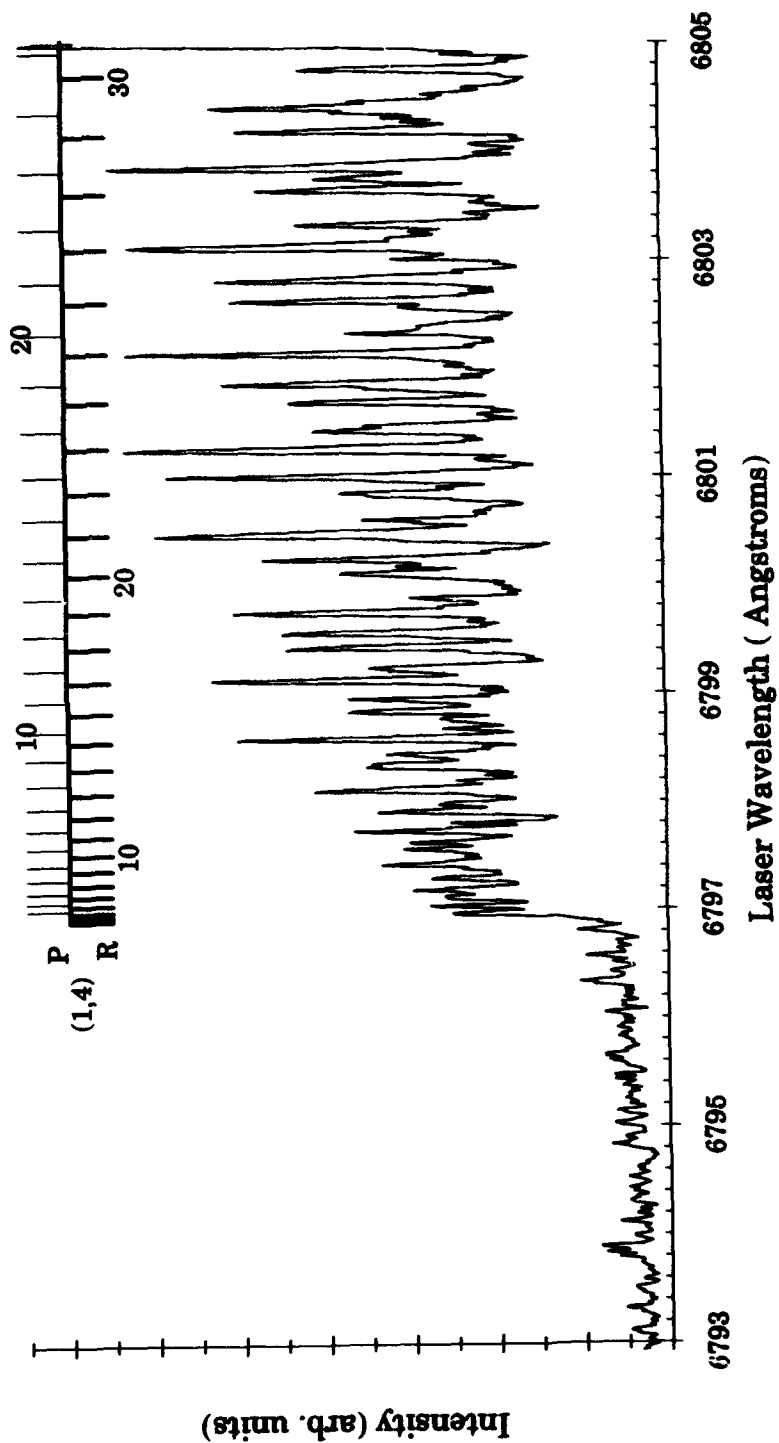


Figure 17. Vibrationally resolved excitation spectra of $v' = 1$ near the (3,5) and (1,4) bandheads.

noise ratios from the satellite state emissions. Pressures for the p3v3 and p2v2 data sets were much lower, ranging from 20-800 mTorr, because of the increased signal strength of the initially populated levels. Typical resolved fluorescence decay profiles are shown in Figure 18 for $v' = 2$ and Figure 19 for $v' = 3$ and 1 emissions after initially populating $v' = 2$ at a Br_2 pressure of 660 mTorr. Figure 19 provides direct evidence of strong coupling within the non-predissociative levels of the $\text{Br}_2(\text{B})$ vibrational manifold as emissions were observed from collisionally populated vibrational levels above and below the initially excited level. The relatively short timescales in Figures 18 and 19 are also indicative of the short radiative lifetime of $\text{Br}_2(\text{B})$ and suggest that strong electronic removal processes may also be present. The delayed decay of the $v' = 1$ fluorescence with respect to the $v' = 3$ fluorescence also suggests that the collisional transfer out of a particular vibrational level increases with increasing vibrational quantum number.

The simplest possible mechanisms describing the temporal evolution of collisionally populated vibrational states like those shown in Figure 19 are the low pressure approximation and radioactive decay analogy described by Eq (32) (see chapter 2, section 3.3.2.1). However, in the current experiments, multiple collisions conditions are certainly probable. Additionally, in strong vibrational coupling cases, it is inappropriate to simply attribute the observed exponential rise and fall rates to the transfer rate into and out-of the observed state. Inverse reactions up the vibrational ladder ($v' \rightarrow v' + 1$) are evident in Figure 19 and suggest that repopulation of the parent level from collisionally populated levels ($v' \pm 1 \rightarrow v'$) may be important as well. Therefore, neither of these models provide acceptable physical descriptions of vibrational transfer in $\text{Br}_2(\text{B})$.

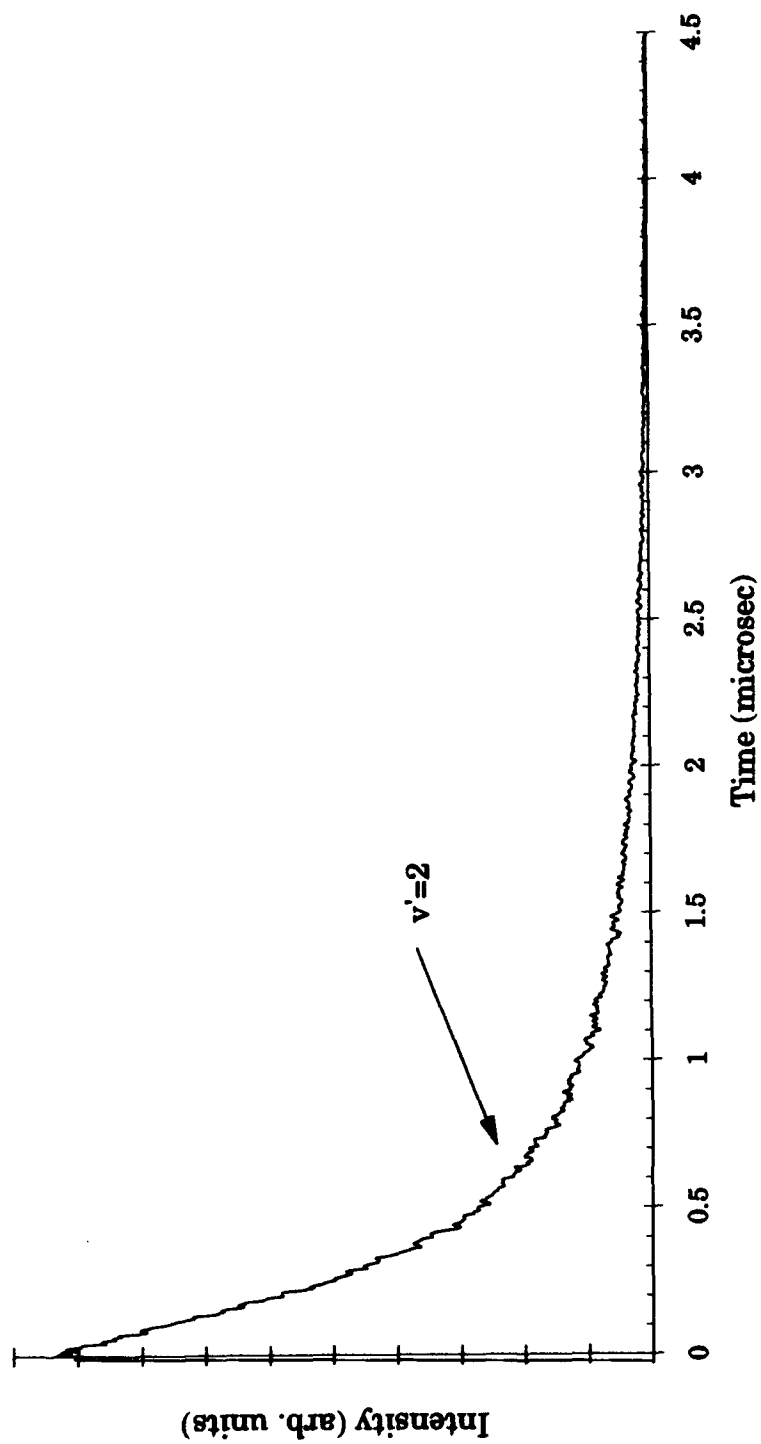


Figure 18. Spectrally resolved, temporally resolved fluorescence profile for $v' = 2$ after initial excitation of $v' = 2$ at 660 mTorr of Br_2

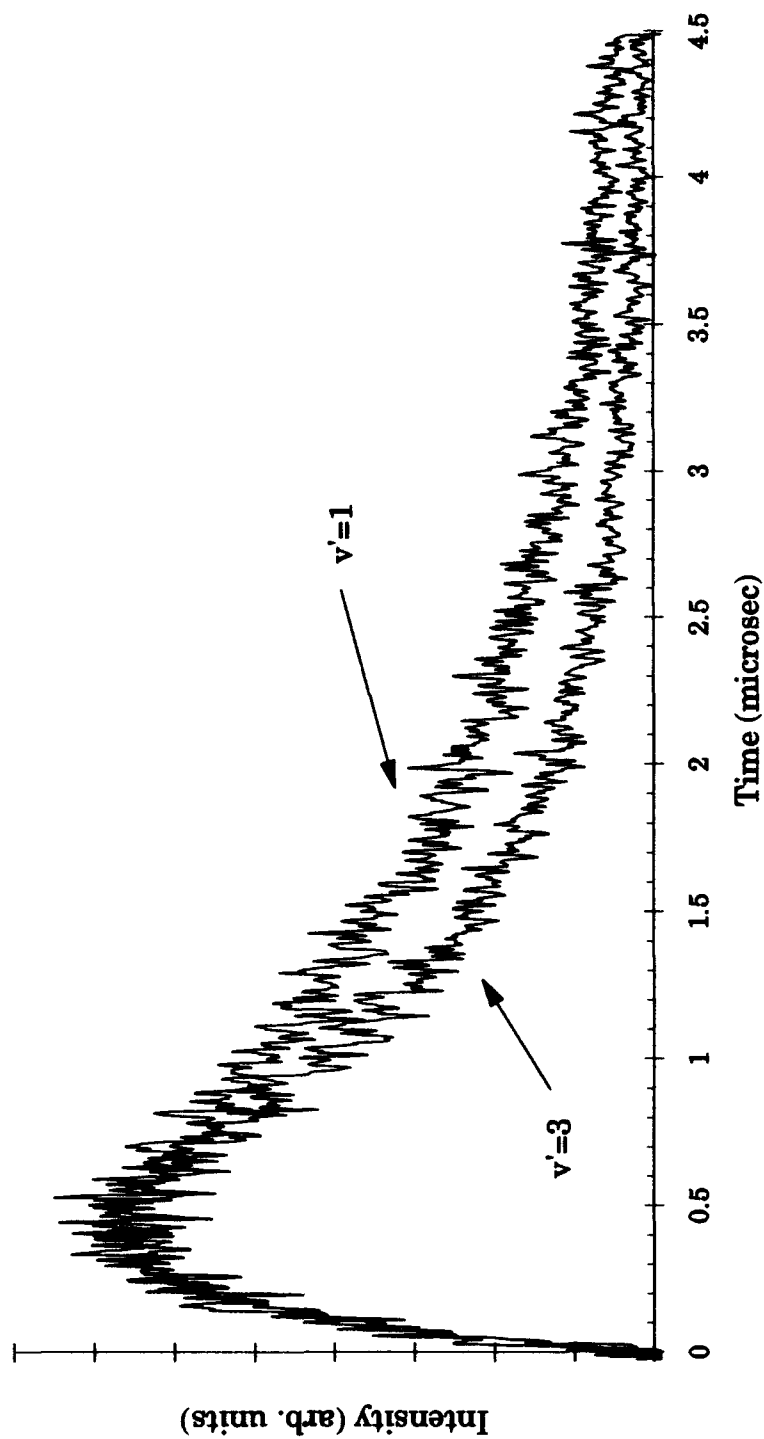


Figure 19. Spectrally resolved, temporally resolved fluorescence profiles for $v' = 1$ and 3 after initial excitation of $v' = 2$ at 660 mTorr of Br_2

4.2.1 Montroll-Shuler Fits

The TableCurve implementation of the Montroll-Shuler model described in Appendix B was used to fit all observed fluorescence waveforms. The fitting routine was tested to insure the accuracy of the implementation over a wide range of possible quenching and vibrational transfer rates by using Mathematica to generate noise-free simulated intensity vs. time data for the Montroll-Shuler equation in Eq (33). The simulated data was input to TableCurve and the Montroll-Shuler model fitting routine was applied. In all cases, the TableCurve fitting routine extracted the exact same quenching and vibrational transfer rate coefficient values used to generate the data. Although it was initially unclear whether Montroll-Shuler would be an adequate model for the strongly coupled $\text{Br}_2(\text{B})$ state, it is currently the only analytic solution to the master rate equation for vibrational transfer and certainly warranted investigation. Figures 20–25 show typical fits to collisionally populated satellite states with $\text{Br}_2(\text{X})$ as the bath gas. Figures 20, 22 and 24 are typical of fits to the higher pressure traces for the p3v2, p2v3 and p2v1 cases, respectively. Figures 21, 23 and 25 are typical of fits at lower pressures for the same three pump/view level combinations. As can be seen, the quality of fit is outstanding in all cases. More will be said later in this chapter about the applicability of the Montroll-Shuler model to vibrational transfer in $\text{Br}_2(\text{B})$.

4.2.2 Total Removal from Initially Excited Levels

Fluorescence decay profiles from the initially populated $v' = 2$ and 3 states were also investigated to determine total removal rate coefficients, k_{TR} , from these levels. A single exponential decay function as in Eq (27) was fitted to the $v' = 3$ data. The single exponential fits to the $v' = 3$ emissions

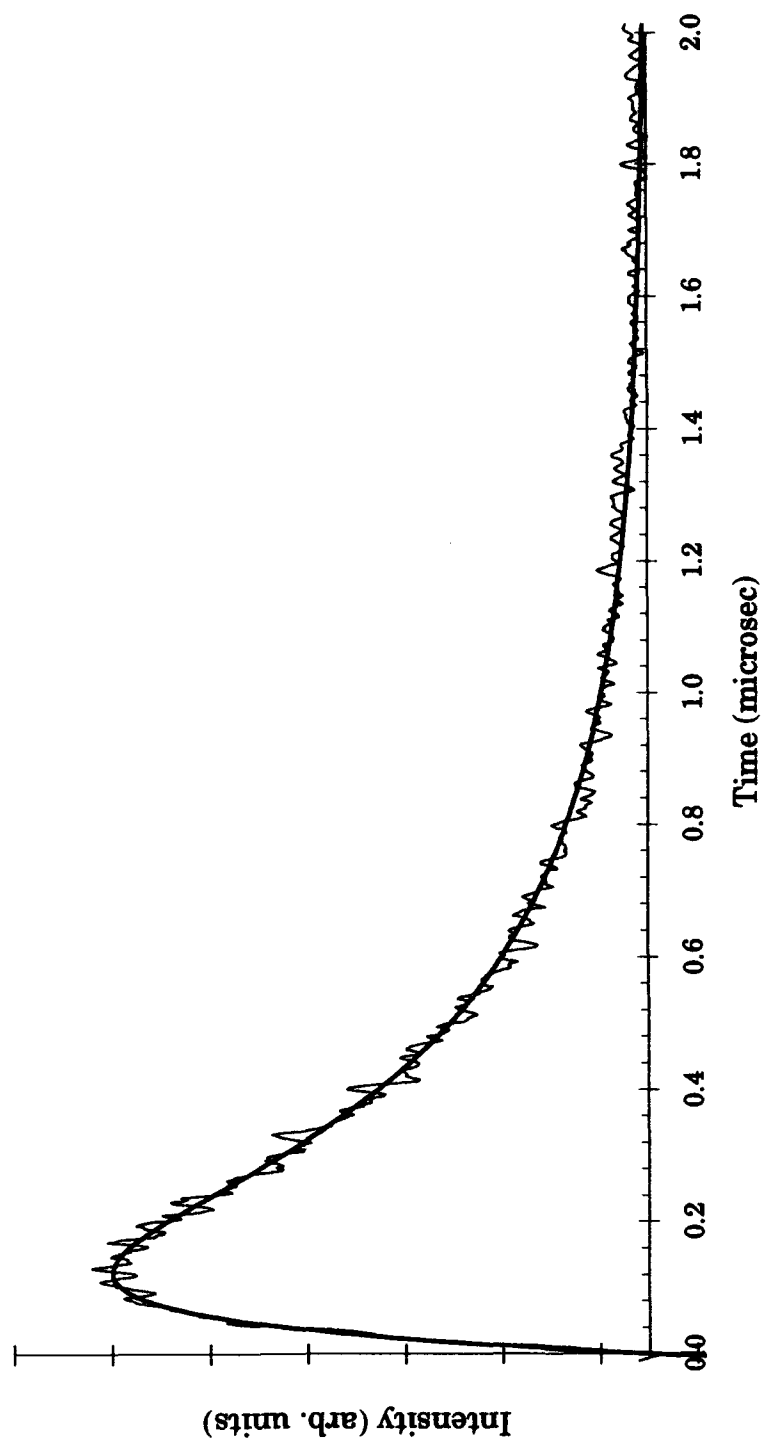


Figure 20. Montroll-Shuler fit to emissions from the (2-11) band transition after initial excitation of $v'=3$ with a Br_2 pressure of 1.68 Torr.

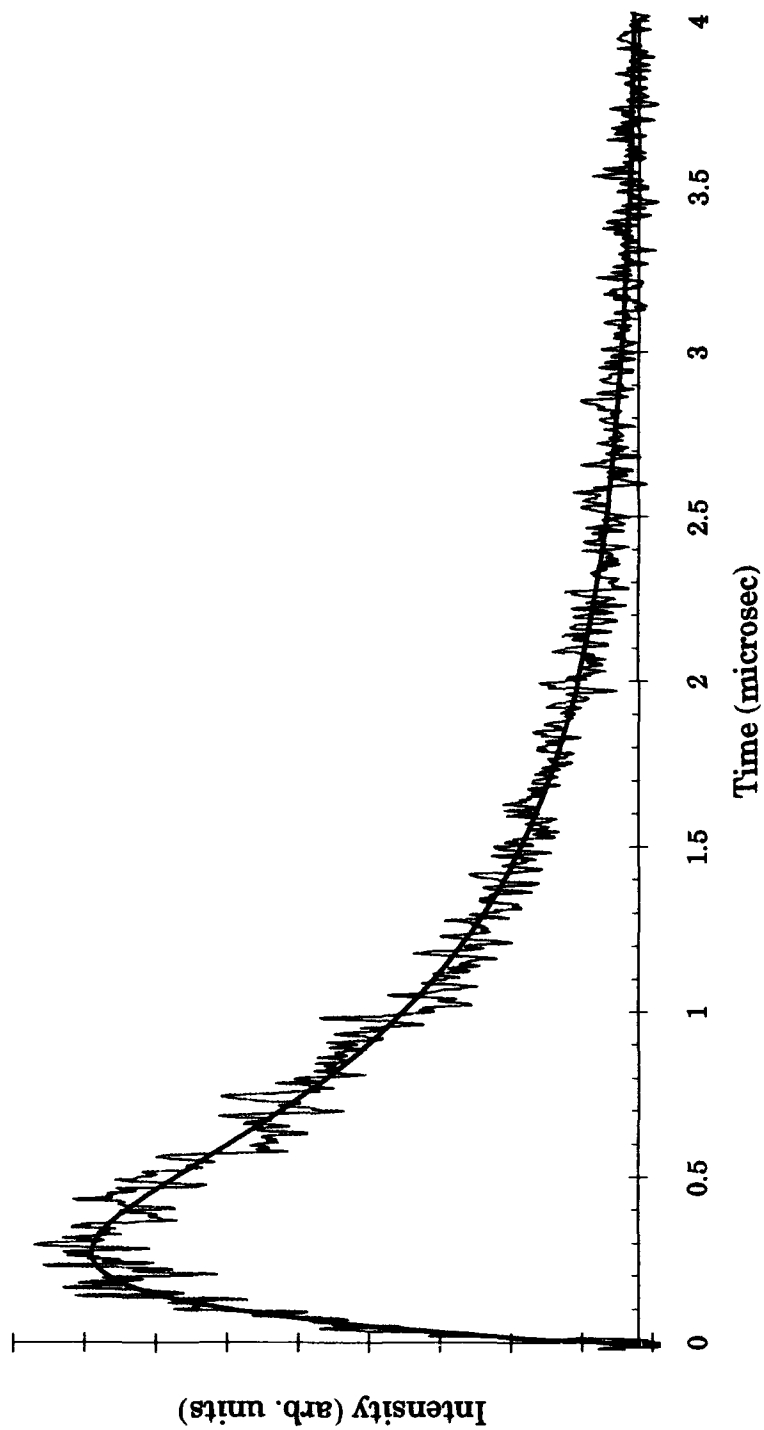


Figure 21. Montroll-Shuler fit to emissions from the (2-11) band transition after initial excitation of $v'=3$ with a Br_2 pressure of 724 mTorr

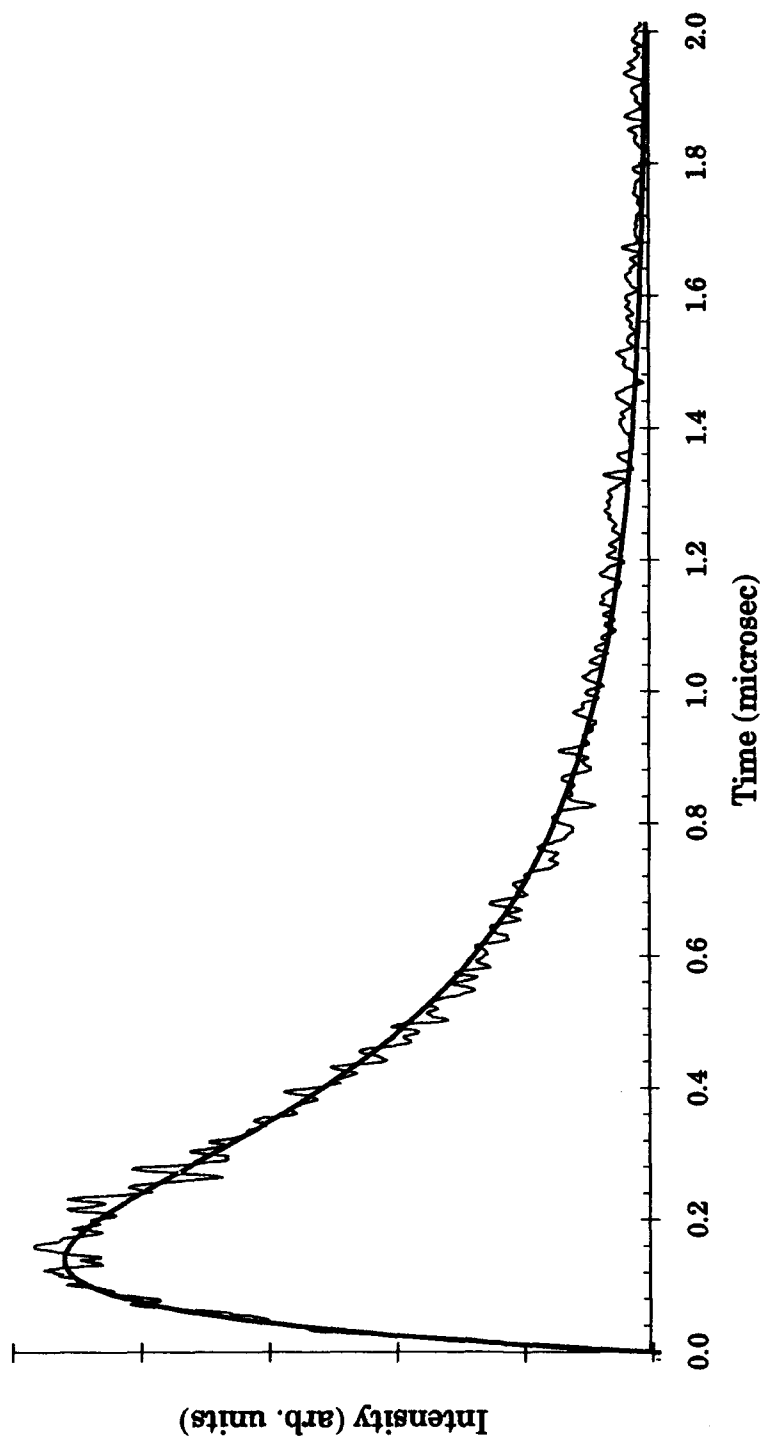


Figure 22. Montroll-Shuler fit to emissions from the (3-9) band transition after initial excitation of $v'=2$ with a Br_2 pressure of 1.97 Torr

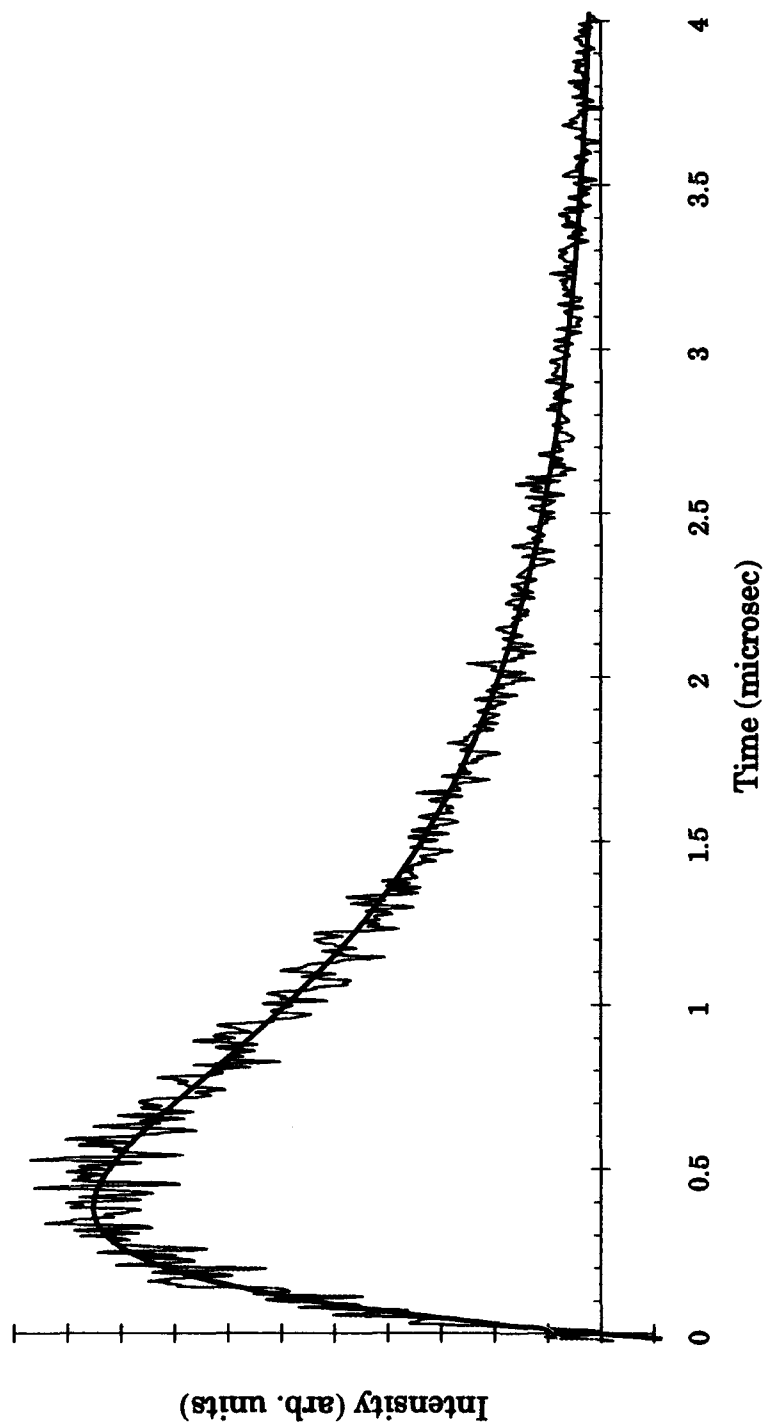


Figure 23. Montroll-Shuler fit to emissions from the (3-9) band transition after initial excitation of $v'=2$ with a Br_2 pressure of 660 mTorr

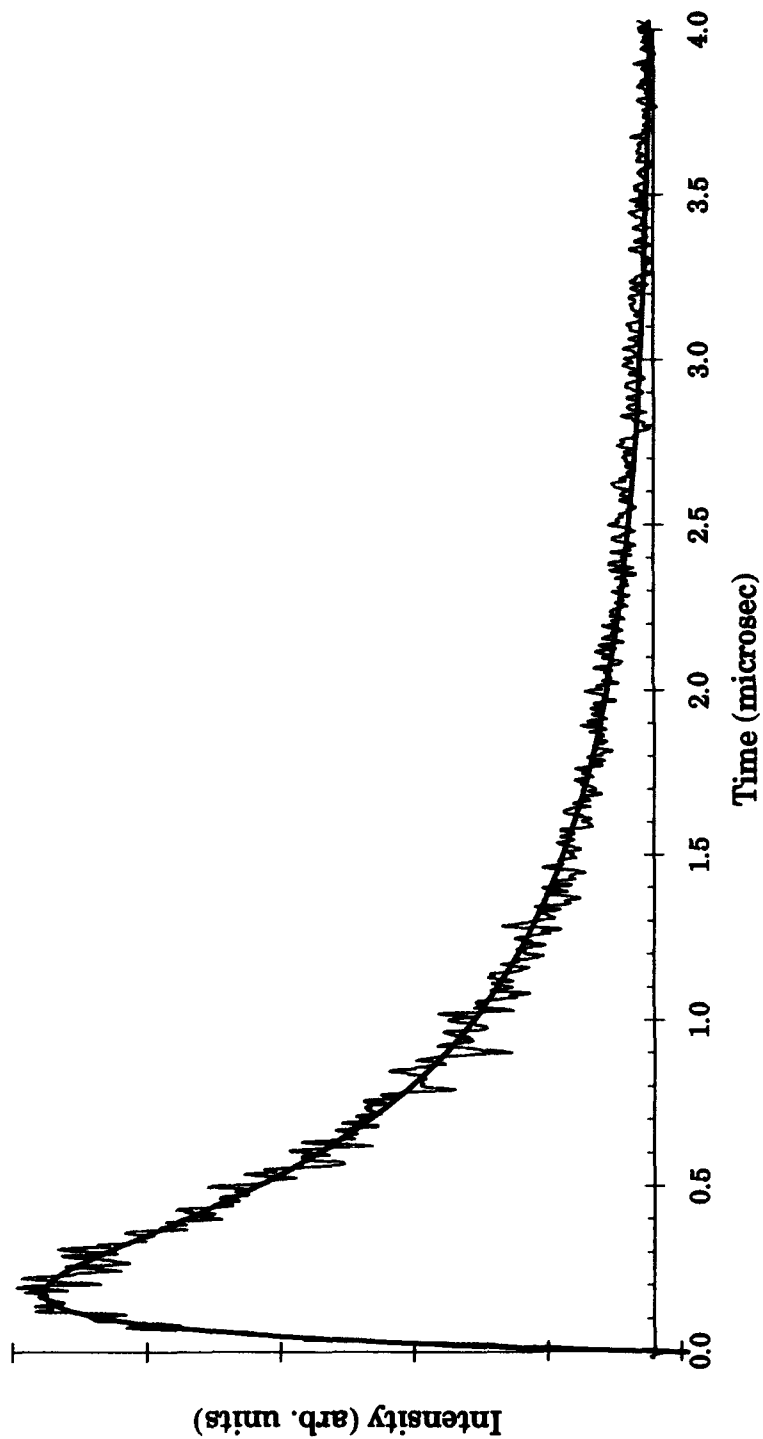


Figure 24. Montroll-Shuler fit to emissions from the (1-11) band transition after initial excitation of $v'=2$ with a Br_2 pressure of 2.06 Torr

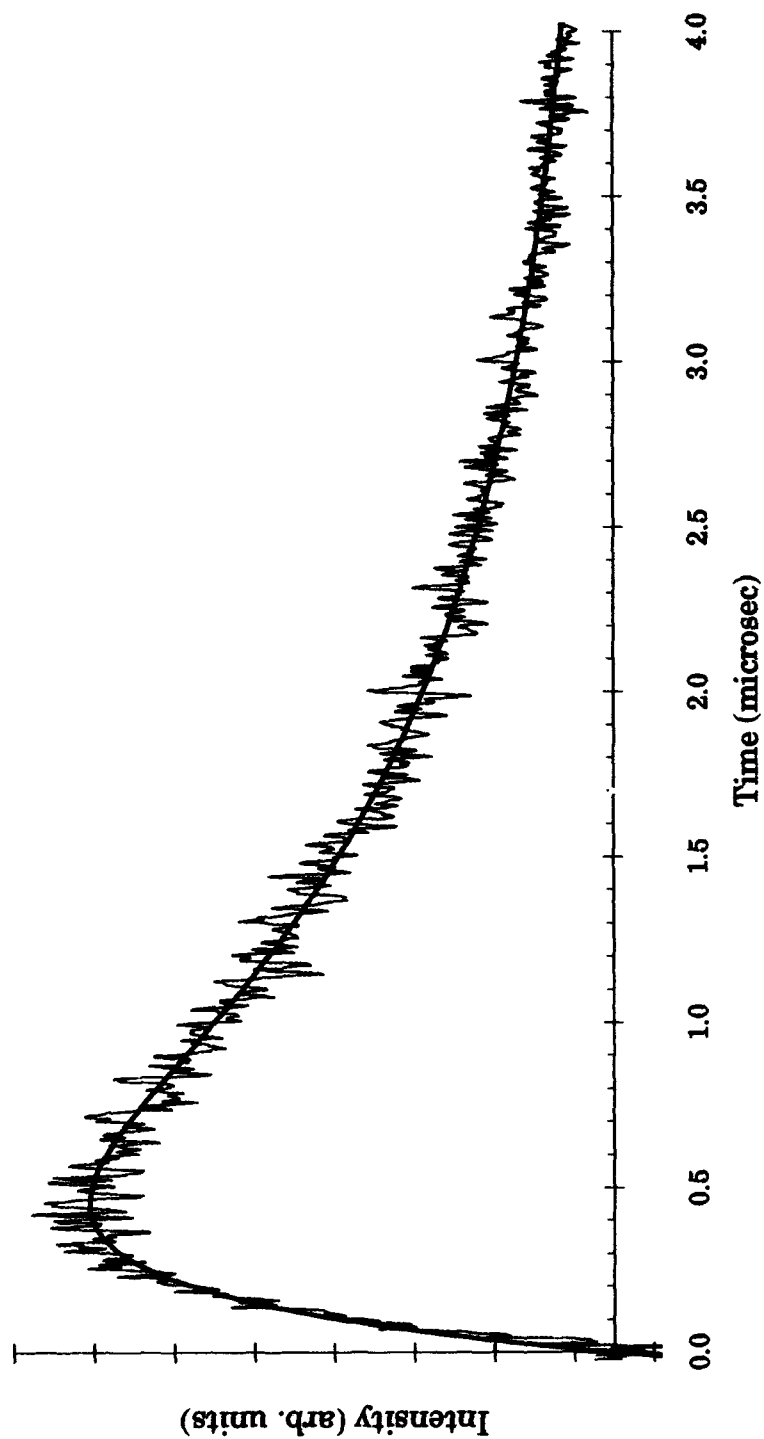


Figure 25. Montroll-Shuler fit to emissions from the (1-11) band transition after initial excitation of $v'=2$ with a Br_2 pressure of 780 mTorr

with Br_2 collision partners were quite good for 3–4 fluorescence decay e -folds over the entire pressure range examined. This suggests that only a very small amount of transfer occurs back into $v' = 3$. Stern-Volmer plots of the inverse lifetimes obtained from these fits also scaled linearly with pressure. The slope of the Stern-Volmer plot gives the total population removal rate out of $v' = 3$. Emissions from the pump $v' = 2$, view $v' = 2$ data were not single exponential, indicating that a significant amount of vibrational transfer back into $v' = 2$ is present. The $v' = 2$ data did fit quite well to a sum of two decaying exponential terms. At early times, the excited state population is primarily in $v' = 2$ and little repopulation of $v' = 2$ from other v' levels has occurred. Therefore, to a rough approximation, the initial, rapidly decaying exponential term may be related to the total removal rate from $v' = 2$. Examples of fits to parent level emissions are shown in Figures 26 and 27.

4.2.3 Stern-Volmer Analysis of Montroll-Shuler Data

Each observation band discussed above was investigated over a range of pressures and the data were fitted to the Montroll-Shuler model. The fitting routine extracted values for Γ_v and Γ_0 , the fundamental vibrational transfer rate and the electronic removal rate, respectively, for each time profile. It is clear from Eq (33) that the fundamental vibrational transfer rate coefficient, $k_v(1,0)$, is the slope of a plot of Γ_v versus buffer gas concentration (or pressure). Similarly, the assumed vibrationally independent quenching rate, k_q , can be obtained from the slope of a plot of Γ_0 versus buffer gas concentration. Figures 28 and 29 show combined results of the Stern-Volmer analysis for $k_v(1,0)$ and k_q , respectively, from several pump $v' = 3$, view $v' = 2$ experiments with $\text{Br}_2(\text{X})$ collision partners. These

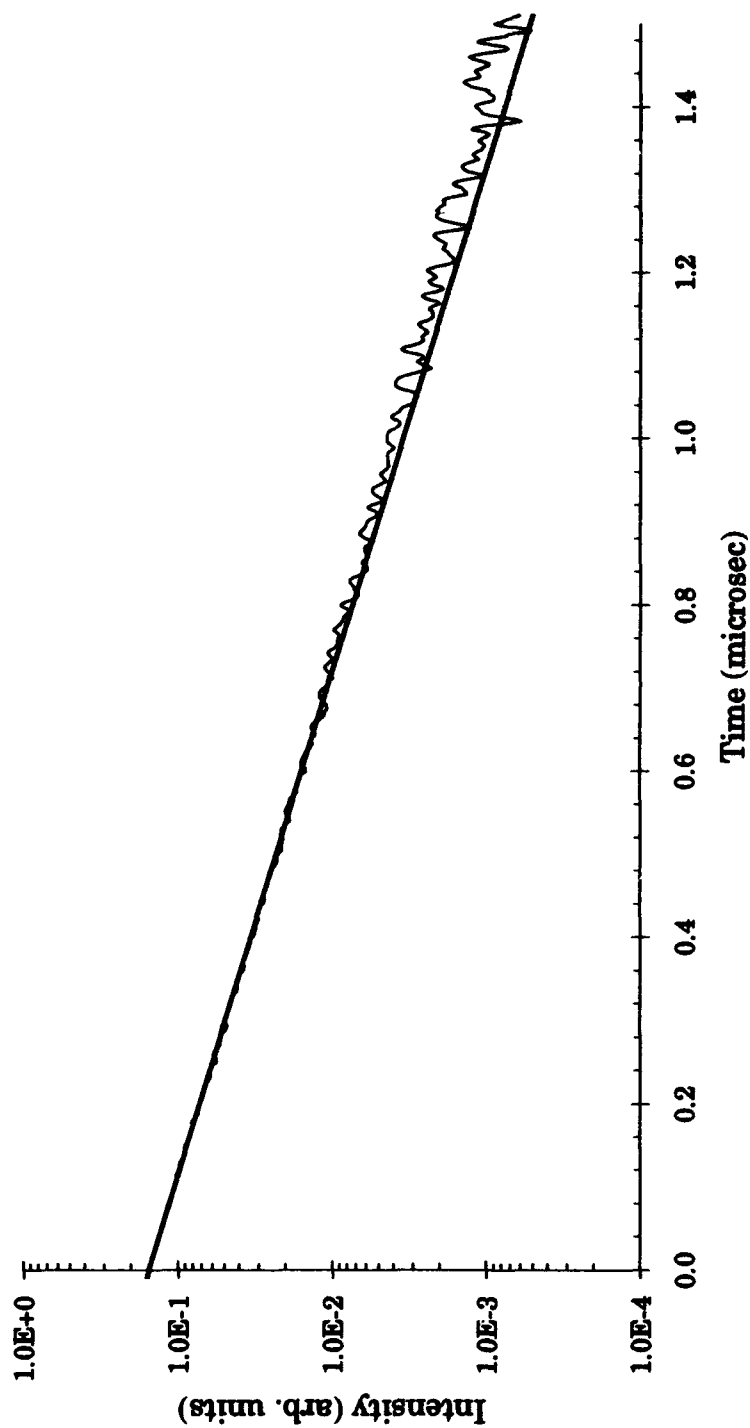


Figure 26. Single exponential decay fit to emissions from the $v' = 3$ parent state for Br_2 pressure of 656 mTorr

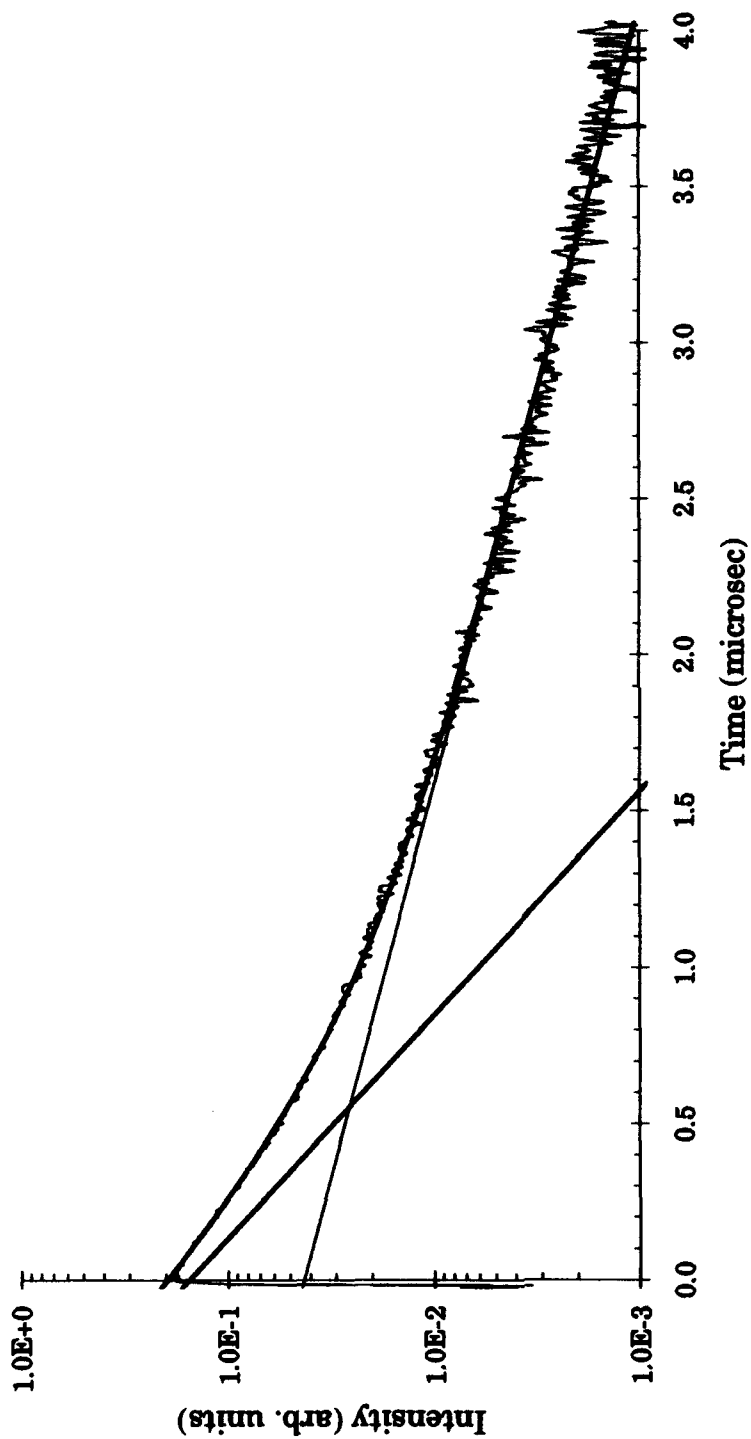


Figure 27. Double exponential decay fit to emissions from $v' = 2$ parent state for Br_2 pressure of 576 mTorr

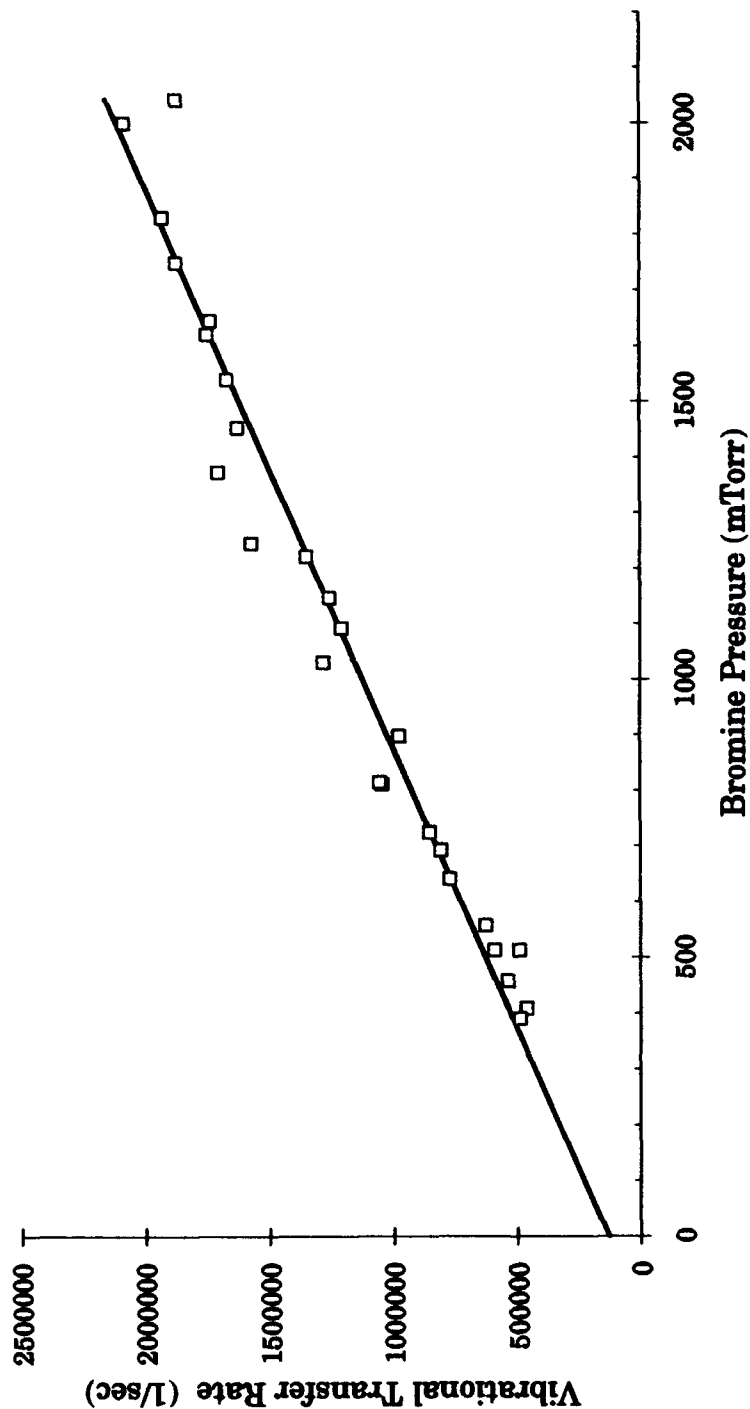


Figure 28. Stern-Volmer plot of the Montroll-Shuler vibrational transfer fits to the combined pump $\nu' = 3$ view $\nu' = 2$ data with $\text{Br}_2(\text{X})$ buffer gas that gives $k_v(1,0) = 3.6 (\pm 0.2) \times 10^{-11} \text{ cm}^3/\text{molec}\cdot\text{sec}$

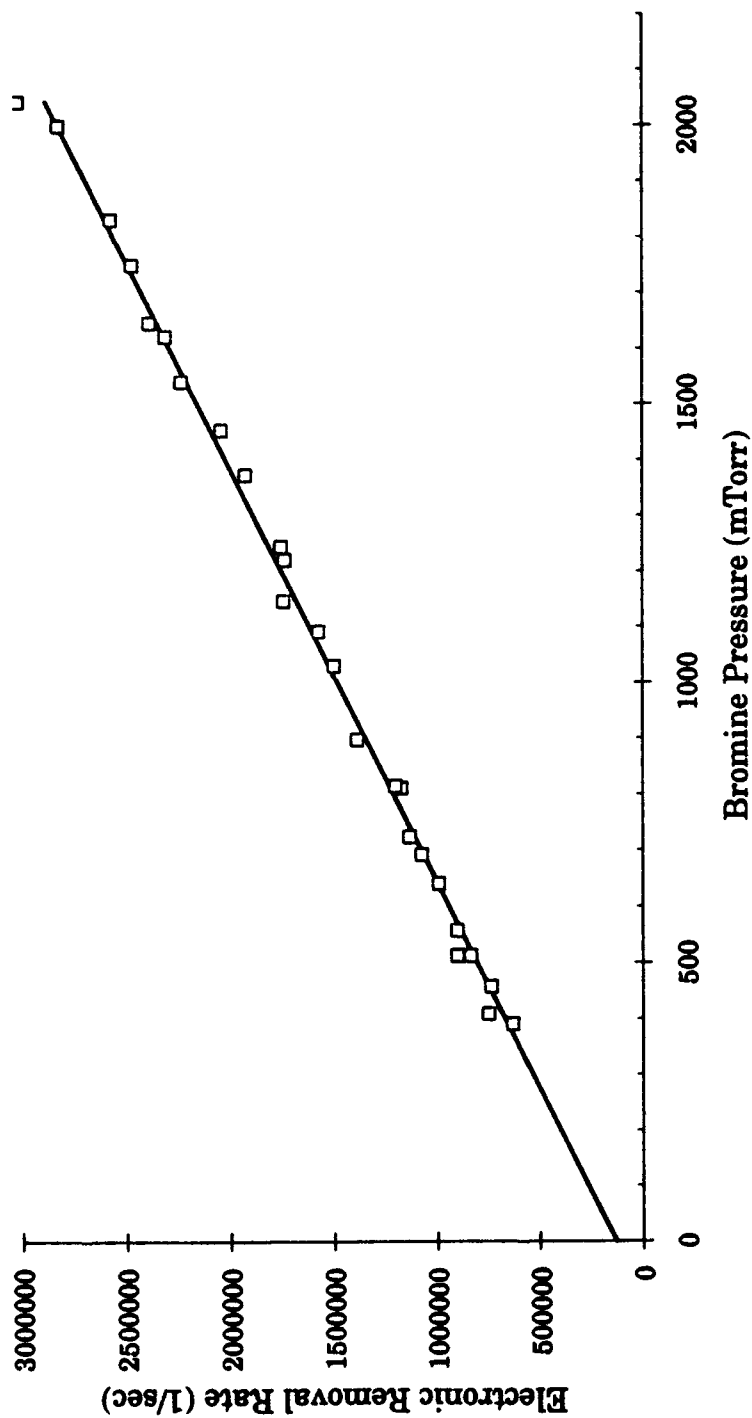


Figure 29. Stern-Volmer plot of the Montroll-Shuler electronic quenching fits to the combined pump $v'=3$ view $v'=2$ data with $\text{Br}_2(\text{X})$ buffer gas $k_q = 5.0 (\pm 0.2) \times 10^{-11} \text{ cm}^3/\text{molec}\cdot\text{sec}$ and $\tau_r = 7.6 (\pm 2.8) \mu\text{sec}$

figures both show that the linearity and repeatability of the experimentally determined rates are excellent for the p3v2 data. Stern-Volmer plots for the other pump-view level combinations were of similar quality. Ideally, the zero-pressure intercept of the $k_v(1,0)$ plot should be zero. In practice, however, this is not always the case. Factors such as uncompensated overlap from competing vibrational bands and differences in vibrational level quenching rates and radiative lifetimes can cause positive intercepts. The zero-pressure intercept of the electronic quenching plots provides the collision-free lifetime of the observed vibrational level. However, large extrapolations in buffer gas pressure are required to obtain the zero pressure intercepts. The sensitivity of the intercept values to minor variations in the quenching rate precludes the use of this method for determining collision-free lifetimes.

Similar analyses to those just described were accomplished for each pump-view level combination. Stern-Volmer plots from the combined data sets of similar experiments were analyzed to provide the reported rate coefficients for electronic quenching and vibrational transfer as well as total removal rate coefficients from the $\text{Br}_2(\text{B})$ parent levels with $\text{Br}_2(\text{X})$ as collision partner. Table 6 summarizes these rate coefficients for the $\text{Br}_2(\text{X})$ collision partner work. The error quoted in Table 6 is the standard deviation of the slopes or intercept values from the Stern-Volmer plots for the combined data sets. The reported total removal rate coefficient out of $v' = 2$ is the faster of the two observed rates from the double exponential decay fits. Reported radiative lifetimes are the intercepts of the Stern-Volmer plots for electronic removal from collisionally populated states. More will be said about the magnitudes of the various kinetic rate coefficients later on.

Table 6

Fundamental vibrational transfer rate coefficients, total removal rate coefficients, electronic quenching rate coefficients ($10^{-11}\text{cm}^3/\text{molec}\cdot\text{sec}$) and collision-free lifetimes (10^{-6} seconds) from $\text{Br}_2(\text{B})$ collisions with $\text{Br}_2(\text{X})$

v' pump/ view	$k_v(1,0)$	$k_v(p,v)$	k_{TR}	k_q	τ_r
2 / 3	3.1 ± 0.1	5.1 ± 0.2	25.8 ± 1	4.2 ± 0.1	4.7 ± 0.8
3 / 2	3.6 ± 0.4	10.8 ± 1.1	25.5 ± 2	5.0 ± 0.1	7.6 ± 2.8
2 / 1	4.1 ± 0.1	8.2 ± 0.2		2.1 ± 0.1	6.6 ± 2.6

4.3 $V \rightarrow T$ Transfer With Rare Gas Collision Partners

Vibrational transfer studies with rare gas collision partners were accomplished in the same manner as in the self-transfer study discussed above. The rare gases were chosen as collision partners for several reasons. Inert, monatomic collision partners eliminate the possibility of chemical reaction or $V \rightarrow V$ transfer. Electronic states in the rare gases are also not energetically accessible. Therefore, for these experiments, the primary difference between the rare gases is nuclear mass, making comparisons with kinetic energy transfer models such as the SSH and Landau-Teller theories possible. Results can also be compared with previous $V \rightarrow T$ transfer studies in other interhalogens with rare gas collision partners. These various comparisons are discussed later in this chapter. Of the rare gases considered, argon was studied most extensively. Virtually identical

experiments to those in the self-transfer study were performed with argon as buffer gas. Helium, neon, krypton and xenon were also investigated but to a lesser extent than argon.

4.3.1 Argon

Argon was studied more thoroughly than the other rare gases, primarily for comparisons with previous works. It is also considered typical because it falls in the middle of the range of atomic masses for the rare gases. The procedure for the rare gas investigations differed only slightly from the self-transfer experiments. Small amounts of $^{79}\text{Br}_2$, usually about 500 mTorr, were introduced into the fluorescence cell. Buffer gases were added to the cell and fluorescence profiles were recorded as before. Rare gas partial pressures ranged from 0–4 Torr for all of the rare gases. This was a wider range than was typically used in the self-transfer study (0.5–3 Torr) due to the lower quenching efficiency of the rare gases.

As in the self-transfer case, the Montroll-Shuler model was fit to all emission waveforms from collisionally populated vibrational levels. Since only the buffer gas concentration was changed over a given set of waveforms, the Stern-Volmer analysis used to extract the appropriate rate coefficients was identical to that previously discussed with one exception. The zero-pressure intercepts from the Stern-Volmer plots for both vibrational transfer and electronic quenching provide no real information concerning the buffer gas. As before, the Montroll-Shuler model produced excellent fits to the experimental data. Stern-Volmer plots for quenching and vibrational transfer were linear. Typical curve fits and Stern-Volmer plots for the rare gas collision partners are shown in Appendix D. Table 7 summarizes the

Table 7

Fundamental vibrational transfer rate coefficients , total removal rate coefficients and electronic quenching rate coefficients ($10^{-11} \text{ cm}^3/\text{molec}\cdot\text{sec}$) from $\text{Br}_2(\text{B})$ collisions with Argon

v' pump /view	$k_v(1,0)$	$k_v(p,v)$	k_{TR}	k_q
2/3	3.7 ± 0.5	5.8 ± 0.8		$1.0 \pm .16$
3/2	2.5 ± 0.3	7.5 ± 0.9	20 ± 1	0.88 ± 0.16
2/1	2.3 ± 0.1	4.6 ± 0.2		$.28 \pm 0.07$

rate coefficients obtained from the Montroll-Shuler fitting routine for collisions with argon.

Parent level emissions from the $v' = 2$ level in an argon buffer also displayed the two term exponential decay behavior noted in the self-transfer study. The data were again fitted to two decaying exponential terms as before to determine a total removal rate from the pumped level. The total removal rate from $v' = 2$ is also reported in Table 7. The slower of the two exponential rates, $1.9 \pm 0.1 \times 10^{-11} \text{ cm}^3/\text{molec}\cdot\text{sec}$, will be discussed further later.

4.3.2 Helium, Neon, Krypton and Xenon

The remaining rare gases were studied in less detail because the Montroll-Shuler model fit the argon data so well. For helium, neon, krypton

and xenon, only the $v' = 3$ level was pumped while observations were made from both $v' = 2$ and 3 for rare gas pressures up to ~ 3 Torr. Again, both the Montroll-Shuler and double exponential models provided excellent fits to the experimental data and linear Stern-Volmer plots. Examples are also shown in Appendix D. Table 8 gives the rate coefficients derived for the rare gas collision partners other than argon.

Table 8

Fundamental vibrational transfer rate coefficients and electronic quenching rate coefficients (10^{-11} cm³/molec-sec) from Br₂(B) collisions with various rare gases

rare gas	$k_v(1,0)$	$k_v(3,2)$	k_n
He	2.5 ± 0.3	7.6 ± 1.0	$0.80 \pm .12$
Ne	2.5 ± 0.2	7.4 ± 0.6	0.87 ± 0.06
Kr	2.8 ± 0.2	8.3 ± 0.5	0.67 ± 0.08
Xe	3.1 ± 0.4	9.4 ± 1.1	0.75 ± 0.11

5 Discussion of Br₂(B) Vibrational Transfer Results

The experiments described in the previous sections indicate that the Montroll-Shuler model adequately describes V→T transfer in the lower vibrational levels ($v' \leq 3$) of the Br₂(B) electronic state for both Br₂(X) and rare gas collision partners. The fundamental vibrational transfer rate

coefficients and average electronic quenching rate coefficients for each collision partner studied are summarized in Table 9. The error bounds indicate the standard deviation for each term. The error reported for Br₂(X) and argon are somewhat higher than for the other collision partners. However, the values in Table 9 for both Br₂(X) and argon were averaged over all of the pump/view level combinations where, in general, the spread in $k_v(1,0)$ and k_q values was somewhat greater than the repeatability of the data within a given pump/view combination.

Table 9

Fundamental vibrational transfer rate coefficients and electronic quenching and (10^{-11} cm³/molec-sec) for Br₂(B) with various collision partners

Collision Partner	$k_v(1,0)$	$\sigma_v(1,0)/\sigma_g$	k_q
Br ₂ (X)	3.6 ± 0.4	.2	3.7 ± 1.2
He	2.5 ± 0.3	.048	$.80 \pm .12$
Ne	2.5 ± 0.2	.097	$.87 \pm 0.6$
Ar	2.9 ± 0.7	.13	$.80 \pm .3$
Kr	2.8 ± 0.2	.15	$.66 \pm 0.8$
Xe	3.1 ± 0.4	.17	$.75 \pm .11$

5.1 Validity of Montroll-Shuler Model for Br₂

Several factors contribute to accepting the Montroll-Shuler model as an adequate description of vibrational transfer in Br₂(B). In previous studies of state-to-state V→T transfer in the interhalogens, particularly BrF (30, 36) and IF (47), emissions were observed from several collisionally populated

vibrational states after excitation of a single parent vibrational level. The data in these studies were rather noisy and the fits to the Montroll-Shuler model were only satisfactory. However, because of the consistent $k_v(1,0)$ rate coefficients obtained from the various v' levels, the Montroll-Shuler model was determined to adequately represent vibrational transfer in both BrF and IF. In the current work, experimental considerations (primarily, the spectral overlap of emissions from the parent v' level and emissions from collisionally populated levels with $\Delta v' = \pm 2$) prohibited observation of emissions from collisionally populated vibrational levels with $|\Delta v| > 1$ from the parent level. However, the quality of the data (i.e., high signal-to-noise ratios) obtained from $\Delta v' = \pm 1$ levels helped to compensate for the limited range of excited and observed v' levels. The quality of the nonlinear fits to the Montroll-Shuler model was much better for the current experiments than in the BrF (30, 36) and IF (47) experiments. In addition, the Stern-Volmer plots of the fundamental $V \rightarrow T$ transfer rates and the electronic quenching rates were all linear for all the cases considered. This linearity serves to validate the scaling of $V \rightarrow T$ transfer rates with vibrational level which is an essential feature of the Montroll-Shuler model. Also, no systematic variation in the experimental rate coefficients with respect to either the pumped or observed vibrational levels was noted. Finally, as will be discussed more later, the values for $k_v(1,0)$ for both Br₂ and the rare gas collision partners using the Montroll-Shuler model are consistent with the trends previously reported in the BrF, BrCl and IF vibrational transfer studies discussed above.

5.2 Deficiencies of the Montroll-Shuler Model for Br₂

The discussion in the previous section builds a fairly strong case for acceptance of the Montroll-Shuler model as an adequate description of V→T transfer in the non-predissociative vibrational levels of Br₂(B). It is also important to understand the inherent deficiencies of the Montroll-Shuler model for Br₂ and estimate their magnitudes. Examination of satellite state emissions on logarithmic plots clearly shows deviation from the Montroll-Shuler fits, particularly at longer times and higher buffer gas concentrations. Figures D.27–D.31 in Appendix D show typical examples from the rare gas studies of this deviation, where the observed signal intensities are slightly higher than predicted by the Montroll-Shuler fits. The deviations from the Montroll-Shuler fits were somewhat stronger for the lighter rare gases than for xenon and almost unnoticeable in the pure bromine work. The deviations were not present in the bromine-only emission profiles taken during the rare gas studies and became more pronounced as the partial pressure of the buffer gas was increased.

Possible explanations for the observed deviations from the Montroll-Shuler model were also considered in this study. The simplest explanation for the observed increase in fluorescence intensity at longer times would be the presence of systematic errors in the data from incorrect assignment of the absolute zero reference values for the observed intensities. Even a rather small positive offset in the zero reference can significantly alter the shape of a logarithmic plot, especially for small signals. In the current work, the same zeroing procedure was used for all buffer gas species at all pressures. Such offset errors would likely be present, therefore, in practically all of the data. However, as was noted earlier, the observed deviations from Montroll-Shuler

were both pressure dependent and buffer species dependent. It is unlikely, therefore, that such systematic errors could account for the observed pressure dependence of the deviations.

Another possible explanation for the observed deviations from Montroll-Shuler was that the effects of predissociation in the vibrational manifold, which are totally excluded by the Montroll-Shuler model, must be considered. In order to investigate this, several numerical models including various amounts of predissociation were developed using Mathematica. These models are discussed completely in Appendix B. Briefly, the lower $\text{Br}_2(\text{B})$ vibrational levels ($0 \leq v' \leq 6$) were modeled as a simple, n-level Montroll-Shuler system with vibrational state independent electronic quenching and spontaneous emission. Vibrational levels at and above the first predissociation level, v_{pd}' ($v_{\text{pd}}' = 4$ for the four level model ($v' = 0, 1, 2$ and 3), $v_{\text{pd}}' = 5$ for the five level model, and so on), were eliminated and all $V \rightarrow T$ transfer to vibrational levels $v' \geq v_{\text{pd}}'$ were assumed to immediately predissociate and were lost from the systems. Eigenvalues and eigenvectors for the rate matrices were calculated and numerical solutions were obtained of the form

$$x_i(t) = \sum_{j=0}^{j_{\text{max}}} C_j u_i^j \exp(\lambda_j \Gamma_v t) \exp(\Gamma_o t) \quad (37)$$

where

$j_{\text{max}} = n - 1$ is the highest nonpredissociative vibrational level

C_j are coefficients determined from the initial conditions

$x_i(t)$ is the normalized temporal profile of the observed state

u_i^j is the i^{th} element of the j^{th} eigenvector of the n-level rate matrix

λ_j is the j^{th} eigenvalue of the n -level rate matrix

Γ_v and Γ_o are the fundamental $V \rightarrow T$ transfer rate and the electronic removal rate defined in chapter II

The predissociative models in the form of Eq (37) were implemented into TableCurve as user-defined functions with the same fitting parameters as the Montroll-Shuler model, namely Γ_v and Γ_o .

The rationale for investigating the truncated vibrational manifold models was twofold. First, the use of vibrational state independent electronic removal rates (quenching and spontaneous emission) and Montroll-Shuler scaling for the $V \rightarrow T$ rate matrix elements allowed for closed form solutions of $x_i(t)$ with fit parameters corresponding directly to those of Montroll-Shuler model. This made direct comparison of the $V \rightarrow T$ and electronic quenching rate coefficients from the truncated models and the Montroll-Shuler model possible. Second, the examination of several models truncated at different v_{pd}' levels made it possible to bracket the values for the $V \rightarrow T$ transfer and electronic quenching rate coefficients. It should be noted that none of the truncated vibrational manifold models is any more or less of an exact representation of the actual low v' $\text{Br}_2(\text{B})$ manifold than the Montroll-Shuler model since the $\text{Br}_2(\text{B})$ state is known to have over 50 vibrational levels, most of which are predissociate to some extent. However, the truncated manifold models do account for, albeit rather abruptly, vibrational level dependent electronic removal (i.e., predissociation) not considered in the Montroll-Shuler model alone.

The five level and seven level truncated manifold models were initially fit to the pump $v' = 3$, view $v' = 2$ data from the Br_2 collision partner work.

Stern-Volmer plots for $V \rightarrow T$ transfer and electronic removal are shown in Figures 30 and 31. The agreement between the seven level and Montroll-Shuler systems is within a few percent for both rate coefficients. The values for the $k_v(1,0)$ and k_q rate coefficients from the five level and Montroll-Shuler systems differ by $\sim 15\%$ and $\sim 25\%$ respectively. It is clear, from these figures at least, that the seven level system is a reasonably good approximation of the infinite vibrational manifold of the Montroll-Shuler model.

All four n -level systems were also fit to pump $v' = 3$, view $v' = 2$ data with argon collision partners where deviations from Montroll-Shuler fits had been observed. In all cases, the truncated models provided a better fit to the data than the Montroll-Shuler model, although the differences were rather small. The primary difference between the truncated models and Montroll-Shuler was the agreement with the data at long times. Figure 32 is a linear scale representation of early-time fits that shows how each of the five models provide reasonable fits to the strongest fluorescing region. Figure 33 is a semilog plot of the same data that shows the differences between the fits, particularly at long times. The fact that the observed fluorescence in Figure 33 decays more slowly than the Montroll-Shuler model predicts is reasonable. The effective electronic removal rate is larger at early times ($< 2 \mu\text{sec}$) because the system is under non-equilibrium conditions and a significant number of the $\text{Br}_2(\text{B}, v' = 3)$ state molecules are being transferred up the vibrational ladder to predissociative states. At later times ($> 2 \mu\text{sec}$), the $\text{Br}_2(\text{B})$ state is approaching thermal equilibrium and the observed intensity is not affected by predissociation, yielding a slower fluorescence decay. Since the Montroll-Shuler does not allow for state-dependent electronic removal and the fits are affected more strongly by the rapidly changing early time

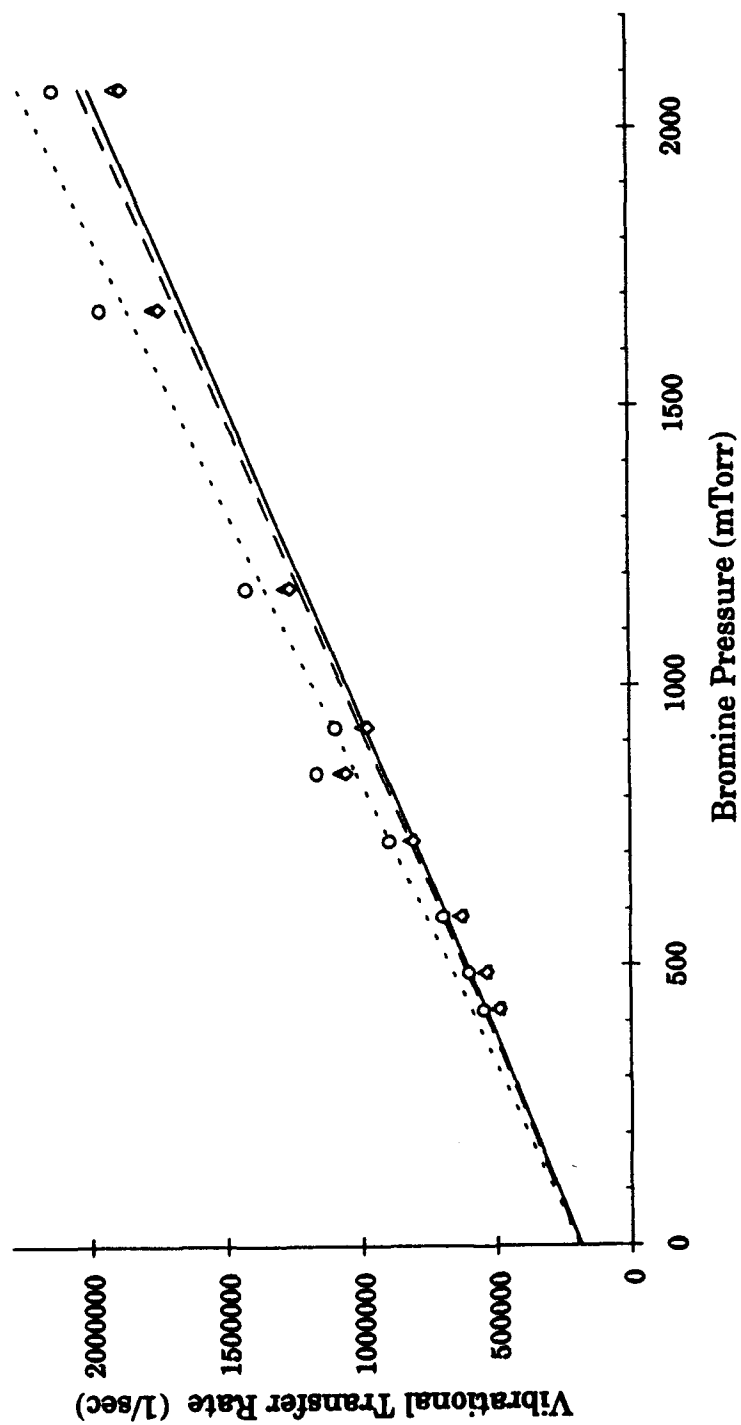


Figure 30. Stern-Volmer $V \rightarrow T$ transfer plots for five level (data (o), fit (---)), seven level (data (Δ), fit (—)) and Montroll-Shuler (data (◇), fit (—)) models for p3v2, Br₂ collision partner data

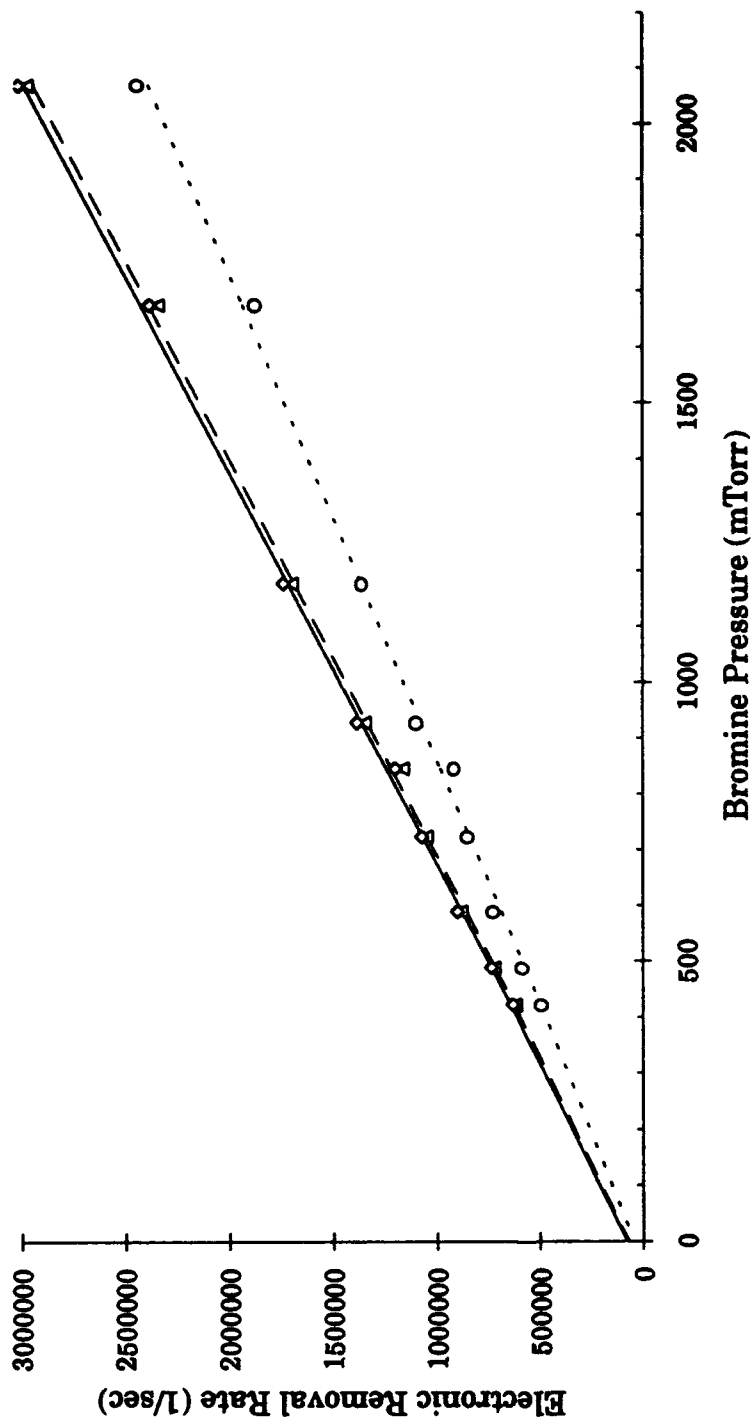


Figure 31. Stern-Volmer electronic removal plots for five level (data (o), fit (---)), seven level (data (Δ), fit (—)) and Montroll-Shuler (data (◊), fit (—)) models for p3v2, Br₂ collision partner data

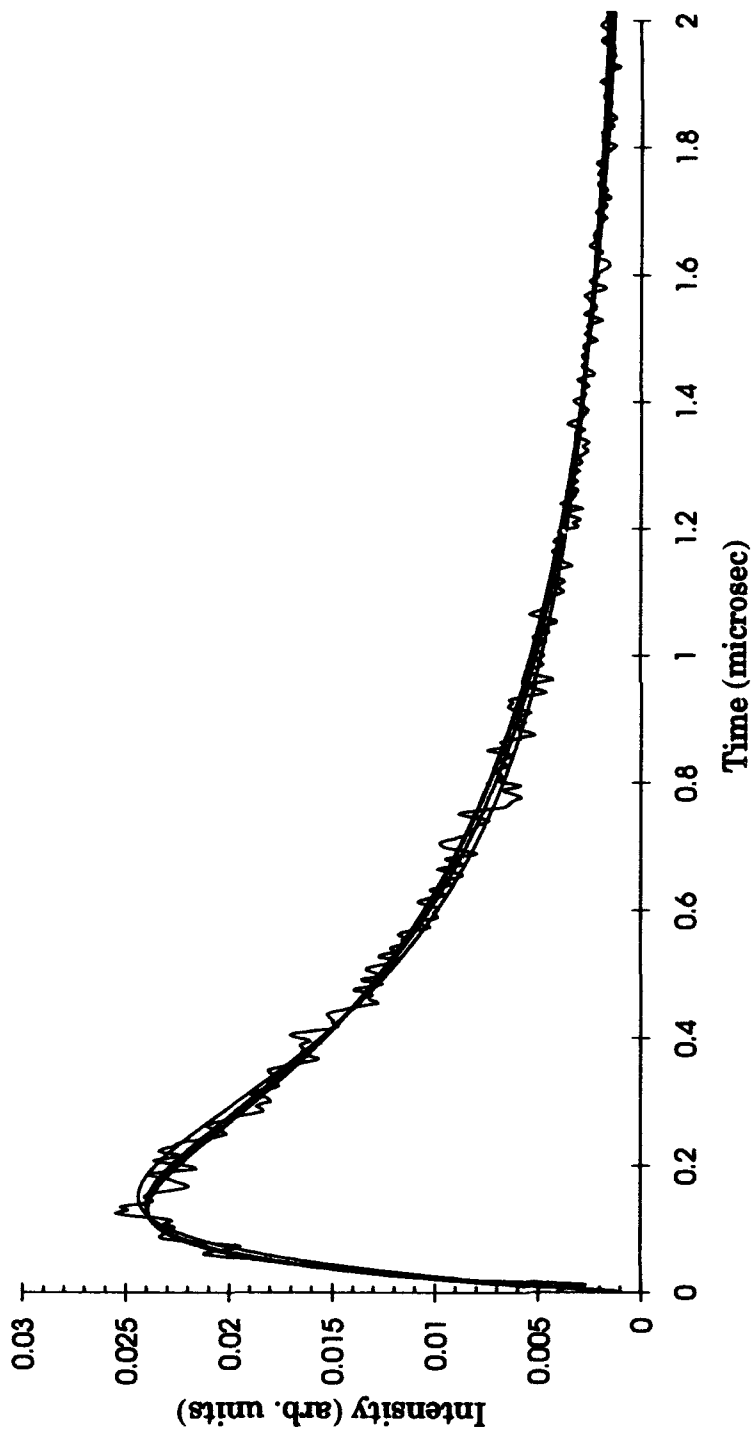


Figure 32. Montroll-Shuler, seven level, six level, five level, and four level model fits to p3v2 data with 1.7 Torr argon

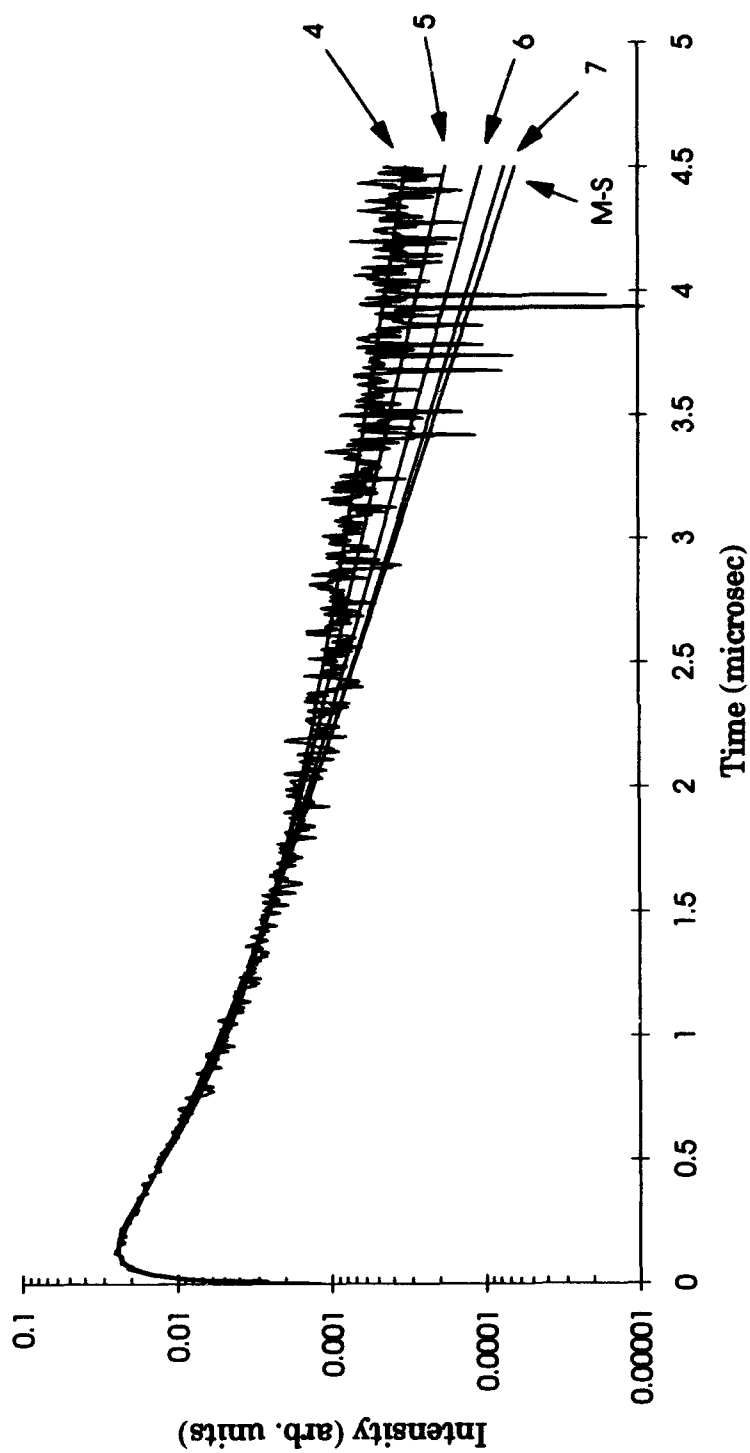


Figure 33. Montroll-Shuler (1), seven level (2), six level (3), five level (4), and four level (5) model fits to p3v2 data with 1.7 Torr argon

data, the Montroll-Shuler fits reflect a higher effective electronic removal rate than is actually present in the data. On the other hand, the n-level models effectively allow for a state-dependent removal rate in the highest non-predissociative vibrational level (i.e., transfer to but not from predissociative levels). This allows the fitting routine to compensate for slower decay at long times for n-level models by trading $V \rightarrow T$ transfer and electronic removal (Γ_v and Γ_0 , respectively). The fact that the seven level system fit in Figure 33 is virtually identical to the Montroll-Shuler fit indicates that very little population is transferred up to $v' \geq 7$ in the Montroll-Shuler model. However, as n is decreased, it is clear from Figure 32 and Figure 33 that the tradeoff between Γ_v and Γ_0 is occurring.

Stern-Volmer plots for the fits to these data are shown in Figures 34 and 35. $V \rightarrow T$ transfer and electronic removal rate coefficients obtained from the Stern-Volmer plots are given in Table 10. $V \rightarrow T$ transfer rate coefficients obtained from slopes of the Stern-Volmer plot for the five level, six level, seven level and Montroll-Shuler models agree favorably with one another for the argon collision partner. The $k_v(1,0)$ values obtained from Figure 34 are all within $\sim 10\%$ of the Montroll-Shuler value. The four level system provided the best fit parameter for each data set, however, the $k_v(1,0)$ value for the four level system was $\sim 25\%$ lower than the Montroll-Shuler value. Electronic quenching rates from Figure 35 did not agree as well. Quenching rate coefficients from the truncated systems were all smaller than the Montroll-Shuler value, with the four level system k_q value being only 20% of the Montroll-Shuler value. The considerable difference in rate coefficient values between the four level system and the Montroll-Shuler model is certainly reasonable since the four level system is the least physically believable of the

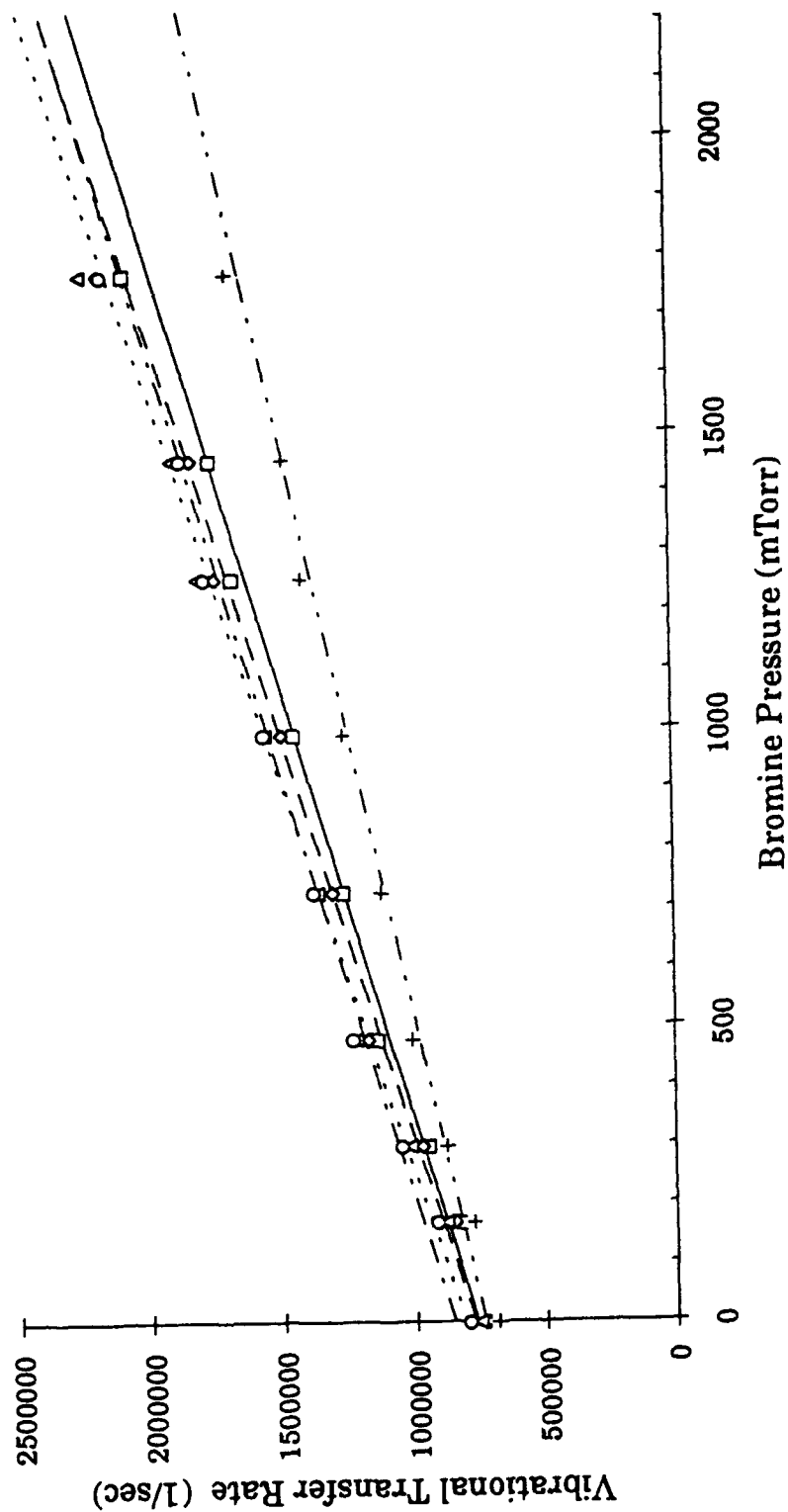


Figure 34. Stern-Volmer vibrational transfer plots for four level (+), five level (o), six level (◊), seven level (Δ) and Montroll-Shuler (◻) models for p3v2, argon collision partner data

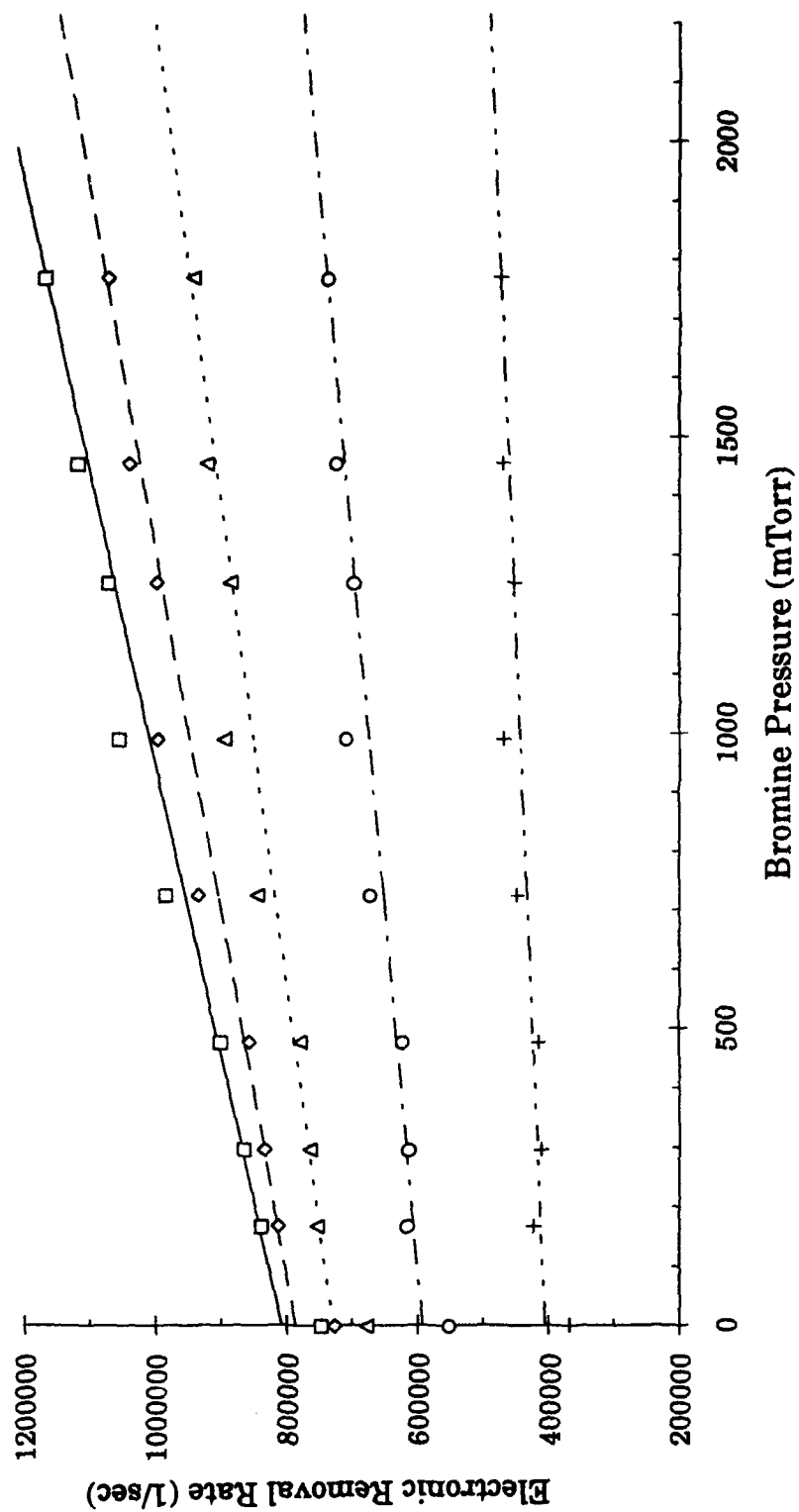


Figure 35. Stern-Volmer electronic removal plots for four level (+), five level (o), six level (◊), seven level (Δ) and Montroll-Shuler (◻) models for p3v2, argon collision partner data

Table 10

Fundamental vibrational transfer rate coefficients and electronic quenching rate coefficients ($10^{-11} \text{ cm}^3/\text{molec}\cdot\text{sec}$) for $\text{Br}_2(\text{B})$ from n-level systems

Collision Partner	pump/view levels	Model	$k_v(1,0)$	k_q
Br_2	3 / 2	5 level	3.7	4.2
		7 level	3.3	5.2
		M-S	3.2	5.2
Ar	3 / 2	4 level	1.86	.13
		5 level	2.53	.31
		6 level	2.75	.46
		7 level	2.67	.60
		M-S	2.49	.75
Ar	2 / 3	5 level	3.58	.40
		M-S	3.68	1.02
Ar	2 / 1	5 level	2.42	.045
		7 level	2.37	.15
		M-S	2.28	.19

n-level systems. This is because the four level system assumes that all transfer to $v' = 4$ is lost by predissociation. However, Tellinghuisen (10) showed that predissociation in the $\text{Br}_2(\text{B})$ state is strongest in $v' = 5$ and significantly smaller in $v' = 4$.

The five level model was also fit to p2v1 and p2v3 data while the seven level model was fit to the p2v1 data with argon as collision partner. As in the p3v2 data described above, the fundamental $V \rightarrow T$ transfer rate coefficient

values from the truncated models were within ~10–15% of the values obtained using the Montroll-Shuler model. The quenching rate coefficients from the five level system were about half of the Montroll-Shuler values while the seven level system quenching rate coefficients were about ~80% of the Montroll-Shuler values for both sets of data. Again, the visual quality of the non-linear least squares fits was better for the five level system than for the Montroll-Shuler model, especially at long times (i.e., after 2 μ sec).

The improved fits with the truncated vibrational manifold models over the infinite vibrational manifold Montroll-Shuler model support the idea that predissociation is a major contributor to the observed deviations in the rare gas collision partner studies. However, as was discussed in chapter II, the fact that emissions have been observed from many $\text{Br}_2(\text{B})$ vibrational levels above $v' = 3$ and rotationally dependent predissociation rate coefficients have been experimentally determined for many of these states (10) implies that a simple truncated vibrational manifold is not physically reasonable. Therefore, the most reasonable physical explanation for the observed deviations from Montroll-Shuler is that the electronic removal rates (i.e., quenching, radiation and/or predissociation) are not independent of vibrational level. In the case of $\text{Br}_2(\text{B})$, it is quite possible that the pure electronic quenching rates and radiative lifetimes are state independent while the probability for either spontaneous or collision induced predissociation is both rotational and vibrational state dependent. Unfortunately, experimental verification of this hypothesis is practically impossible. Vibrational state dependent electronic removal rates can significantly affect the energy transfer rate matrix. Analytic solutions to the master rate equation, such as Montroll-Shuler or the n-level systems described here, cannot be obtained, even if the various

state dependent rates and lifetimes are known. If state dependent rates and lifetimes are not known, any number of non-unique relationships between the electronic removal rates can be found that fit the data as well or better than any of the models considered here. One example of a non-unique fit to experimental data is shown in Figure 36 where a seven level system with an arbitrary, but somewhat reasonable electronic removal rate dependence, is virtually identical to the fit obtained with the four level model described above. For the seven level system in Figure 36, the electronic removal rates for the different vibrational levels, $\Gamma_0(v')$ were scaled as follows:

$$\Gamma_0(0) = \Gamma_0(1) = \Gamma_0(2) = 0.75 \Gamma_0(3) = 0.05 \Gamma_0(4) = 0.005 \Gamma_0(5) = 0.005 \Gamma_0(6)$$

In any case, the general agreement in $k_v(1,0)$ values obtained from the five, six and seven level models and the values from Montroll-Shuler in Table 10 strongly support the $V \rightarrow T$ transfer scaling used in all of the models. The wide variations in the electronic quenching rates reported in Table 10 can be attributed to the fact that the reported values are actually averages of electronic removal rates that have strong rovibrational level dependencies, at least for $v' \geq 4$. Because of this averaging effect, it is unreasonable to attach any additional physical significance to the k_q values reported in Table 10.

In summary, the n-level models provided a reasonable contrast to the infinite manifold Montroll-Shuler model. For practical purposes, the $k_v(1,0)$ values given in Table 9 obtained with the Montroll-Shuler fits adequately describe $V \rightarrow T$ transfer in the $\text{Br}_2(\text{B})$ state. The error bounds reported in Table 9 are probably a little optimistic and should practically be around 20% for $k_v(1,0)$ fundamental rate coefficient. The considerable variation in the electronic quenching rate coefficients obtained with the various models

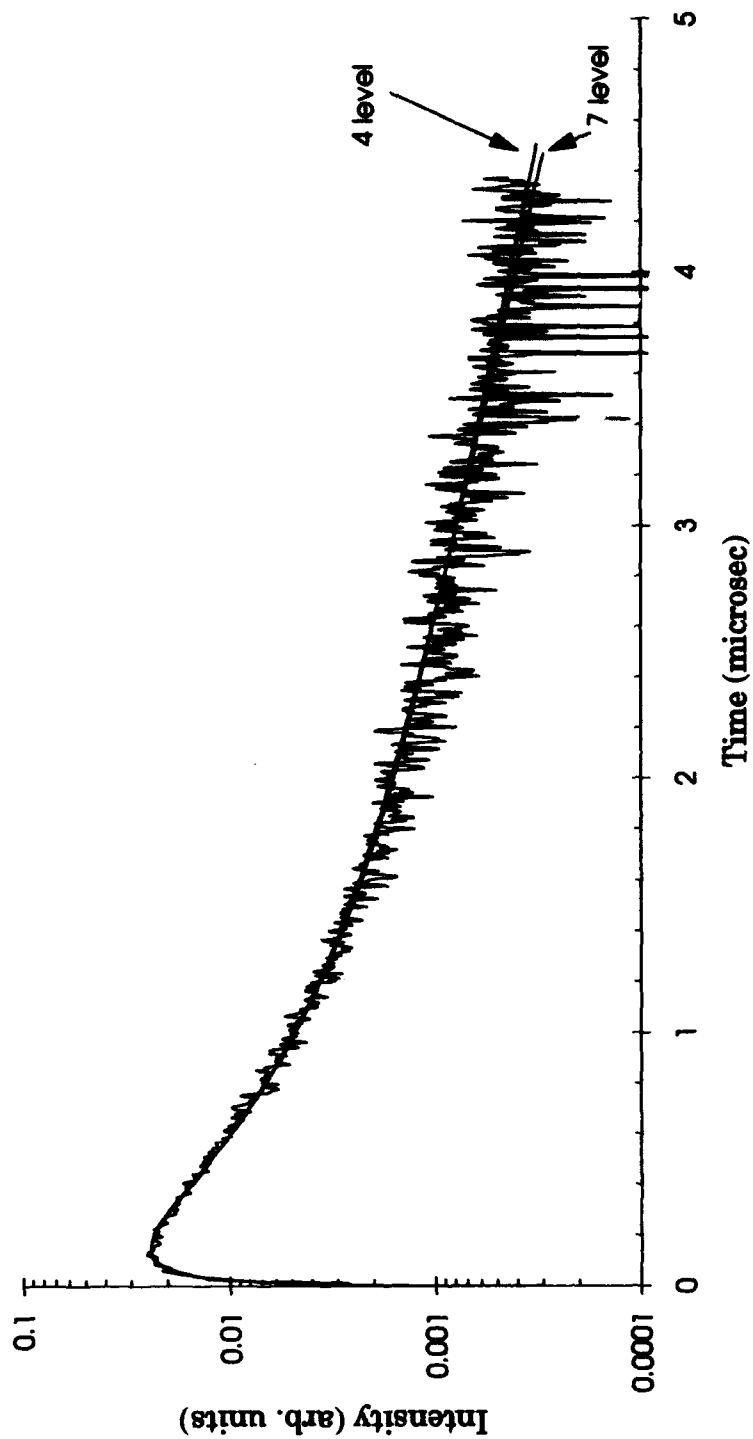


Figure 36. Four level system fit and seven level system with state dependent electronic removal rates fit to p3v2 data in argon

makes the k_q values in Table 9 quite suspect. Since it is probable that electronic removal rates in the $\text{Br}_2(\text{B})$ state are vibrational state dependent, the averaged k_q values obtained with the Montroll-Shuler model should be within 50% for $v' \leq 3$.

5.3 $V \rightarrow T$ Scaling Theories

The Schwartz, Slawsky and Herzfeld (SSH) theory (38) described in Appendix B predicts that the vibrational transfer probability for collisions with monatomic partners depends upon the reduced mass of the collision pair, μ , the vibrational energy spacing of the diatomic molecule, ω/kT , and the interaction length, L , between the two collision partners. The full SSH functional form from Appendix B as given by Yardley (49) is

$$P_{10} = M \cdot \left(\frac{\Theta'}{\Theta} \right) \left(\frac{\Theta'}{T} \right)^{1/6} \exp \left[-\frac{3}{2} (\Theta'/T)^{1/3} + (\Theta/2T) + (\epsilon/k_B T) \right] \quad (\text{B.7})$$

where

P_{10} = probability of $V \rightarrow T$ transfer from vibrational state 1 to state 0

$$M = \sqrt{\frac{2\pi}{3}} \frac{2A^2BC}{(B+C)(A+B)^2 \cdot \mu}$$

A = mass of collision partner

B, C = masses of the diatomic molecule

μ = reduced mass of collision pair

$$\Theta' = 4\pi^2 L^2 \omega^2 \mu / k_B$$

$$\Theta = \hbar \omega / k_B$$

$\hbar \omega$ = vibrational energy

ϵ = potential well depth of collision partners

L = interaction length

Typically, initial comparisons are made with SSH by assuming that the exponential terms in Eq (B.7) dominate (this will be discussed further later on) and can be written as

$$\ln(P_{10}) \propto \ln(\sigma_v(1,0)/\sigma_g) = A - B \mu^{1/3} \omega^{2/3} \quad (39)$$

where

$\sigma_v(1,0)/\sigma_g$ = ratio of fundamental V→T transfer cross section to the gas kinetic cross section

A, B = constants independent of reduced mass or energy spacing

In Table 9, the ratio $\sigma_v(1,0)/\sigma_g$ is tabulated for the rare gas collision partners from the experiments in this study. The gas kinetic cross-sections were calculated using atomic radii values from Hirschfelder, et al. (20) and are discussed in Appendix B. Fundamental vibrational transfer probabilities have been previously reported for BrF, BrCl, and IF (30, 33, 47). The V→T transfer probabilities for Br₂(B) along with the interhalogens IF(B), BrF(B) and BrCl(B) have been plotted in Figure 37 as a function of the cube root of the collision pair reduced mass. Eq (39) predicts a linear relationship with a negative slope for the transfer probabilities in Figure 37. Note that the IF(B) and BrF(B) data exhibit the reduced mass dependence predicted by Eq (39). However, the BrCl data shows no clear trend with reduced mass while the Br₂ data exhibits a linear dependence with a positive slope.

The observation that both BrCl and Br₂ deviate from the reduced mass scaling of Eq (39) (the simplified SSH scaling) is certainly reasonable. As is noted in Appendix B, the SSH theory was developed for molecules with large vibrational energy spacings ($\omega_e/kT > 1$). This condition is met reasonably well for both IF and BrF ($\omega_e/kT = 2$ and $\omega_e/kT = 1.7$, respectively). However,

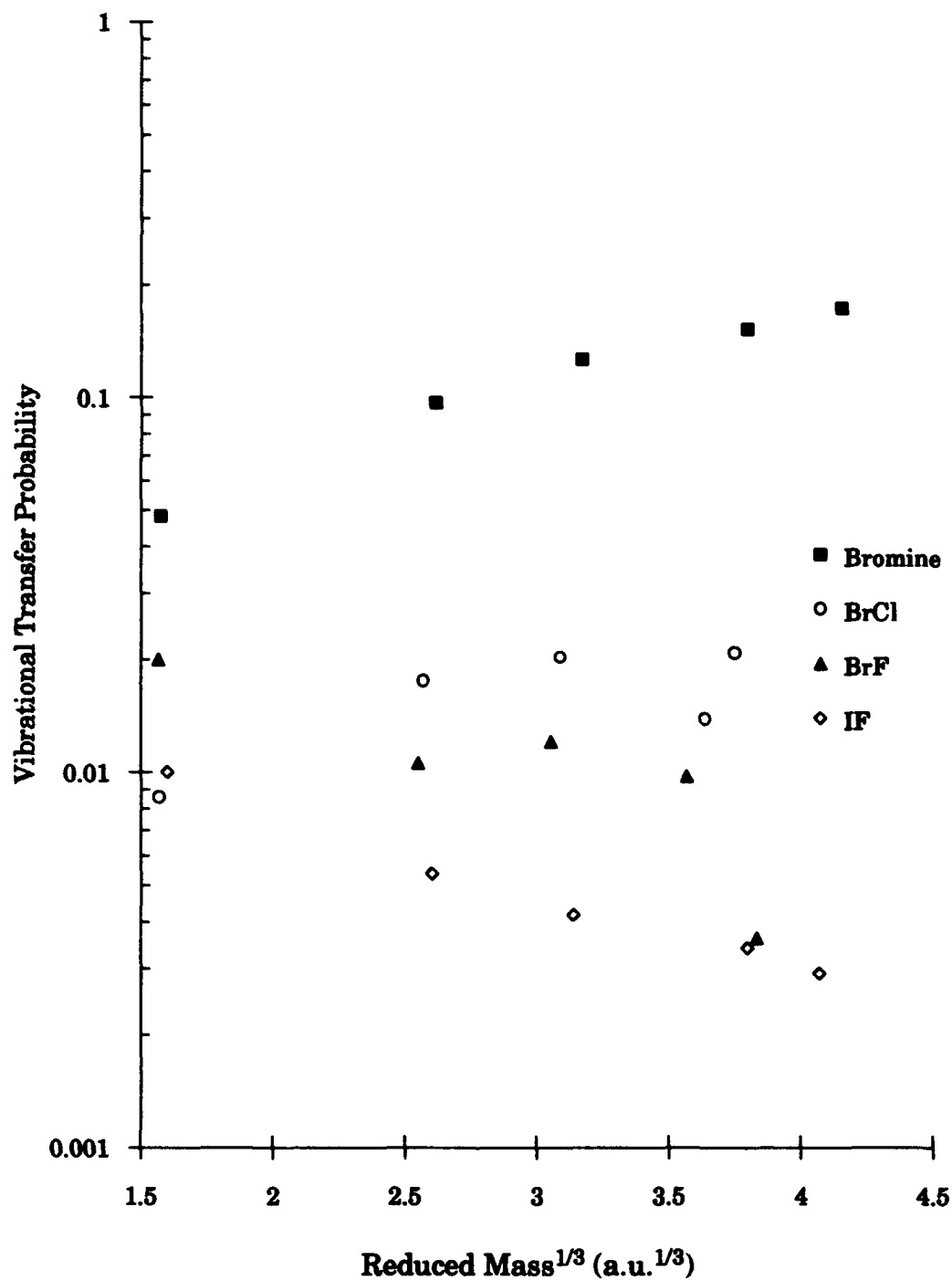


Figure 37. Vibrational transfer probabilities ($\Delta v = -1$) for Br_2 , BrCl (33), BrF (30) and IF (47) with rare gas collision partners as a function of the cube root of the collision pair reduced mass

the condition is only marginally satisfied for BrCl ($\omega_e/kT = 1.1$) and Br₂ (where $\omega_e/kT \approx 1$ for the heated cell used in this study). In addition, the experimental $k_v(1,0)$ values obtained for V→T transfer in Br₂ with rare gas collision partners are quite large (typically $\approx 0.1 \times$ gas kinetic rates). The small vibrational spacings and rapid transfer rates bring into question the validity of a perturbational approach. It is not too surprising, therefore, that V→T transfer in both BrCl and Br₂ deviate from the simplified form of the SSH theory in Eq (39). Nevertheless, it was still of interest to further investigate the SSH theory for Br₂ and the interhalogens to determine the significance of the pre-exponential terms in Eq (B.7). Since it was reasonable to expect that the interaction length, L , will vary, depending upon both the diatomic molecule and collision partner being considered, an interesting exercise was to calculate L for the various diatomic species and collision partners using the complete SSH equation form given by Eq (B.7) (see Appendix B). The only unknown parameter in Eq (B.7) (other than L) was the potential well depth, ϵ . According to Yardley (49), accurate values for ϵ are difficult to obtain. In general, however, ϵ is much smaller than $k_B T$ so that the exponential term containing ϵ is typically on the order of unity. Using the approximation that $\exp(\epsilon/k_B T) \approx 1$, values for the interaction length, L , were calculated for all combinations of diatomic and collision partner species. The results are plotted in Figure 38 as a function of collision pair reduced mass. Two observations can be made from this set of data. First, the values obtained for L are reasonable for all cases. According to Yardley (49), interaction lengths are typically on the order of a few tenths of an Å, which is the case here. Second, for each of the diatomic molecules considered, the calculated interaction length decreases as the mass of the

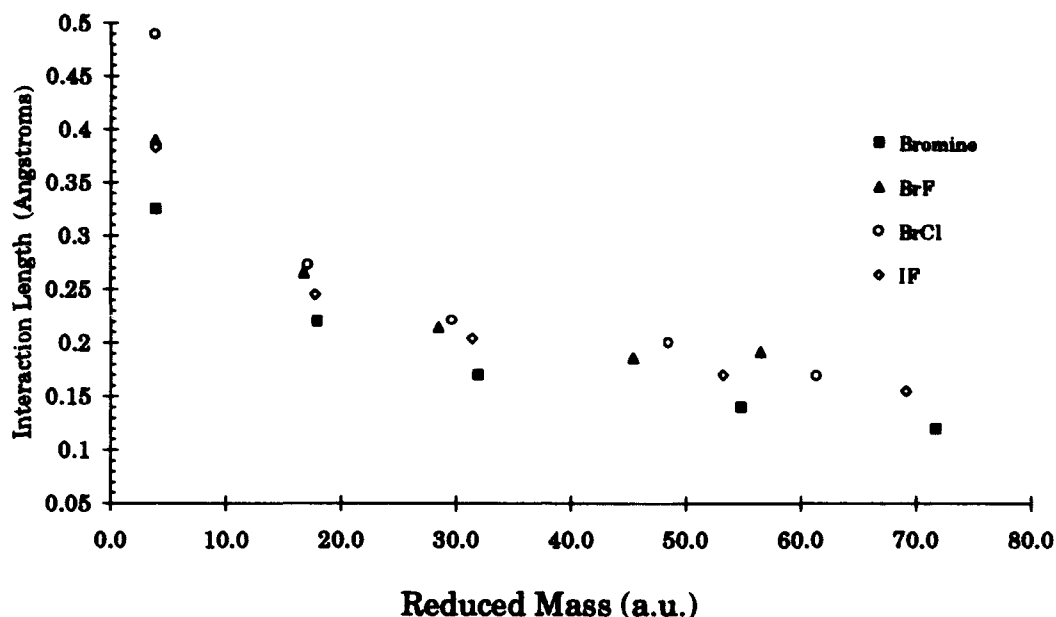


Figure 38. Interaction length as a function of collision pair reduced mass for Br_2 , IF, BrF and BrCl with rare gas collision partners

rare gas collision partner increases. While the validity of the SSH perturbational approach is questionable, at best, for the diatomic halogens and interhalogens, the consistent reduced mass trends and reasonable magnitudes of the calculated interaction lengths imply that the SSH theory may still be applicable for this class of molecule. It is also clear that the failure of the simplified SSH form in Eq (39) to adequately account for the reduced mass trends in the experimental data in Figure 37 indicates that the pre-exponential factors in the full SSH equation are important and should not be discarded arbitrarily.

Another apparent trend from Figure 37, is that, for a given rare gas collision partner, the probability of vibrational transfer increases as the vibrational energy spacing of the diatomic molecule decreases. A plot of the

fundamental transfer probabilities for IF(B), BrF(B), BrCl(B) and Br₂(B) as a function of the diatomic molecule vibrational energy spacing, ω , for collisions with argon is shown in Figure 39. The linear trend and negative slope are both consistent with the scaling in the simplified SSH form of Eq (39).

A final note regarding SSH scaling should be made concerning the possibility of V→V transfer occurring in the Br₂ self-transfer experiments. It can be seen in Appendix A that the vibrational energy spacings in the ground state Br₂ are very nearly twice the value of the vibrational spacings in the Br₂(B) state. Because of this energy difference, a single-quantum vibrational level change in the ground state would require a change of two vibrational quantum levels in the B state. No conclusive evidence for multi-quantum transfer was observed in the Br₂ collision partner data. The probability for V→T transfer in the Br₂ collision partner experiments also showed no significant deviation from the trends in the rare gases. This can be seen in Figure 40 where the self-transfer probability has been included along with the rare gas values. It is probable that while some V→V transfer may occur, its effects are not significant compared to purely V→T transfer.

5.4 Uniqueness of Solution

The process of extracting uniquely defined state-to-state V→T transition probabilities from experimentally observed population distributions is not necessarily a straightforward task. Carrington has shown that the precision needed in the experimental data in order to obtain uniquely defined transition probabilities is often much greater than the precision required in the transition probabilities themselves (4). This is because the temporal population distributions generated by a given set of

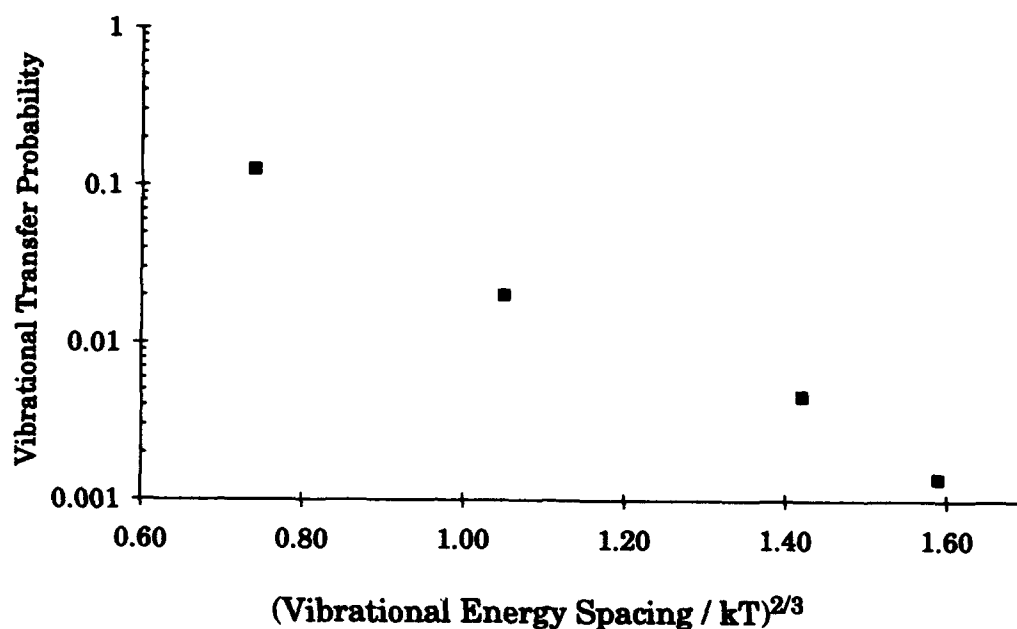


Figure 39. Vibrational transfer probabilities ($\Delta v = -1$) for Br_2 , BrCl , BrF and IF for collisions with argon as a function of the $2/3$ power of the diatomic molecule vibrational energy spacing

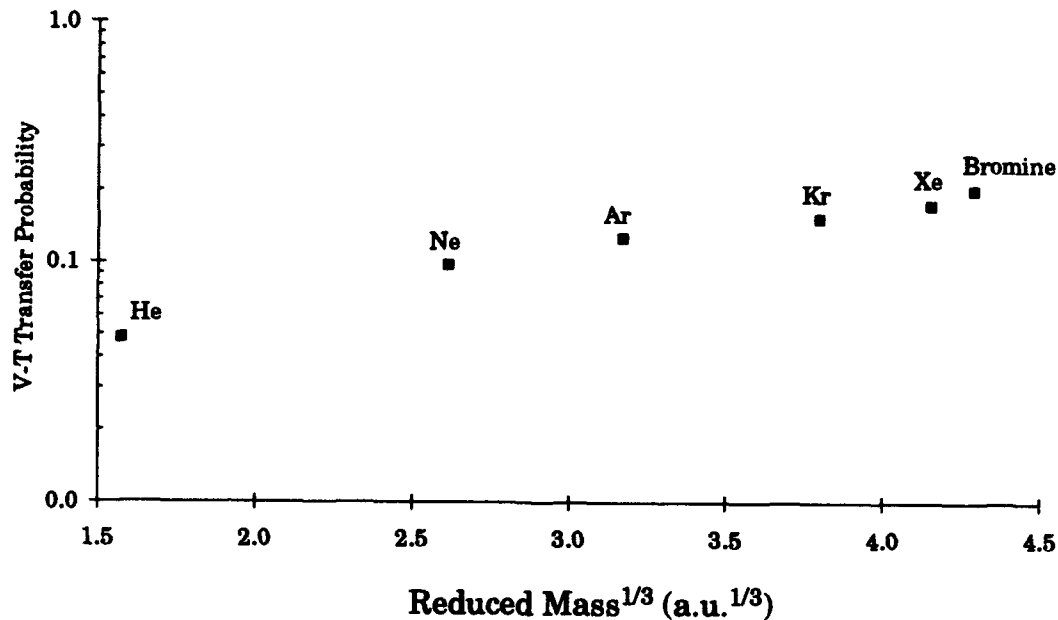


Figure 40. Vibrational transfer probabilities ($\Delta v = -1$) for Br_2 for self-transfer and rare gas collision partners as a function of the cube root of the collision pair reduced mass

themselves (4). This is because the temporal population distributions generated by a given set of transition probabilities may be quite insensitive to rather significant changes in the individual transition probabilities themselves. In other words, there may be several different sets of transition probabilities that generate virtually identical population distributions. From an experimental data analysis standpoint, this is equivalent to having several different functional forms that fit a given set of experimental data equally well. Such was the case in the current $V \rightarrow T$ transfer study in the $\text{Br}_2(\text{B})$ state. The Montroll-Shuler fits and the n -level system fits described earlier are certainly examples of the difficulty in obtaining unique transition probabilities. However, the differences between the $k_v(1,0)$ values obtained from these various models were within reasonably expected error limits for this type of experimentally determined rate coefficient. Additionally, the n -level systems each used the same Landau-Teller $V \rightarrow T$ scaling and state-independent electronic removal as the Montroll-Shuler model so a certain amount of agreement in the rate coefficients obtained from the models is expected. However, for the sake of completeness, the simple two exponent (one rising and one decaying) functional form given in Eq (32) was also fit the $V \rightarrow T$ transfer data with Br_2 collision partners. The following two sections discuss the analysis and results obtained from this double exponential fitting effort and serve to further exemplify the difficulty in uniquely defining state-to-state $V \rightarrow T$ transfer rate coefficients.

5.4.1 Double Exponential Fits

The double exponential functional form of Eq (32) was implemented as a user-defined function in TableCurve and fit to all of the Br_2 collision partner

data obtained in the current study. Typical examples of the non-linear, least-squares fits to experimental data are shown in Figures 41 and 42.

TableCurve extracted two inverse lifetime values corresponding to the two exponential decay terms from each data trace. The inverse lifetimes were plotted and analyzed using the Stern-Volmer technique discussed earlier. Stern-Volmer plots for the p3v2 data are shown in Figure 43. Rate coefficients obtained from the slopes of the Stern-Volmer plots are reported in Table 11. The k_{fast} coefficient corresponds to the early time, rising exponential term while the k_{slow} rate coefficient corresponds to the later time, decaying exponential term.

5.4.2 Analysis of the Double Exponential Fits

The high quality of the fits to the data was unexpected because both of the mechanisms discussed in chapter II that resulted in the functional form of Eq (32) were considered to be unacceptable models for V→T transfer in the Br₂(B) state. Nevertheless, it was of interest to determine if the V→T transfer rate coefficients or the electronic quenching rate coefficients ($k_v(1,0)$ and k_q , respectively) obtained from the Montroll-Shuler fits described earlier could be obtained from the fits to Eq (32). To accomplish this task, a physically reasonable explanation for the quality of the fits to Eq (32) was needed. If the assumptions used to obtain Eq (32) (see chapter II, section 3.3.3) were appropriate and electronic removal rates were equal for all v' levels, then the difference in the two total removal rates out of levels p and p_0 in Eq (32) would be equivalent to the difference in vibrational removal rates. Assuming Landau-Teller V→T transfer scaling, the difference in removal rates can be related to the fundamental V→T transfer rate coefficient by the

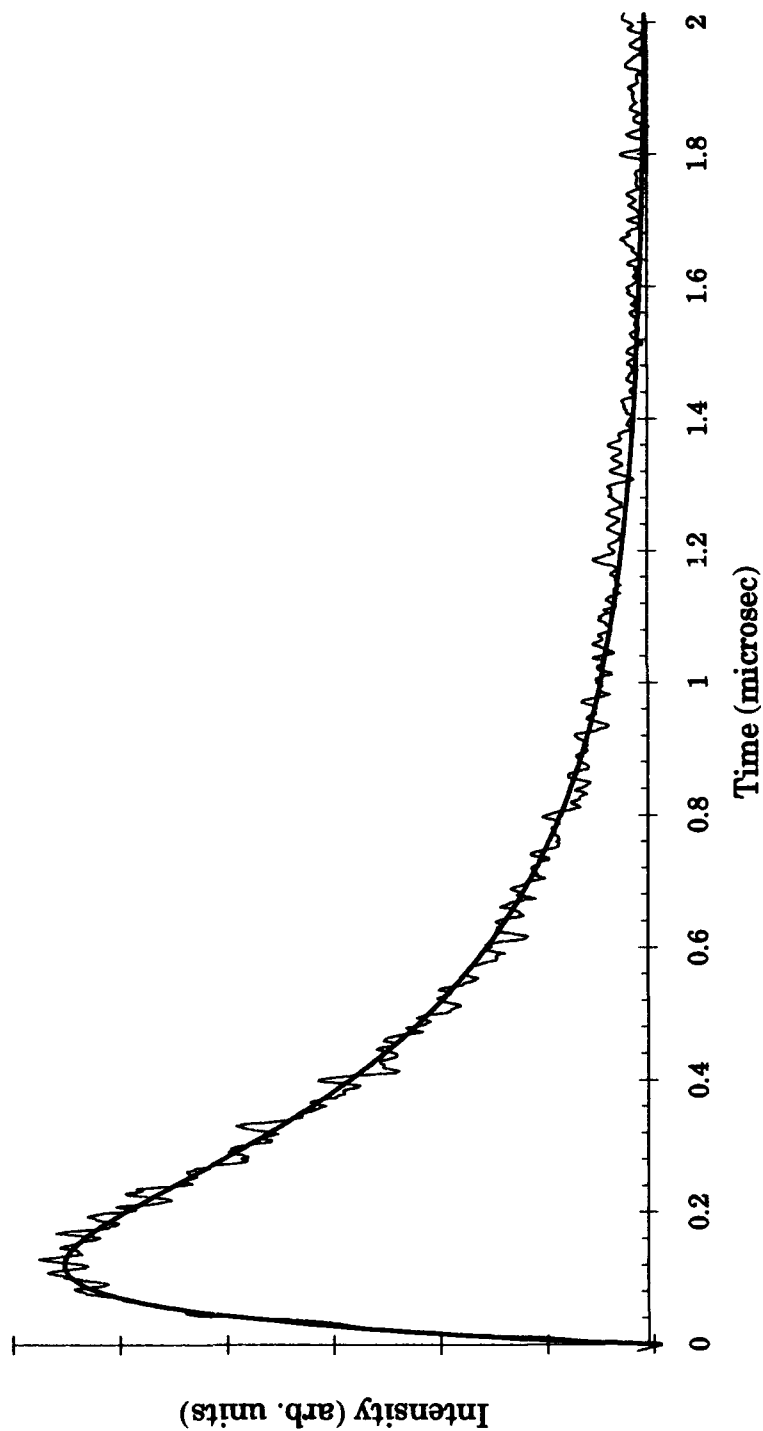


Figure 41. Double exponential fit to emissions from the (2-11) band after excitation of $v' = 3$ with a Br_2 pressure of 1.68 Torr

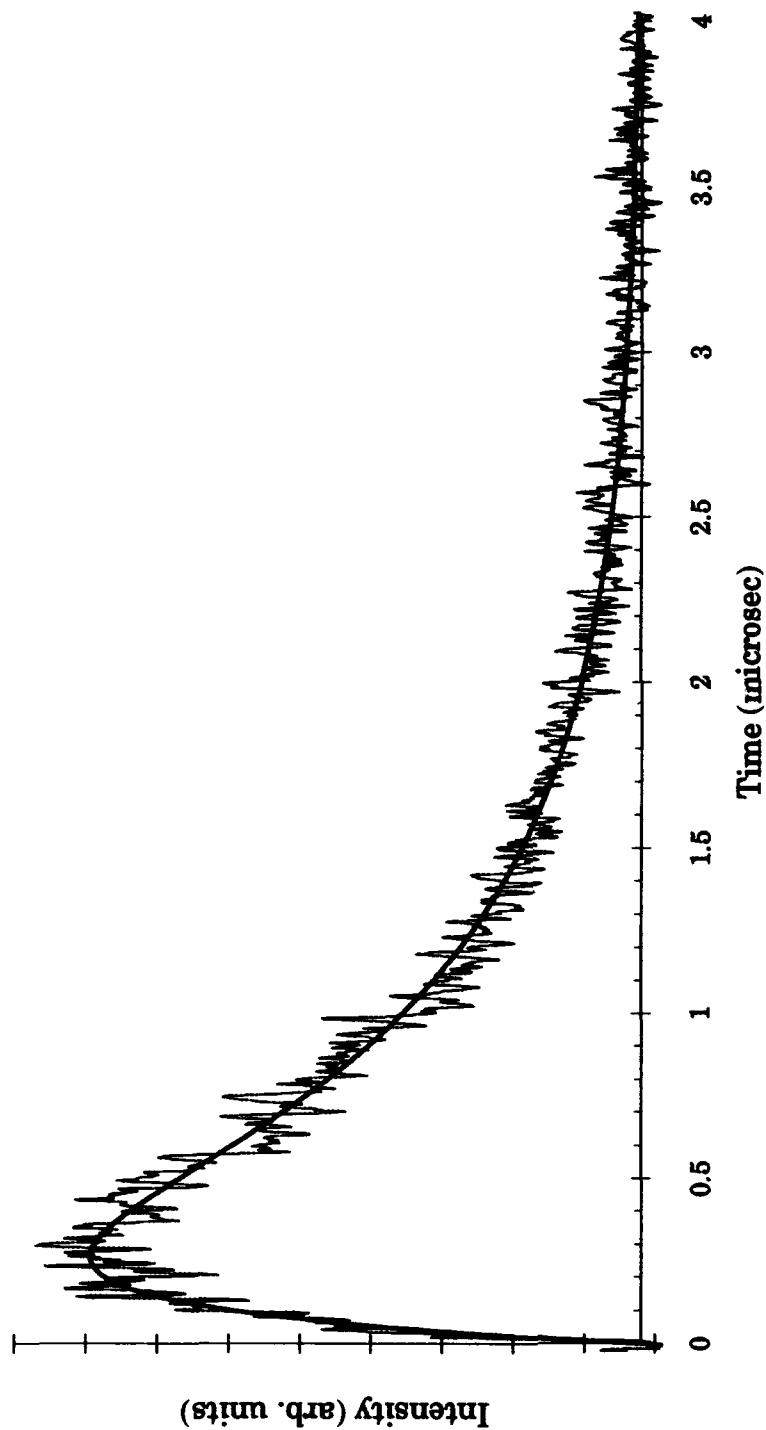


Figure 42. Double exponential fit to the emissions from the (2-11) band after excitation of $v' = 3$ with a Br_2 pressure of 724 mTorr

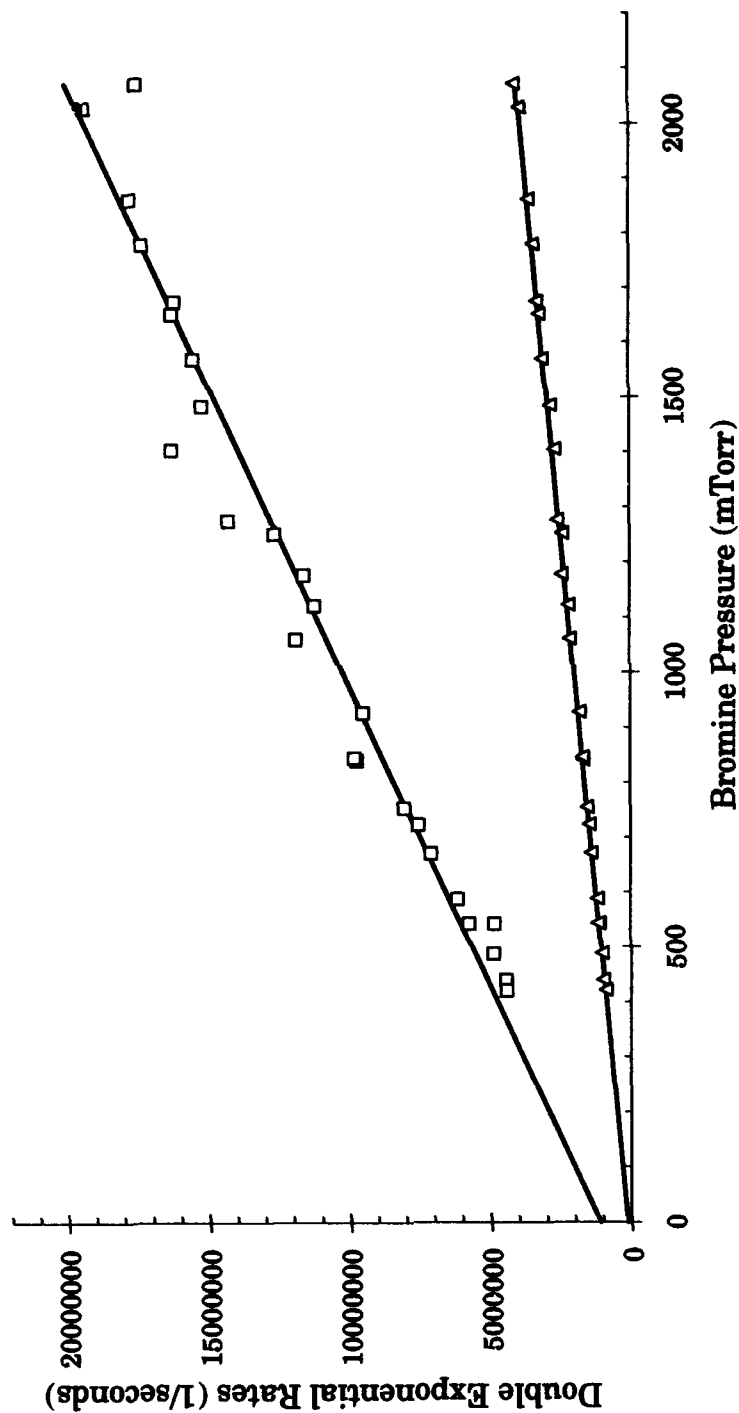


Figure 43. Stern-Volmer plot for the double exponential fits to the pump $v' = 3$, view $v' = 2$ data with $\text{Br}_2(\text{X})$ as buffer specie. Fast rate $()$ is $3.4 (\pm 0.1) \times 10^{-10}$ and slow rate (Δ) is $6.9 (\pm 0.1) \times 10^{-11} \text{ cm}^3/\text{molec}\cdot\text{sec}$

Table 11

Rate coefficients from Stern-Volmer analysis of double exponential fits to collisionally populated $\text{Br}_2(\text{B})$ satellite states induced by collisions with $\text{Br}_2(\text{X})$ ($10^{-11}\text{cm}^3/\text{molec}\cdot\text{sec}$)

v' pump/view	k_{fast}	k_{slow}
2 / 3	28 ± 2	5.7 ± 0.2
3 / 2	34 ± 1	6.9 ± 0.1
2 / 1	28 ± 1	2.4 ± 0.1

expression

$$k_{\text{TR}}(p_0) - k_{\text{TR}}(p) = N \times k_v(1,0) \quad (40)$$

where N is a proportionality constant which can be determined from the applicable scaling laws. In the case of pump $v' = 3$ and view $v' = 2$ data, evoking detailed balance and solving for N we get

$$N = \{4 \exp(-\Delta E_{4-3}/kT) + 3\} - \{3 \exp(-\Delta E_{3-2}/kT) + 2\} \approx 15 \quad (41)$$

From Table 11, the difference between the fast and slow rate coefficients for the p3v2 transition is approximately $27 \times 10^{-11} \text{cm}^3/\text{molec}\cdot\text{sec}$ which is about $7.5 \times k_v(1,0)$. Clearly, the assumptions used to arrive at Eq (32) are inappropriate and another explanation for the fit quality of the double exponential function is needed.

One reasonable explanation that relates directly to the uniqueness issue can be developed using the five-level truncated vibrational manifold model discussed earlier in this chapter and in Appendix B. The solution to the five-level model for the p3v2 case which describes the temporal evolution of the population in $v' = 2$ is given by

$$\begin{aligned} x_2(t) = & -0.23 \exp\{-(9.2\Gamma_v + \Gamma_o)t\} - 0.28 \exp\{-(5.1\Gamma_v + \Gamma_o)t\} \\ & + 0.09 \exp\{-(2.5\Gamma_v + \Gamma_o)t\} + 0.34 \exp\{-(0.93\Gamma_v + \Gamma_o)t\} \\ & + 0.08 \exp\{-(0.04\Gamma_v + \Gamma_o)t\} \end{aligned} \quad (42)$$

where Γ_v and Γ_o are defined as they were in chapter II as

$$\begin{aligned} \Gamma_v &= k_v(1,0)[M] \\ \Gamma_o &= k_q[M] + 1/\tau_{\text{rad}} \end{aligned}$$

Using the Br_2 collision partner rate coefficients and radiative lifetimes given in Table 6, it is clear that Γ_o and Γ_v are on the same order of magnitude ($\sim 10^6 \text{ sec}^{-1}$). Therefore, the final exponential term in Eq (42) can be approximated by only the electronic removal term, $\exp(-\Gamma_o t)$. This term is probably the dominant feature in the experimental data at long observation times. This explains why the k_{slow} rate coefficients in Table 11 are similar to the quenching rates reported in Table 6. The k_{fast} rate coefficients cannot be attributed directly to any one of the four remaining exponential terms from the five level system in Eq (42). More likely, because of the short rise times and relatively small number of data points before the peaks in the experimental data, the k_{fast} rate coefficients are a combination of the four faster eigenvalues in Eq (42). Both the Montroll-Shuler model and the

double exponential model were fit to population profiles generated by the five-level system of Eq (42) and provided acceptable fits. Rate coefficients for both models obtained using Stern-Volmer analysis were consistent with the present discussion. It was concluded, therefore, that the fits of the double exponential form of Eq (32) to the experimental data can be explained qualitatively as just described. However they provide little quantitative information concerning the fundamental energy transfer mechanisms in the $\text{Br}_2(\text{B})$ state.

5.5 Comparisons with Previous Studies

No other spectrally resolved, temporally resolved LIF studies investigating state-to-state vibrational energy transfer in the $\text{Br}_2(\text{B})$ state have been reported previously. Clyne, Heaven and Davis examined vibrational transfer in $\text{Br}_2(\text{B})$ from $v' = 11$ to $v' = 10$ with N_2 as collision partner (11) using CW LIF excitation. Their reported rate of $k_v(11,10) = 2.5 (\pm 1.0) \times 10^{-11} \text{ cm}^3/\text{molec}\cdot\text{sec}$ cannot be directly compared to the current results for several reasons. No diatomic buffer molecules except $\text{Br}_2(\text{X})$ were studied in the present work. Additionally, all of the present studies were conducted in the non-predissociative levels of the $\text{Br}_2(\text{B})$ vibrational manifold while the Clyne and coworkers vibrational levels were severely affected by both collision-induced and spontaneous predissociation. Nevertheless, by comparing the relative orders of magnitude in Clyne's $k_v(11,10)$ and the current $k_v(1,0)$ values (i.e., $k_v(11,10) \neq 11 \times k_v(1,0) = 39.6 \times 10^{-11}$), it is clear that the Landau-Teller scaling for state-to-state $\text{V} \rightarrow \text{T}$ transfer rate coefficients needed for the Montroll-Shuler model is not applicable for v' levels very far above the onset of predissociation ($4 \leq v' \leq 5$).

Significantly more information is available on electronic quenching for comparison with the values reported here. Clyne, Heaven and Martinez used temporally resolved total fluorescence emissions from $\text{Br}_2(\text{B})$ $v' = 2$ in pulsed LIF experiments to study electronic quenching with Br_2 , N_2 and Ar (9). Their value for Br_2 self-quenching of $k_q = 5.8 (\pm 0.3) \times 10^{-11} \text{ cm}^3/\text{molec}\cdot\text{sec}$ is slightly higher than the value obtained here of $k_q = 5.0 (\pm 0.2) \times 10^{-11} \text{ cm}^3/\text{molec}\cdot\text{sec}$ for $v' = 2$. Considering the difference in the methods used to obtain the current values, we believe the agreement is certainly acceptable. The situation is not as straightforward for the case of argon. Clyne's value for electronic quenching by argon of $k_q = 1.7 (\pm 0.3) \times 10^{-11} \text{ cm}^3/\text{molec}\cdot\text{sec}$ is more than three times as large as the average value obtained from the Montroll-Shuler fits in the current work of $k_q = 5.0 (\pm 0.2) \times 10^{-12} \text{ cm}^3/\text{molec}\cdot\text{sec}$. The slow rate observed from the double decaying exponential fit was $1.9 (\pm 0.2) \times 10^{-11} \text{ cm}^3/\text{molec}\cdot\text{sec}$ which is in much better agreement with Clyne's value. The reason for the large discrepancy in the argon quenching rate is unclear at the present time.

Vibrational energy transfer in the predissociative vibrational levels of the $\text{Br}_2(\text{B})$ state has been shown to be an inefficient process when compared with total removal from the initially populated states (11). The current work indicates, however, that in the nonpredissociating vibrational levels, $V \rightarrow T$ transfer competes strongly with pure electronic quenching. In light of this, it was of interest to investigate whether vibrational transfer may have affected the electronic quenching rates reported by Clyne and coworkers (9) for $v' = 2$ obtained using total fluorescence techniques. Simulated total fluorescence data was generated in Mathematica using the Montroll-Shuler model over the Br_2 pressure range observed by Clyne (1-110 mTorr). For simplicity, only

emissions from $v'=1, 2$ and 3 after excitation of $v' = 2$ were included. Each vibrational level was assumed to be detected equally well. This last assumption is not too far off for the case of the 712 nm long-pass filtered RCA C31034 PMT used by Clyne. The radiative lifetime, quenching rate and vibrational transfer rate used were $5.0 \mu\text{sec}$, $5.0 \times 10^{-11} \text{cm}^3/\text{molec}\cdot\text{sec}$ and $3.6 \times 10^{-11} \text{cm}^3/\text{molec}\cdot\text{sec}$ from the current work. The simulated emission profiles were fit to a single exponential decay function from 2-20 μsec as in Clyne's work and analyzed with the Stern-Volmer technique to determine the apparent quenching rate of $6.5 \times 10^{-11} \text{cm}^3/\text{molec}\cdot\text{sec}$. Considering the simplicity of the model, this value is in fairly good agreement with Clyne's value for Br_2 self-quenching of $5.8 \pm 0.3 \times 10^{-11} \text{cm}^3/\text{molec}\cdot\text{sec}$. In light of this, it is reasonable to conclude that vibrational transfer may affect quenching rates for non-predissociated vibrational levels in $\text{Br}_2(\text{B})$ obtained from total fluorescence studies.

To test the validity of the vibrational transfer values obtained in this study, the measured total removal rate from $v' = 3$ can be compared with the sum of the vibrational transfer rates ($k_v(3,2)$ and $k_v(3,4)$) and electronic quenching rate (k_q) out of $v' = 3$. Values for $k_v(3,2)$ and k_q can be taken directly from Table 6, while detailed balance gives

$$\begin{aligned} k_v(3,4) &= 4 \cdot k_v(1,0) \cdot \exp(-\Delta G_{3 \rightarrow 4}/kT) \\ &= 8.0 \pm 0.8 \times 10^{-11} \text{cm}^3/\text{molec}\cdot\text{sec} \end{aligned}$$

Summing the removal processes from $v' = 3$ yields a total removal rate of $23.8 \pm 2.0 \times 10^{-11} \text{cm}^3/\text{molec}\cdot\text{sec}$ which is in good agreement with the experimental total removal rate of $25.8 \pm 1.0 \times 10^{-11} \text{cm}^3/\text{molec}\cdot\text{sec}$. A similar

calculation for total removal from $v' = 2$ yields a value of $18.3 \pm 0.5 \times 10^{-11}$ $\text{cm}^3/\text{molec}\cdot\text{sec}$ which does not agree as well with the experimentally determined rate of $25.5 \pm 0.2 \times 10^{-11}$ $\text{cm}^3/\text{molec}\cdot\text{sec}$ as the $v' = 3$ value. This difference is probably due to the method in which the total removal rates were obtained for the $v' = 2$ case. The reported value for $v' = 2$ was the faster of the two values from a two term exponential decay fit to the data. It is probable that the initial decay rate in the two exponential fit is subject to greater error than the long time rate because of the smaller number of data points that actually affect the fit.

V. Conclusions

Two areas of interest in Br₂ were examined in this dissertation research. The spectroscopy of the high vibrational levels in the ground state of ⁷⁹Br⁸¹Br was investigated using spectrally resolved emissions from pulsed laser induced fluorescence (LIF) experiments. Vibrational energy transfer and electronic quenching were studied simultaneously using spectrally resolved, temporally resolved pulsed LIF techniques.

1 Summary of Spectroscopy of High v'' Levels in Br₂(X)

The spectroscopy of the Br₂ ground state was investigated by observing spectrally resolved emissions from ⁷⁹Br⁸¹Br (B; $v' = 15-21$, $J' \leq 5$) which were selectively excited with a tunable pulsed dye laser. Bandhead progressions were observed to ground state vibrational levels ranging from $1 \leq v'' \leq 27$. The rotational distributions of the spectrally resolved emissions were virtually unrelaxed, however, a number of P-R doublets were observed from other Br₂ isotopes with overlapping excitation wavelengths. Over 100 bandheads for the ⁷⁹Br⁸¹Br isotopomer were identified and a set of ground state molecular constants were derived. The molecular constants from the current study were $\omega_e = 323.1 \pm 1.5 \text{ cm}^{-1}$, $\omega_e x_e = 1.02 \pm 0.1 \text{ cm}^{-1}$ and $\omega_e y_e = -3.77 \pm 0.2 \times 10^{-3} \text{ cm}^{-1}$ apply out to $v'' = 27$. Within the experimental error of this study, these values agree with those obtained by high resolution absorption spectroscopy for $v'' \leq 10$ reported by Barrow and coworkers (2). Energies and turning points for an RKR potential were also calculated for both sets of constants and compared. The relative agreement between the

calculated potentials indicates that the Barrow constants can also be considered accurate for $v'' \leq 27$.

2 Summary of Collisional Energy Transfer Studies in Br₂(B)

Vibrational energy transfer and electronic quenching within the non-predissociative vibrational levels in the Br₂(B) state were investigated for Br₂(X) and rare gas collision partners using spectrally resolved, temporally resolved LIF techniques. Vibrationally resolved emissions were observed from $v' = 1, 2$ and 3 after populations were excited by the laser in $v' = 2$ and 3 . The Montroll-Shuler model for vibrational transfer in harmonic oscillators was adapted to include an electronic quenching mechanism and used to extract rate coefficients for state-to-state vibrational energy transfer and electronic quenching simultaneously. A single fundamental vibrational transfer rate coefficient of $k_v(1,0) = 3.6 \pm 0.4 \times 10^{-11}$ cm³/molec-sec describes vibrational transfer rates for $0 \leq v' \leq 3$ for collisions with Br₂(X). V→T transfer rate coefficients for the rare gas collision partners were somewhat smaller, ranging from $k_v(1,0) = 2.5 \pm 0.3 \times 10^{-11}$ cm³/molec-sec for helium to $k_v(1,0) = 3.1 \pm 0.4 \times 10^{-11}$ cm³/molec-sec for xenon. Electronic quenching rates were much higher for Br₂(X) ($k_q = 3.7 \pm 1.2 \times 10^{-11}$ cm³/molec-sec) than for the rare gases (typically $8.0 \pm 1.2 \times 10^{-12}$ cm³/molec-sec for neon).

The observed fluorescence waveforms did display some deviation from the Montroll-Shuler model, especially at long times. The observed deviations varied with both pressure and collision partner, with the strongest deviations noted at higher pressures for light collision partners. Various n-level V→T transfer numerical models were used to determine that the observed

deviations were a result of vibrational state dependent electronic removal rates caused primarily by the rovibrationally dependent predissociation in $\text{Br}_2(\text{B})$ state vibrational levels $v' \geq 4$. No clear evidence of $\text{V} \rightarrow \text{V}$ transfer was observed in the Br_2 collision partner data. The probability for $\text{V} \rightarrow \text{T}$ transfer in $\text{Br}_2(\text{B})$ with the rare gas collision partners did not scale with reduced mass according to the simplified SSH theory, similar to previous observations in BrCl . However, calculations of the collision pair interaction length, L , using the full SSH equation for Br_2 , BrF , BrCl and IF provided reasonable values that decreased with increasing rare gas partner mass. Br_2 and the other interhalogens did follow the SSH theory trend for increased vibrational transfer probability with decreased vibrational energy spacing.

Previous energy transfer studies in the $\text{Br}_2(\text{B})$ predissociated states ($v' \geq 4$) indicated that vibrational energy transfer was an inefficient process compared to electronic removal through electronic quenching, spontaneous predissociation and collision-induced predissociation. However, in the lower v' levels where predissociation effects are minimized, state-to-state vibrational energy transfer was shown to compete favorably with pure electronic quenching.

3 Further Studies

Further vibrational transfer studies in $\text{Br}_2(\text{B})$ are underway to investigate molecular collision partners such as N_2 and O_2 where $\text{V} \rightarrow \text{V}$ transfer may be significant. Additional experiments should also be conducted to observe emissions from vibrational levels more than one quantum state away from the pumped level. This would provide a definitive

answer on the applicability of the Montroll-Shuler model to the $\text{Br}_2(\text{B})$ system. Finally, steady-state CW LIF experiments should be conducted in the low v' levels of $\text{Br}_2(\text{B})$ to investigate vibrational as well as rotational energy transfer.

Bibliography

1. Andrews, L.C. *Special Functions for Engineers and Applied Mathematicians*. MacMillan Publishing Company, New York, (1985).
2. Barrow, R. F., T. C. Clark, J. A. Coxon and K. K. Yee. "The $B^{\circ}\Pi(0_u^{+}) \rightarrow X^1\Sigma_g^{+}$ System of Br_2 : Rotational Analysis, Franck-Condon Factors, and Long Range Potential in the $B^{\circ}\Pi(0_u^{+})$ State," *Journal of Molecular Spectroscopy*, 51: 428-449 (1974).
3. Byer, R. L. et. al. "An Optically Pumped Molecular Iodine Laser," *Applied Physics Letters*, 20: 463 (1972).
4. Carrington, T. "Transition Probabilities in Multilevel Systems: Calculation from Impulsive and Steady-State Experiments," *Journal of Chemical Physics*, 35(3): 807-816 (1961).
5. Clyne, M. A. A. and M. C. Heaven, "Kinetics of Excited States of Br_2 Using Laser Excitation," *Journal of the Chemical Society Faraday Transactions II*, 76: 1992-2012 (1978).
6. Clyne, M. A. A. and J. A. Coxon. "The Emission Spectra of Br_2 and IBr Formed in Atomic Recombination Processes," *Journal of Molecular Spectroscopy*, 23: 258-271 (1967).
7. Clyne, M. A. A., J. A. Coxon and A. R. Woon Fat, "Recombination of Ground State Halogen Atoms," *Faraday Discussions of the Chemical Society*, 53: 82-99 (1972).
8. Clyne, M. A. A., J. A. Coxon and H. W. Cruse, "Electronic Energy Transfer to Dissociated Bromine by O_2 $^1\Sigma_g^{+}$, $^1\Delta_g$," *Chemical Physics Letters*, 6(1) (1967).
9. Clyne, M. A. A., M. C. Heaven and E. Martinez. "Kinetics of Excited States using Laser Excitation," *Journal of the Chemical Society Faraday Transactions II* 76: 405-419 (1980).

10. Clyne, M. A. A., M. C. Heaven and J. Tellinghuisen. "Theoretical Treatment of the Spontaneous Predissociation of Br_2 ($\text{B}^{\circ}\Pi(0_v^+)$)," *Journal of Chemical Physics* 76: 5341-5349 (1982).
11. Clyne, M. A. A., M. C. Heaven and S. J. Davis. "Laser-Excitation Studies in Br_2 ," *Journal of the Chemical Society Faraday Transactions II* 76: 961-978 (1980).
12. Coxon, J. A. "The $\text{B}^{\circ}\Pi(0^+) \rightarrow \text{X}^1\Sigma^+$ Emission Spectrum of ^{79}BrF and ^{81}BrF in the Range 625-870 nm," *Journal of Molecular Spectroscopy*, 87(1): 85 (1981).
13. Coxon, J. A. "The $\text{B}^{\circ}\Pi(0_v^+) \leftarrow \text{X}^1\Sigma_g^+$ system of $^{79}\text{Br}^{79}\text{Br}$," *Journal of Molecular Spectroscopy*, 37: 39-62 (1971).
14. Coxon, J. A., "Franck-Condon Factors and r-Centroids for Halogen Molecules--II. The $\text{B}^{\circ}\Pi(0_v^+) \leftarrow \text{X}^1\Sigma_g^+$ System of $^{79}\text{Br}^{81}\text{Br}$," *Journal of Quantum Spectroscopy and Radiation Transfer*, 12: 639-650" (1972)
15. Davis, S.J. "Potential of Halogen Molecules as Visible Chemical Laser Systems," AFWL-TR-79-104: 167, (1979).
16. Davis, S. J., L. Hanco and R. F. Shea. "Iodine MonoFluoride $\text{B}^{\circ}\Pi(0^+) \rightarrow \text{X}^1\Sigma^+$ Lasing From Collisionally Populated States," *Journal of Chemical Physics*, 78: 172 (1983).
17. Davis, S.J., L. Hanco and P.J. Wolf. "Continuous Wave Optically pumped Iodine Monofluoride $\text{B}^{\circ}\Pi(0^+) \rightarrow \text{X}^1\Sigma^+$ Laser," *Journal of Chemical Physics*, 82: 4831 (1985).
18. Heaven, M. C. "Fluorescence Decay Dynamics of the Halogens and Interhalogens," *Chemical Society Review*, 15: 405-448 (1986).
19. Herzberg, G. *Spectrum of Diatomic Molecules*. Van Nostrand, New York, 1953.

20. Hirschfelder, J.O., C.F. Curtis and R.B. Bird. *Molecular Theory of Gases and Liquids*. John Wiley and Sons, Inc., New York, 1110-1111, (1954).
21. Kitamura, M., K. Kuniaki, K. Suzuki, T. Kondow, K. Kuchitsu, T. Munakata and T. Kasuya. "Cross Sections for Fluorescence Quenching of Br₂ by Collision with Foreign Gases as Studied by Laser Excited Fluorescence," *Journal of Physical Chemistry* 90: 1589-1592" (1986).
22. Kronig, R. *Z. Phys.* 50: 347 (1928).
23. Kurzel, R.B. and J.I. Steinfeld. "Energy-Transfer Processes in Monochromatically Excited Iodine Molecules, III, Quenching and Multiquantum Transfer from $v' = 13$," *Journal of Chemical Physics*, 53: 3293 (1970).
24. Landau V. L. and E. Teller. *Phys Z Sowj Un.* 10: 35 (1936).
25. Lin, Yaomin. *Spectroscopic and Dynamic Studies of Br₂ and Open-Shell van der Waals Complexes*, Doctoral Dissertation, Emory University, 1991.
26. Luypaert, R., G. DeVlieger and J Van Craen. "Lifetimes and Collisional Quenching Cross Sections of Single Rotational States in Bromine," *Journal of Chemical Physics* 72(11): 6283-6288 (1980).
27. Massman, D. A. *Quenching and Rotational Energy Transfer in Molecular Bromine: Br₂ (B)^oΠ(0_u⁺)*, Master's Thesis, Air Force Institute of Technology (AU), GEP/91-J, May, 1991.
28. McAfee, K. B. and R. S. Hozack. "Lifetimes and Energy Transfer Near the Dissociation Limit in Bromine," *Journal of Chemical Physics* 64: 2491-2495 (1976).
29. McFeeters, B.D., G.P. Perram, R.P. Crannage and E.A. Dorko. "Long Wavelength Vibronic Band Analysis of the B^oΠ(0⁺)→X¹Σ⁺ Transitions of ⁷⁹Br³⁵Cl and ⁸¹Br³⁵Cl," *Chemical Physics*, 139: 347-357 (1989).

30. Melton, D. W. Capt, USAF. *Collisional Dynamics of the $B^{\circ}\Pi(0^{+})$ State of BrF*, Doctoral Dissertation, Air Force Institute of Technology (AU), DS/ENP/91-01, August, 1991.
31. Montroll, E.W. and K.E. Shuler. "Studies in Nonequilibrium Rate Processes: The Relaxation of a System of Harmonic Oscillators," *Journal of Chemical Physics*, 26: 454 (1957).
32. Mulliken, R. S. "The Interpretation of Band Spectra, Part III," *Review of Modern Physics*, 4:1-88 (1932).
33. Perram, G. P. Capt, USAF. *Collisional Dynamics of the B-State of Bromine Monochloride*, Doctoral Dissertation, Air Force Institute of Technology (AU), August, 1986.
34. Perram, G. P. and S. J. Davis. "Spectroscopic and Kinetic Studies of a Dye Laser Pumped Br_2 $B^{\circ}\Pi(0_u^{+}) \rightarrow X^1\Sigma_g^{+}$ Laser," *Journal of Chemical Physics* 84: 2526-2533 (1986).
35. Perram, G.P., D.A. Massman and S.J. Davis. "Quantum Resolved Rotational Energy Transfer in the $B^{\circ}\Pi(0_u^{+})$ State of Br_2 ," to be published.
36. Perram, G.P., D.W. Melton, T.L. Thompson and W.B. Roh. "Collisional Dynamics of the BrF $B^{\circ}\Pi(0^{+})$ state. II. Vibrational Energy Transfer," *Journal of Chemical Physics*, 97(5) 3258-3264.
37. Rao, Y.V., and P. Venkateswarlu. "Vacuum Ultraviolet Resonance Spectrum of Br_2 Molecule," *Journal of Molecular Spectroscopy*, 13: 288 (1964).
38. Schwartz, R.N., Z.I. Slawsky and K.F. Herzfeld. "Calculation of Vibrational Relaxation Times in Gases," *Journal of Chemical Physics*, 20: 1591 (1952).
39. Sinha, M.P., A. Schulz and R.N. Zare. "Internal State Distribution of Alkali Dimers in Nozzle Beams," *Journal of Chemical Physics*, 58(2): 549 (1973).

40. Smedley, J. E., H. K. Haugen and S. R. Leone. "Collision-induced Dissociation of Laser-Excited Br₂: Formation of Br ²P_{1/2} + ²P_{3/2} at Energies 1-5 kT Below Dissociation," *Journal of Chemical Physics*, 86(12): 6801-6812 (1987).
41. Steinfeld, J. I. "Rate Data for Inelastic Collision Processes in the Diatomic Halogen Molecules," *Journal of Physical and Chemical Reference Data* 13(2): 445 (1984).
42. Steinfeld, J. I. *Molecules and Radiation*. The MIT Press, Cambridge, 1974.
43. Steinfeld, J. I. and W. Klemperer. "Energy Transfer Processes in Monochromatically Excited Iodine Molecules. I. Experimental Results," *Journal of Chemical Physics*, 42: 3475 (1965).
44. Striganov, A. R. and N. S. Sventitskii. *Tables of Spectral Lines of Neutral and Ionized Atoms*. IFI/Plenum, New York-Washington, 1968.
45. Van de Burgt, L. J. and M. C. Heaven. "Rate Constants for Collisional Deactivation of Br₂ (B)^oΠ(0_u⁺) by Br₂ (X) and He," *Chemical Physics* 103: 407-416 (1986).
46. Wodarczyk, F. J. and H. R. Schlosser. "An Optically Pumped Molecular Bromine Laser," *Applied Physics Letters* 20: 4476 (1977).
47. Wolf, P. Capt, USAF. *Collisional Dynamics in the B^oΠ(0⁺) State of Iodine Monofluoride*, Doctoral Dissertation, Air Force Institute of Technology (AU), 1986.
48. Yamasaki, K. and S. R. Leone. "Quenching and Energy Transfer Processes of Single Rotational Levels of Br₂ (B)^oΠ(0_u⁺) v'=24 with Ar Under Single Collision Conditions," *Journal of Chemical Physics* 90: 964-976 (1989).
49. Yardley, J. T. *Introduction to Molecular Energy Transfer*. Academic Press, New York, 95-110, (1980).

Appendix A. Br_2 Spectroscopy

1 Spectroscopic Constants

Dunham expansion molecular constants for the $\text{B}^3\Pi(0_u^+)$ electronically excited state and $\text{X}^1\Sigma_g^+$ ground electronic state of the three Br_2 isotopomers reported by Barrow and coworkers (2) listed in Table A.1. The Dunham expansion coefficients for the $\text{B}^3\Pi(0_u^+)$ state are only valid for $v' \leq 8$. Because of this, Barrow also reported a complete set of vibrational level term values for each vibrational level investigated in both the B and X states in the $^{79}\text{Br}_2$ and $^{81}\text{Br}_2$ isotopes. Term values for the $^{79}\text{Br}_2$ isotope were used in the current work and are listed in Table A.2.

2 Franck-Condon Factors

Franck-Condon factors for the $^{79}\text{Br}^{81}\text{Br}$ isotope $\text{B} \rightarrow \text{X}$ transition have been reported by Coxon (12). Coxon's calculations used a Morse potential for both the X and B states which is clearly inaccurate, especially for the extrapolations to high v'' values. However, for the transitions studied in the present work, Coxon's values compared favorably with those calculated by Barrow for the $^{79}\text{Br}_2$ and $^{81}\text{Br}_2$ isotopes where a more sophisticated RKR potential was used for both the X and B states (2) and, thus, were used in the current studies to determine isolated (v', v'') observation transitions for the vibrational transfer work. Coxon's Franck-Condon factors for the (v', v'') pertinent to the current work are given in Table A.3.

Table A.1
Molecular Constants (cm^{-1}) for the $\text{B}^3\Pi(0_u^+)$ and $\text{Br}_2 \text{X}^1\Sigma_g^+$ States of Br_2 from
Barrow and coworkers (2)

State	Term	$^{79}\text{Br}_2$	$^{81}\text{Br}_2$	$^{79}\text{Br}^{81}\text{Br}$
$\text{B}^3\Pi(0_u^+)$ $v' \leq 8$	T_{00}	15823.47	15824.46	15823.96
	T_e	15902.47	15902.47	15902.47
	ω_e	167.6066	165.5244	166.5688
	$\omega_e \chi_e$	1.63608	1.5957	1.6159
	$10^3 \omega_e y_e$	-9.3687	-9.0238	-9.1957
	$10^8 B_e$	5.9589	5.8118	5.8853
	$10^4 \alpha_e$	4.89095	4.7109	4.8007
	$10^6 \gamma_e$	-6.6369		
		3.013	2.866	2.939
	$10^8 D_e$			
	ω_e	325.3213	321.29	323.3069
	$\omega_e \chi_e$	1.07742	1.064	1.0641
	$10^3 \omega_e y_e$	-2.29798	-2.2134	-2.2556
	$10^8 B_e$	8.2107	8.0088	8.1093
$\text{X}^1\Sigma_g^+$ $v'' \leq 10$	$10^4 \alpha_e$	3.1873	3.19	3.1285
	$10^6 \gamma_e$	-1.045		
	$10^8 D_e$	2.092	1.990	2.041

Table A.2
Term Values (cm^{-1}) for the $X^1\Sigma_g^+$ and $B^3\Pi(0_u^+)$ States
of Br_2 from Barrow and coworkers (2)

	v'	$T_v, J=0$	$10^2 B_v$	$10^8 D_v$	$-10^{13} H_v$
$B^3\Pi(0_u^+)$	55	19578.53	0.4539	465.00	
	54	77.85	0.5482	169.9	
	53	76.46	0.6880	119.7	
	52	74.47	0.8435	114.1	
	51	71.74	1.0063	118.4	
	50	68.20	1.1276	88.77	
	49	63.64	1.2704	85.49	
	48	57.96	1.4055	73.97	
	47	51.00	1.5398	63.95	
	46	42.61	1.6768	59.36	
	45	32.64	1.8158	55.39	
	44	20.98	1.9453	48.24	
	43	07.45	2.0778	43.95	
	42	19451.95	2.2058	39.03	
	41	74.35	2.3306	34.48	
	40	54.48	2.4557	30.70	
	39	32.25	2.5791	28.07	
	38	07.51	2.7048	26.30	
	37	19380.20	2.8239	23.01	
	36	50.12	2.9455	22.26	
	35	17.22	3.0640	20.79	
	34	19281.36	3.1815	19.70	
	33	42.44	3.2944	18.12	
	32	00.32	3.4065	16.81	
	31	19154.90	3.5184	15.59	
	30	06.05	3.6283	15.08	23.40
	29	19053.71	3.7338	13.56	9.91
	28	18997.73	3.8392	12.30	5.57
	27	38.04	3.9444	12.29	10.40
	26	18874.56	4.0451	10.96	5.84
	25	07.20	4.1453	9.89	5.80
	24	18735.86	4.2426	9.63	2.76
	23	18660.52	4.3404	9.26	8.721
	22	18581.13	4.4338	8.98	8.61
	21	18497.66	4.5230	8.09	4.69
	20	18410.07	4.6122	7.74	5.59

Table A.2 (continued)

	v'	$T_{v',J=0}$	$10^2 B_2$	$10^8 D_v$	$-10^{-13} H_v$
$B^3\Pi(0_u^+)$	19	18318.33	4.6979	7.36	4.87
	18	18222.46	4.7801	6.49	2.63
	17	18122.45	4.8626	6.24	4.29
	16	18018.37	4.9399	5.5	1.55
	15	17910.18	5.0181	5.7	2.44
	14	17797.88	5.0927	5.4	1.71
	13	17681.50	5.1644	5.1	0.76
	12	17561.14	5.2363	5.2	1.99
	11	17436.89	5.3039	5.0	1.77
	10	17308.65	5.3687	4.4	1.03
	9	17176.65	5.4340	4.40	1.65
	8	17040.78	5.4956	4.18	1.40
	7	16901.15	5.5544	4.00	0.88
	6	16757.83	5.6123	3.81	0.60
	5	16610.87	5.6697	3.64	0.59
	4	16460.33	5.7260	3.53	0.67
	3	16306.26	5.7799	3.42	0.57
	2	16148.73	5.8320	3.33	0.42
	1	15987.78	5.8840	3.23	0.38
	0	15823.47	5.9342		0.31
$X^1\Sigma_g^+$	10	3132.03	7.8648		
	9	2828.96	7.8983		
	8	2523.58	7.9321		
	7	2215.93	7.9658		
	6	1906.05	7.9991		
	5	1593.90	8.0323		
	4	1279.52	8.0654	2.135	
	3	962.94	8.0979	2.129	
	2	644.14	8.1304	2.116	.00288
	1	323.16	8.1627	2.108	.00289
	0	0.0	8.1947	2.097	.00300

Table A.3
Franck-Condon Factors for selected $^{79}\text{Br}^{81}\text{Br}$ B \rightarrow X (v',v'')
transitions from Coxon (13)

$v' v''$	0	1	2	3	4	5	6
0	3e-10	8e-9	1e-7	1e-6	1e-5	3e-5	1.3e-4
1	4e-9	1e-7	1e-6	1e-5	6e-5	2.8e-4	1.02e-3
2	3e-8	7e-7	8e-6	6e-5	3e-4	1.22e-3	3.91e-3
3	1e-7	3e-6	1.1e-4	2.2e-4	1.02e-3	3.64e-3	1.02e-2
4	6e-7	1e-5	2.8e-4	6.3e-4	2.65e-3	8.32e-3	1.99e-2
5	2e-6	3e-5	6.4e-4	1.51e-3	5.64e-3	1.54e-2	3.13e-2

$v' v''$	7	8	9	10	11	12	13
0	4.6e-4	1.37e-3	3.52e-3	7.88e-3	1.56e-2	2.76e-2	4.42e-2
1	3.07e-3	7.78e-3	1.67e-2	3.08e-2	4.85e-2	6.57e-2	7.63e-2
2	1.02e-2	2.17e-2	3.83e-2	5.56e-2	6.55e-2	6.07e-2	4.11e-2
3	2.24e-2	3.95e-2	5.50e-2	5.88e-2	4.50e-2	2.02e-2	1.86e-3
4	3.67e-2	5.16e-2	5.31e-2	3.61e-2	1.17e-2	1e-4	1.20e-2
5	4.69e-2	4.98e-2	3.33e-2	9.05e-3	3.50e-4	1.54e-7	3.37e-2

Appendix B. Basic Energy Transfer Theories

This appendix describes the basic energy transfer processes used in this dissertation. These processes include the gas kinetic collision rate , the Landau-Teller theory , the Schwartz, Slawsky and Herzfeld (SSH) theory (49) and the Montroll-Shuler model . The implementation of the Montroll-Shuler model as a user-defined function in Jandel-Scientific TableCurve is also presented as is a description of the five-level numerical solution to the Montroll-Shuler model.

1 Gas Kinetic Collision Rates

The elastic, hard sphere collision frequency for molecule A with collision partner B is given by

$$Z_A = N_B \sigma_g v_{AB} \quad (B.1)$$

where

Z_A = collision frequency (1/sec)

N_B = number density of particle species B

σ_g = velocity averaged collision cross section = $\pi (r_A + r_B)^2$

r_A = radius of particle A

r_B = radius of particle B

v_{AB} = average relative speed of collision partners = $(8k_B T / \pi \mu)^{1/2}$

μ = collision pair reduced mass

The rate constant for bimolecular gas kinetic collisions is given by

$$k_g = \sigma_g v_{AB} \quad (B.2)$$

This value is commonly used as the standard for comparing the relative efficiency of various kinetic processes. The probability of occurrence for any given kinetic process is defined as

$$P = \sigma / \sigma_g \quad (\text{B.3})$$

where

σ = cross-section for given kinetic process

P = Probability for process σ occurring during a single collision

Hard sphere cross-sections, reduced masses, relative velocities and gas kinetic rate constants for Br₂ with the collision partners used in this study are given in Table B.1. Hard sphere cross sections were calculated with atomic and molecular radii derived for a (6,12) Lennard-Jones potential from viscosity data tabulated in reference (20).

2 Landau Teller Theory

Landau and Teller (24) developed an elementary vibrational transfer theory that neglected the long range attractive intermolecular potential. A repulsive limb interaction potential of the form $V(r) = V_0 \exp(-\alpha \cdot r)$ where $\alpha = 2\pi \nu_0 / v$, ν_0 is the oscillator frequency and v is the relative velocity of the collision partners was used to calculate the probability for vibrational transfer from $v'=1$ to $v'=0$ using time-dependent perturbation theory. The resulting average probability of vibrational transfer per collision is given by Yardley (49) as

$$P_{10} \propto \exp \left\{ -3 \left(2\pi^4 \mu \nu_0^2 / \alpha^2 k_B T \right)^{-1/3} \right\} \quad (\text{B.4})$$

Table B.1

Gas Kinetic Collision Parameters for Br₂ Collisions

Collision Partner	Cross-Section (Angstroms ²)	Reduced Mass (a.u.)	Velocity (cm/sec)	Gas Kinetic Rate Constant (cm ³ /molec sec)
He	36.8	3.90	1.4×10^5	5.20×10^{-10}
Ne	39.1	17.9	6.6×10^4	2.58×10^{-10}
Ar	46.4	31.9	4.9×10^4	2.29×10^{-10}
Kr	48.7	54.8	3.8×10^4	1.84×10^{-10}
Xe	54.4	71.7	3.3×10^4	1.79×10^{-10}
Br ₂	57.2	79.0	3.1×10^4	1.80×10^{-10}

This equation indicates that efficient transfer is favored for small reduced masses, small vibrational spacings, short interaction distances and high temperatures. Matrix elements calculated for collisional vibrational transitions are proportional to those for radiative transitions. Selection rules dictate transitions between adjacent states only ($\Delta v = \pm 1$). Transition probabilities scale by vibrational level as

$$P_{v,v-1} = v \cdot P_{10} \quad (\text{B.5})$$

3 SSH Theory

The SSH theory is another widely used vibrational transfer theory proposed by Schwartz, Slawsky and Herzfeld (38). Often used as the basis for evaluating experimentally derived vibrational transfer rates, the SSH theory includes an attractive potential term which was neglected in the

Landau-Teller Theory. Their potential has the form

$$V(r) = V_o \exp(-\alpha \cdot r) - \epsilon \quad (\text{B.6})$$

The addition of the attractive term (ϵ = the potential well depth) causes a slight increase in translational energy just prior to reaching the repulsive potential, thus increasing vibrational transfer probabilities. The resulting probability for vibrational transfer from $v'=1$ to $v'=0$ for the SSH theory is, again, given by Yardley (49) as

$$P_{10} \propto \left(\frac{\Theta'}{\Theta_{SSH}} \right) \left(\frac{\Theta'}{T} \right)^{1/6} \exp \left[-\frac{3}{2} (\Theta'/T)^{1/3} + (\Theta_{SSH}/2T) + (\epsilon/k_B T) \right] \quad (\text{B.7})$$

where

$$\Theta' = 4\pi^2 L^2 \omega^2 \mu / k_B$$

$$\Theta_{SSH} = \omega_e / k_B$$

$$\omega_e = \text{vibrational energy spacing}$$

$$L = \text{interaction length}$$

If the exponential terms dominate the probability function above, the logarithm of P_{10} can be written as

$$\ln(P_{10}) = A - B \mu^{1/3} \omega^{2/3} \quad (\text{B.8})$$

where A and B are constants related to the same parameters as Eq (B.7).

This form of the SSH vibrational transfer probability equation is most often used for examining experimentally determined vibrational transfer rate constants and cross-sections.

4 Montroll-Shuler Model

The Montroll-Shuler model provides an analytic solution to the master rate equation for vibrational relaxation in a system of harmonic oscillators immersed in a chemically inert, constant temperature heat bath. Only first order transfer processes are considered, i.e., the ratio of excited vibrational state to bath gas populations are small so the excited molecules interact only with bath gas molecules. Radiative and electronic quenching mechanisms have been included so that the model can be applied to vibrational manifolds of electronically excited states.

Landau-Teller theory, described previously in this appendix, is used for vibrational scaling of the state-to-state rate coefficients by

$$\begin{aligned} k_v(v', v'-1) &= v k_v(1,0) \\ |\Delta v| &= 1 \text{ only} \end{aligned} \quad (\text{B.9})$$

Inverse rates ($\Delta v = +1$) are calculated by applying the principle of detailed balance

$$k_v(v'-1, v') = k_v(v', v'-1) \exp(-\Delta \epsilon_{v', v'-1} / k_B T) \quad (\text{B.10})$$

Radiative decay and electronic quenching rates are assumed to be independent of vibrational state. These processes can then be added to the original Montroll-Shuler solution by simply transforming the population by

$$\begin{aligned} z_n(t) &= x_n(t) \exp(t/\tau_0) \\ 1/\tau_0 &= 1/\tau_r + \sum_Y k_q^Y Y \end{aligned} \quad (\text{B.11})$$

where the summation over Y indicates is needed for the possibility of multiple buffer species. Each element of the tridiagonal rate matrix, R_{pq} ,

can be totally described by the radiative lifetime, electronic quenching rate and the fundamental vibrational transfer rate. Combining these assumptions the master rate equation can be written as

$$dz_n/dt = k_v^M(1,0) \{ ne^{-\Theta} z_{n-1} - [n + (n+1)e^{-\Theta}] z_n + (n+1) z_{n+1} \} \quad (B.12)$$

where Θ in this case is defined by

$$\Theta = h\omega/k_B T$$

If a particular state, q , is populated instantaneously at time $t=0$, the Montroll-Shuler solution to the master rate equation for the normalized population distribution (1/volume) in state p is given by

$$x_p(t) = \frac{(1-e^{-\Theta}) e^{q\Theta} e^{-\Gamma_o t}}{(e^{-t'} - e^{-\Theta})} \left(\frac{e^{-t'} - 1}{e^{-t'} - e^{-\Theta}} \right)^{p+q} F(-p, -q, 1; u^2) \quad (B.13)$$

where

$$\Gamma_o = 1/\tau_o = 1/\tau_r + \sum_Y k_q^Y Y$$

$$\Theta = \omega_e/k_B T$$

$$\omega_e = \text{the fundamental vibrational frequency}$$

$$t' = t(1 - e^{-\Theta}) \Gamma_v$$

$$\Gamma_v = \sum_Y k_v^Y(1,0) Y$$

$$u = \sinh(\Theta/2)/\sinh(t'/2)$$

$$F = \text{hypergeometric function}$$

5 Montroll-Shuler Model TableCurve Implementation

An important analytical tool for this dissertation research was the TableCurve curve fitting software package from Jandel Scientific. The TableCurve package had many features that eliminate many of the typical difficulties encountered when analyzing temporally resolved fluorescence data. The two TableCurve user-defined functions (UDF) allow the user to program customized functional forms to be used by the nonlinear least-squares fitting engine. TableCurve also calculates a wide variety of statistical data for each fitting run.

For this study, it was necessary to implement the Montroll-Shuler solution to the master rate equation shown in the previous section as a user defined function UDF in TableCurve . Functional formatting requirements for UDFs in TableCurve allow for no more than eight lines of pseudo-coded functional relationships using only those functional forms supported by the software. The most difficult portion of the Montroll-Shuler implementation was to accurately reduce the functional form of the hypergeometric function, $F(-v; -w; 1; u^2)$, which is not supported by TableCurve. The general form of the hypergeometric function is given (1) as

$$F(a; b; c; x) = \sum_{n=0}^{\infty} \frac{(a)_n (b)_n}{(c)_n} \frac{x^n}{n!} \quad |x| < 1 \quad (\text{B.14})$$

where $(a)_n$ is called a Pochhammer symbol given by

$$(a)_n = a(a+1) \cdots (a+n-1) \quad n = 1, 2, 3, \dots \quad (\text{B.15})$$

It is clear from Eqn B.15 that if a or $b < 1$, the hypergeometric series is finite. In other words, if $a = -m$, then $(-m)_n = 0$ for all $n \geq m$, thereby terminating the series. In the case of the Montroll-Shuler model, both a and b are negative and the hypergeometric function becomes

$$F(-v; -w; 1; u^2) = \sum_{n=0}^m \frac{(-v)_n (-w)_n}{(1)_n} \frac{(u^2)^n}{n!} \quad (\text{B.16})$$

where m is equal to the smaller value of v and w . Unfortunately, TableCurve does not directly support the Pochhammer or hyperbolic sine functional forms. However, the Pochhammer form can be written as

$$(-a)_n = (-1)^n a(a-1)(a-2) \cdots (a-n+1) = \frac{(-1)^n a!}{(a-n)!} \quad (\text{B.17})$$

and the hyperbolic functions can be expressed as the difference of two exponential functions. The hypergeometric function can thus be simplified to the form

$$F(-v; -w; 1; u^2) = v!w! \sum_{n=0}^m \frac{(u^2)^n}{(v-n)!(w-n)!(n!)^2} \quad (\text{B.18})$$

The total general Montroll-Shuler function was implemented as a UDF in the following format:

```

T = 0.655
# F1 = X [1 - exp(-T)] # A
# F2 = exp(-X/#B) [1 - exp(T)] exp(w T)
# F3 = [exp(-#F1) - 1]^(v+w) / [exp(-#F1) - exp(T)]^(v+w+1)
# F4 = {[exp(T/2) - exp(-T/2)] / [exp(#F1/2) - exp(-#F1/2)]}^2

```

$$\#F5 = (\#F4)^n / \{(n!)^2 (v-n)!(w-n)!\}$$

$$\#F6 = v! w! \sum_{n=0}^m \#F5$$

$$Y = \#C \#F2 \#F3 \#F6$$

where $T = \omega_e/kT$ is the ratio of the $Br_2(B)$ state vibrational energy spacing to the average thermal energy and $\#A$, $\#B$ and $\#C$ are the fitting parameters where $\#A = \Gamma_v$, $\#B = 1/\Gamma_o$, and $\#C$ is a magnitude scaling factor. The TableCurve model was tested for each pump/view level combination by generating test data with Mathematica, which directly supports the hypergeometric function. In all cases, the TableCurve fitting routine obtained Γ_v and Γ_o values that were identical to the values used to generate the test data.

6 *Development of the Eigenvalue Solution to a Five-level Montroll-Shuler System*

This section discusses the methodology for obtaining the numerical eigenvalue solution for a five level, Montroll-Shuler-like $V \rightarrow T$ transfer system with vibrational state independent electronic removal mechanisms that follows Landau-Teller scaling and detailed balance. The other n -level systems discussed in chapter IV are obtained in an analogous manner. As discussed earlier in this Appendix, Landau-Teller scaling uses the vibrational transfer scaling rule $\Delta v = \pm 1$. Vibrational transfer rates are multiples of the fundamental vibrational transfer rate, $k_v(1,0)$, and scale as

$$k_{v \rightarrow v-1} = v k_v(1,0) \quad (B.19)$$

Inverse rates are calculated by detailed balance

$$k_{v \rightarrow v+1} = (v+1)k_v(1,0)\exp(-\Delta E_{v+1,v}/kT) \quad (\text{B.20})$$

Additionally, it is assumed that the electronic removal rates are independent of vibrational level. These assumptions are identical to those of the Montroll-Shuler model (with the exception of a finite number of vibrational levels). Therefore, Eq (B.12) can be used to calculate the rate matrix equation

$$\begin{aligned} \dot{\mathbf{z}}(t) = \Gamma_v \begin{pmatrix} -(4+5e^{-\Theta}) & 4e^{-\Theta} & 0 & 0 & 0 \\ 4 & -(3+4e^{-\Theta}) & 3e^{-\Theta} & 0 & 0 \\ 0 & 3 & -(2+3e^{-\Theta}) & 2e^{-\Theta} & 0 \\ 0 & 0 & 2 & -(1+2e^{-\Theta}) & e^{-\Theta} \\ 0 & 0 & 0 & 1 & -e^{-\Theta} \end{pmatrix} \mathbf{z}(t) \\ = \mathbf{A}\mathbf{z}(t) = \lambda\mathbf{z}(t) \end{aligned} \quad (\text{B.21})$$

where

$$\mathbf{z}(t) = \mathbf{x}(t)\exp(\Gamma_o t)$$

$$\Theta = \omega_e/k_B T$$

$$\Gamma_v = k_v(1,0)[M]$$

$$\Gamma_o = k_q[M] + 1/\tau_{\text{rad}}$$

as in the Montroll-Shuler model described earlier in this appendix.

Eigenvalues and eigenvectors were calculated for the rate matrix, \mathbf{A} with Mathematica. Numerical solutions of the form

$$z_i(t) = \sum_j C_j \mathbf{u}_i^j \exp(\lambda_j t) \quad (\text{B.22})$$

where

u_i^j is the i^{th} element of the j^{th} eigenvector

λ_j is the j^{th} eigenvalue

C_j are the initial condition constants defined by the equations

$$z_i(0) = \sum_j C_j u_i^j \quad (\text{B.23})$$

were written for each pump-view combination. Solutions were of the form

$$\begin{aligned} x_2(t) = & D_1 \exp\{-(9.2 \cdot \Gamma_v + \Gamma_o)t\} + D_2 \exp\{-(5.1 \cdot \Gamma_v + \Gamma_o)t\} \\ & + D_3 \exp\{-(0.93 \cdot \Gamma_v + \Gamma_o)t\} + D_4 \{-(2.5 \cdot \Gamma_v + \Gamma_o)t\} \\ & + D_5 \exp\{-(0.04 \cdot \Gamma_v + \Gamma_o)t\} \end{aligned} \quad (\text{B.24})$$

where the values for D_1 through D_5 were calculated from Eq (B.23). The relative magnitudes of the coefficients may determine if one of the five exponential terms will dominate the temporal profile of the simulated data. Each n -level model discussed in the text will use an $n \times n$ $V \rightarrow T$ transfer rate matrix and will have a functional form similar to Eq (B.24) consisting of n exponential terms.

Appendix C. Experimental Calibrations and Calculations

1 Monochromator Resolution

The spectral resolution of the Instruments SA HR-640 0.64 meter monochromator used in the spectroscopic and vibrational transfer studies, shown as a function of slit width in Figure C.1, was determined by Melton (30). Resolution was measured as the full width at half maximum (fwhm) of a spectral line from a Hg lamp. Slit widths of 50 and 150 μm were used in the spectroscopic work yielding spectral resolutions of 1.5 and Angstroms, respectively. Slit widths of 1 mm were used for the vibrational transfer experiments to maximize the LIF signal from collisionally populated states. Extrapolation from Figure C.1 yields a spectral resolution of 22.4 angstroms for 1 mm slit widths.

Absolute wavelength calibration for the monochromator was determined from comparisons with emission lines from Ne, Ar and Kr spectral calibration lamps over the entire 560-1000 nm range used in the spectroscopy study. Differences between the monochromator readout and the calibration lamp wavelengths were fit to a three term polynomial.

2 Spectral Overlap Calculations

Vibrational bands in the $\text{Br}_2(\text{B} \rightarrow \text{X})$ emission spectrum are severely overlapped. It is clear from the vibrational transfer emission spectrum in Figure 4.1 that the odd numbered v' levels do not significantly overlap even

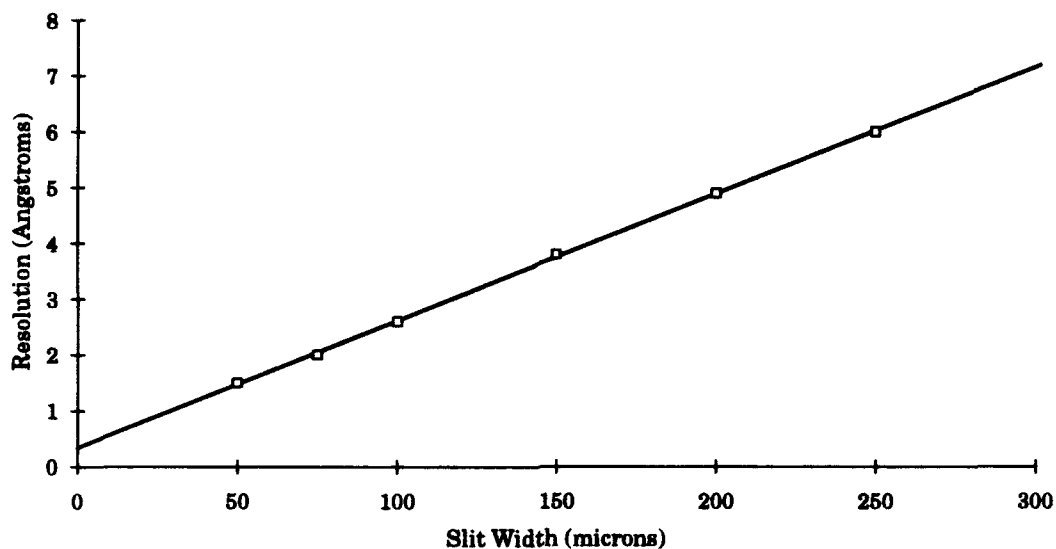


Figure C.1. Spectral resolution of the ISA HR-640 0.64 m monochromator

numbered v' levels, even at the 22.4 Angstrom resolution used in the current vibrational transfer experiments. Overlaps between odd only or even only v' transitions can be considerable. This section outlines the methodology for selecting (v', v'') observation transitions that are sufficiently free of overlap from competing bands.

The intensity observed at a particular wavelength is the sum of the emissions from all (v', v'') transitions falling within the spectral resolution of the detection system. This can be written as

$$I_{\text{obs}} = C \sum_{v'v''} q_{v'v''} N_{v'} h(\lambda_{\text{obs}} - \lambda_{v'v''}) \quad (\text{C.1})$$

where C is an arbitrary scaling constant, $q_{v',v''}$ is the Franck-Condon factor for the (v',v'') transition, $N_{v'}$ is the number density in vibrational level v' and $h(\lambda_{\text{obs}} - \lambda_{v',v''})$ is the response function of the detection system at the observed wavelength with respect to the bandhead wavelength of the (v',v'') transition. In previous vibrational transfer studies in BrCl and BrF, Perram (33) and Melton (30) used a triangular form of $h(\lambda_{\text{obs}} - \lambda_{v',v''})$ to calculate overlap fractions. In the current study, however, the bandhead wavelengths for $(v',v'') = (v'_0 \pm 2, v''_0 \pm 1)$ transitions fall within the monochromator resolution element. Transitions from $v'_0 \pm 1$ levels are almost totally isolated from the monochromator resolution element. Consequently, $h(\lambda_{\text{obs}} - \lambda_{v',v''})$ serves to select transitions from odd only or even only v' levels. The overlap fractions for the (v',v'') transitions given in Table 4.1 were determined from comparisons of the Franck-Condon factor of the (v',v'') transition and the Franck-Condon factors of the $(v' \pm 2, v'' \pm 1)$ transitions.

Appendix D. Rare Gas Vibrational Transfer Data

This appendix includes plots of the vibrational transfer data from the rare gas studies discussed in Chapter IV. Vibrational transfer waveforms and the respective Montroll-Shuler fits as well as typical Stern-Volmer plots used to derive the fundamental vibrational transfer rate coefficients and quenching rates are included for each collision partner. Additionally, logarithmic displays of the Montroll-Shuler fits to satellite waveforms are presented to emphasize non-Montroll-Shuler behavior, especially at higher pressures.

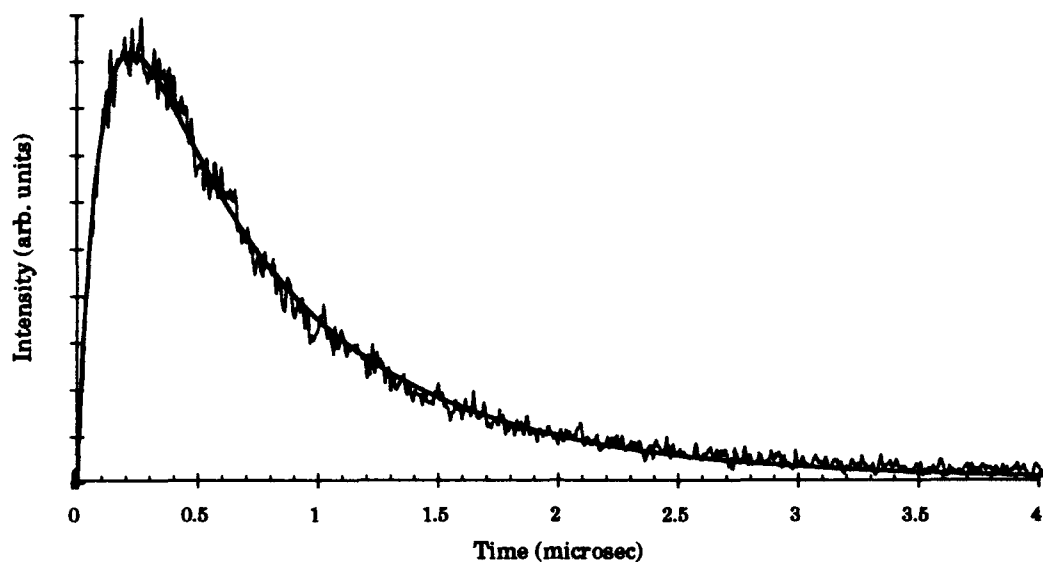


Figure D.1. Montroll-Shuler fit to emissions from the (2-11) band transition after initial excitation of $v'=3$ with 540 mTorr of Br_2 and 440 mTorr of Argon

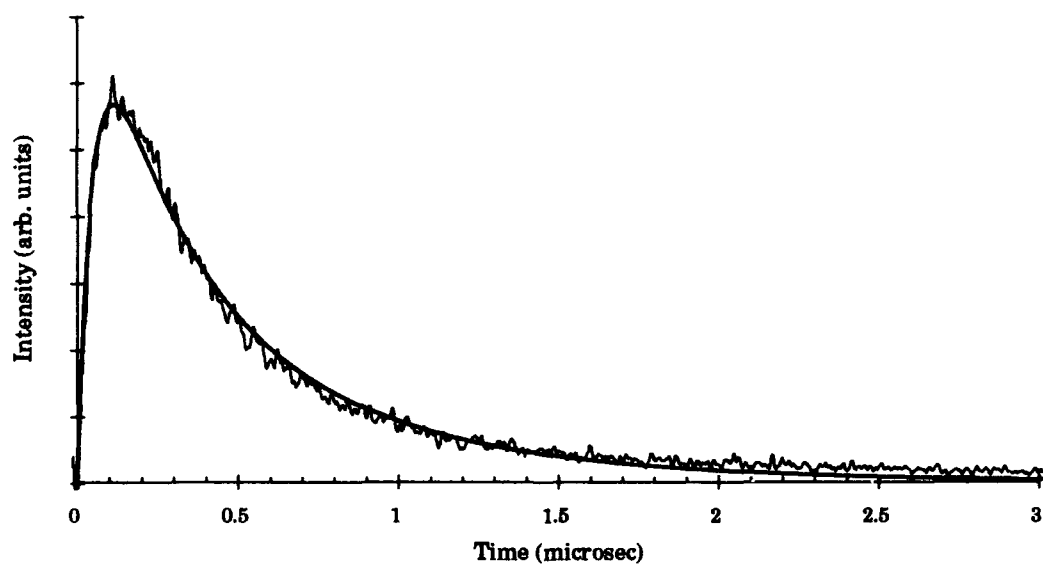


Figure D.2. Montroll-Shuler fit to emissions from the (2-11) band transition after initial excitation of $v'=3$ with 540 mTorr of Br_2 and 3.4 Torr of Argon

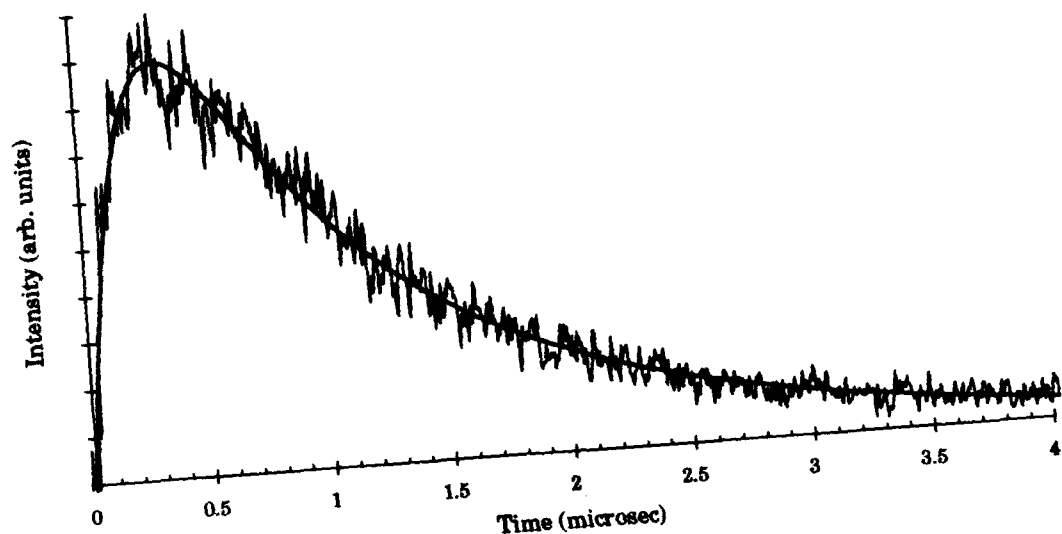


Figure D.3. Montroll-Shuler fit to emissions from the (1-12) band transition after initial excitation of $v'=2$ with a 790 mTorr of Br_2 and 300 mTorr of Argon

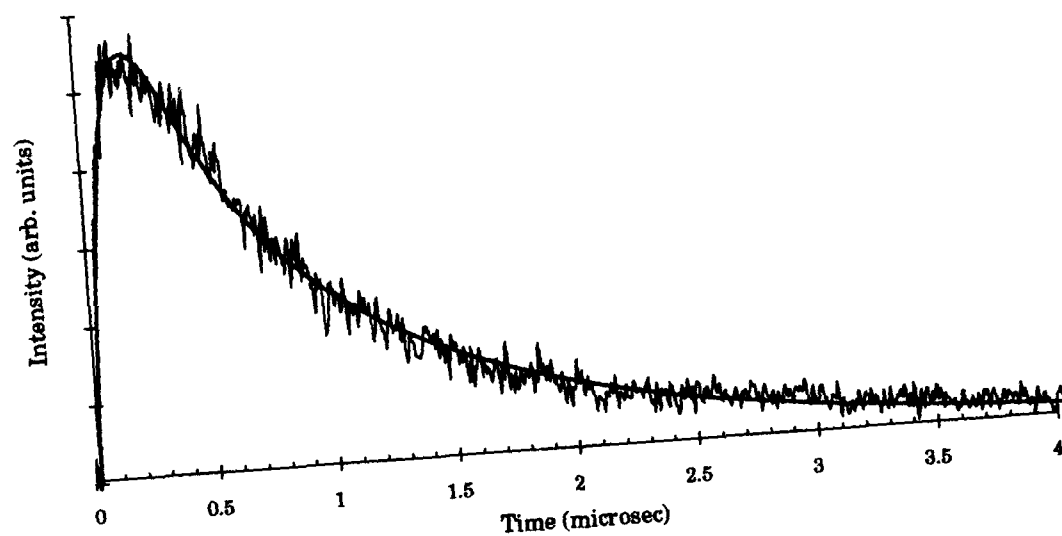


Figure D.4. Montroll-Shuler fit to emissions from the (1-12) band transition after initial excitation of $v'=2$ with 790 mTorr of Br_2 and 1.8 Torr of Argon

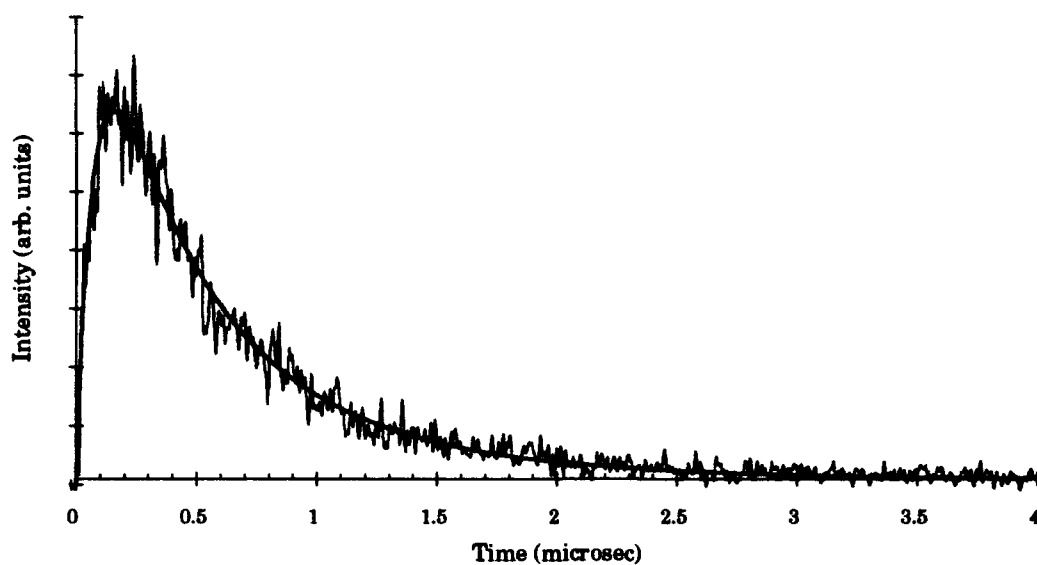


Figure D.5. Montroll-Shuler fit to emissions from the (3-9) band transition after initial excitation of $v'=2$ with 810 mTorr of Br_2 and 330 mTorr Argon

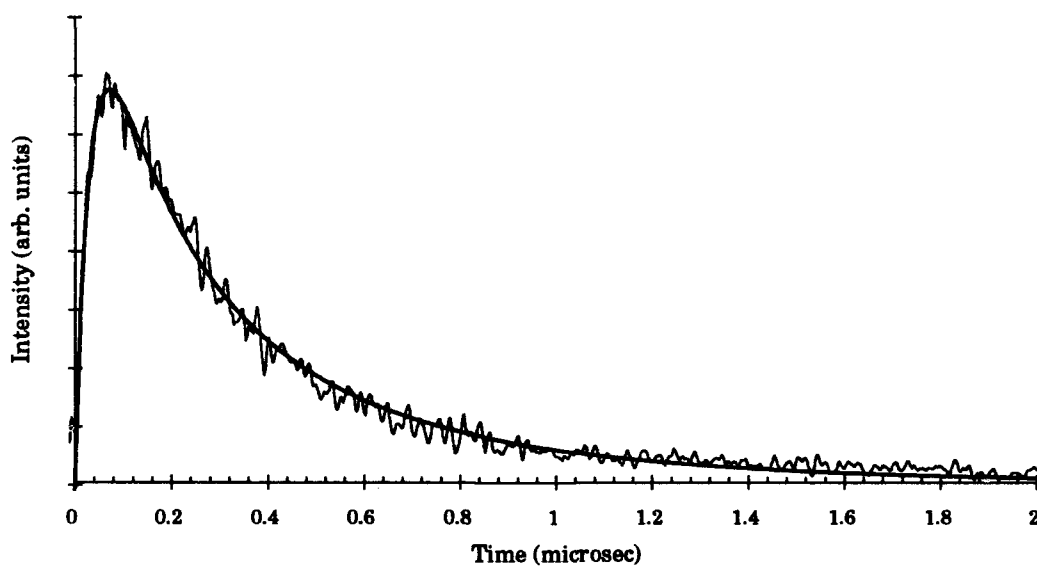


Figure D.6. Montroll-Shuler fit to emissions from the (3-9) band transition after initial excitation of $v'=2$ with 810 mTorr of Br_2 and 3.1 Torr of Argon

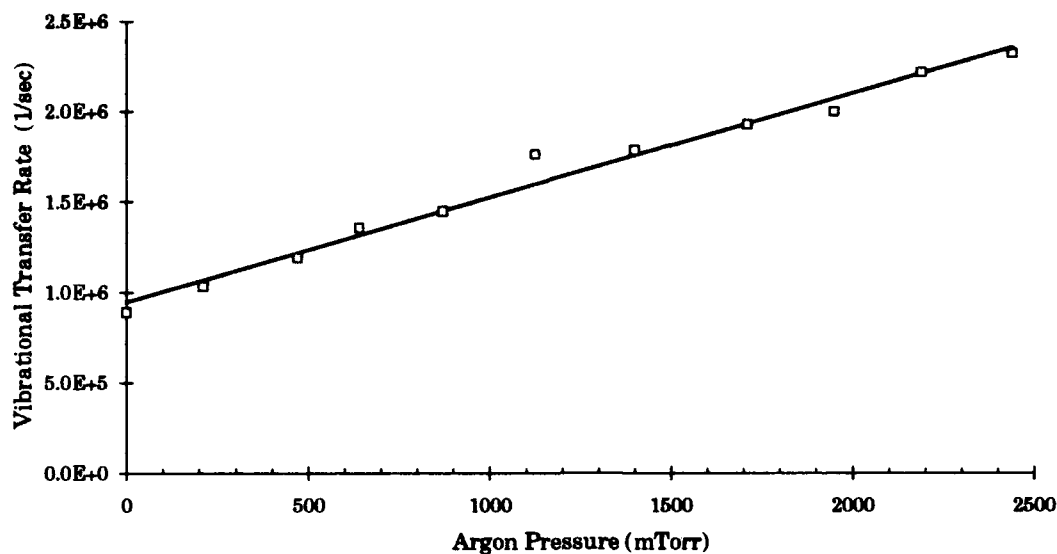


Figure D.7. Stern-Volmer plot of the Montroll-Shuler vibrational transfer fits to the combined pump $v'=3$ view $v'=2$ data with Argon buffer gas $k_v(1,0) = 2.1 (\pm 0.1) \times 10^{-11} \text{ cm}^3/\text{molec}\cdot\text{sec}$

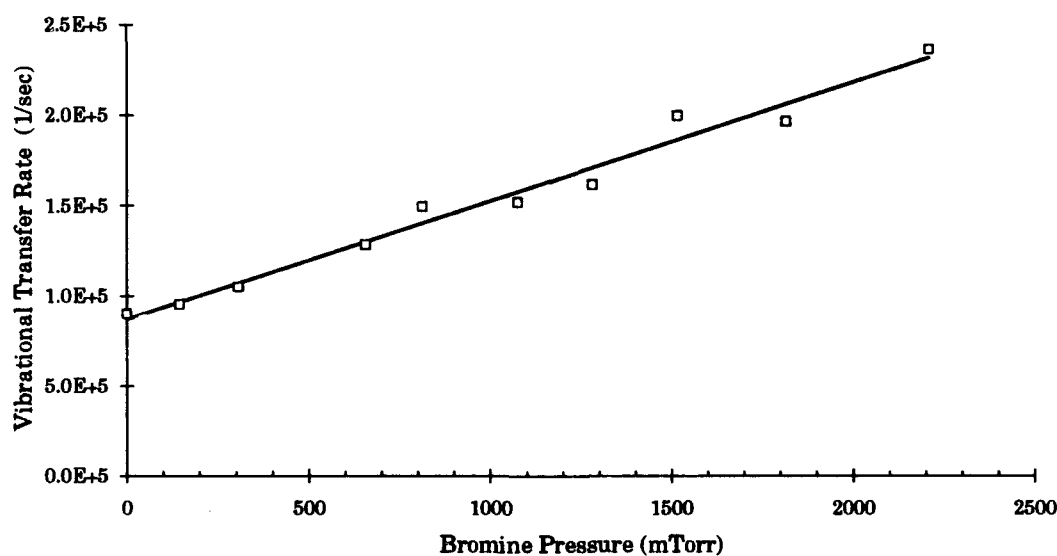


Figure D.8. Stern-Volmer plot of the Montroll-Shuler vibrational transfer fits to the combined pump $v'=2$ view $v'=1$ data with Argon buffer gas $k_v(1,0) = 2.3 (\pm 0.1) \times 10^{-11} \text{ cm}^3/\text{molec}\cdot\text{sec}$

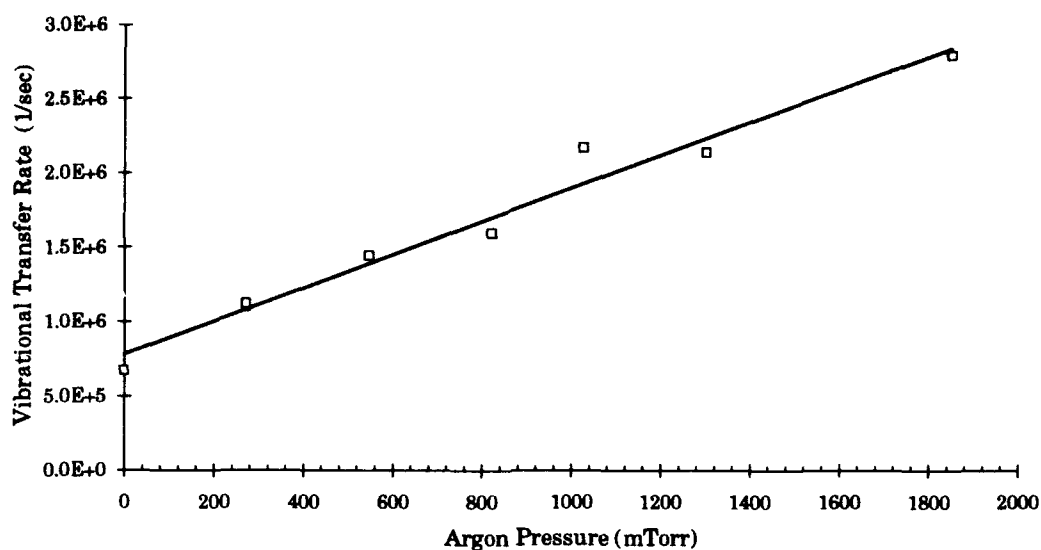


Figure D.9. Stern-Volmer plot of the Montroll-Shuler vibrational transfer fits to the combined pump $v'=2$ view $v'=3$ data with Argon buffer gas $k_v(1,0) = 2.3 (\pm 0.1) \times 10^{-11} \text{ cm}^3/\text{molec}\cdot\text{sec}$

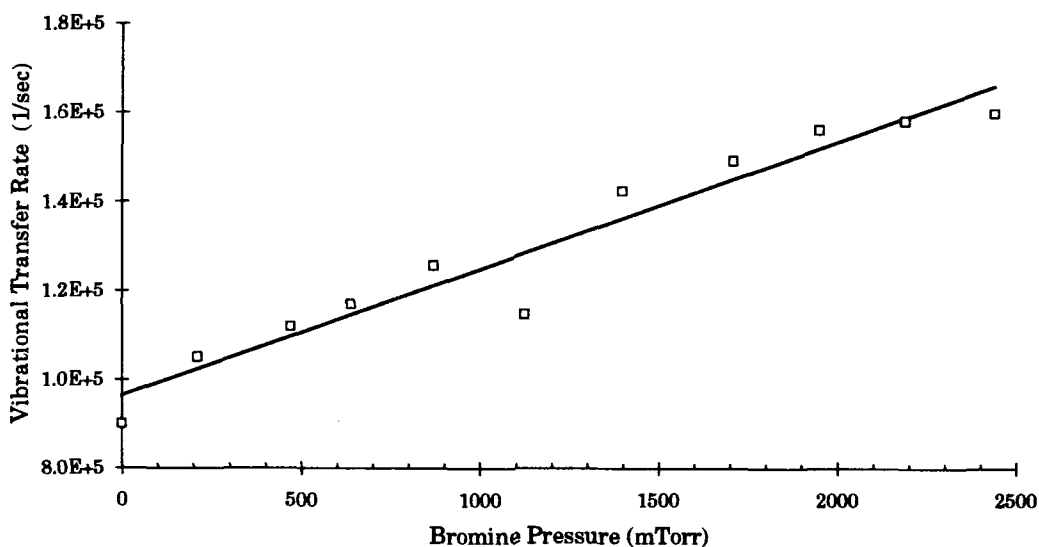


Figure D.10. Stern-Volmer plot of the Montroll-Shuler electronic quenching fits to the combined pump $v'=3$ view $v'=2$ data with Argon buffer gas $k_q = 9.3 (\pm 1.3) \times 10^{-12} \text{ cm}^3/\text{molec}\cdot\text{sec}$

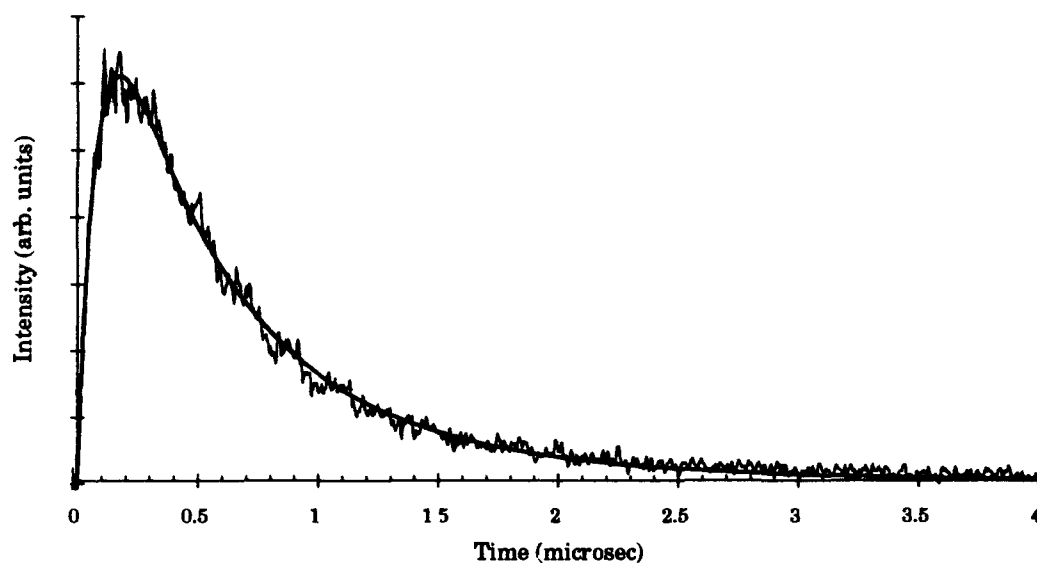


Figure D.11. Montroll-Shuler fit to emissions from the (2-11) band transition after initial excitation of $v' = 3$ with a Br_2 pressure of 650 mTorr and 560 mTorr of Helium

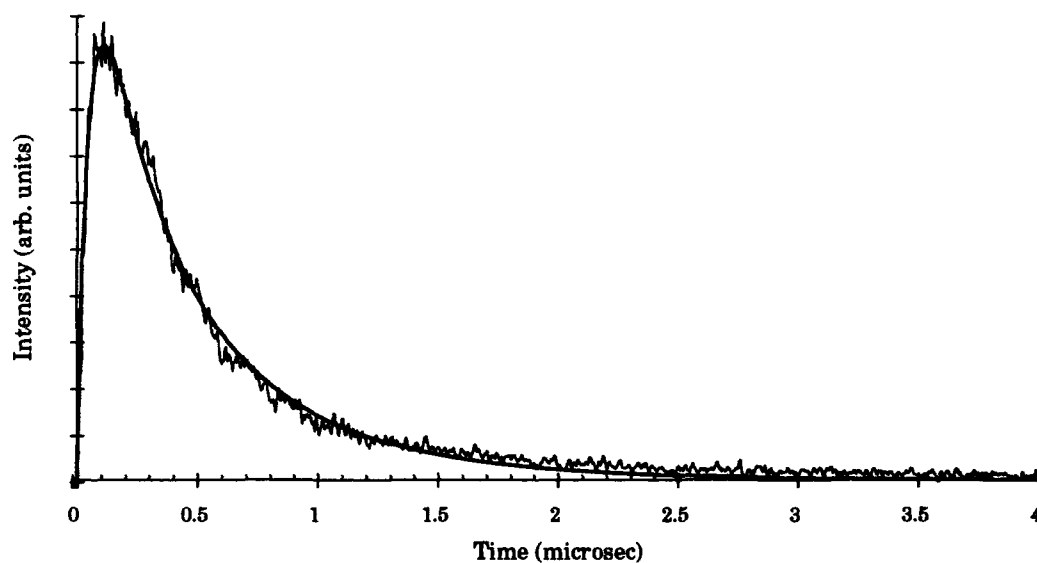


Figure D.12. Montroll-Shuler fit to emissions from the (2-11) band transition after initial excitation of $v' = 3$ with a Br_2 pressure of 650 mTorr and 2.1 Torr of Helium

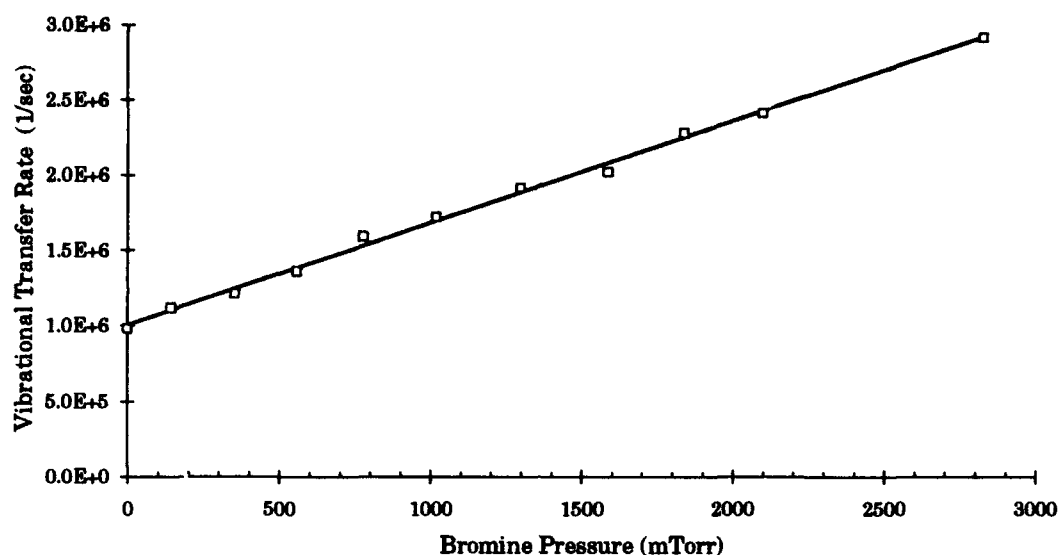


Figure D.13. Stern-Volmer plot of the Montroll-Shuler vibrational transfer fits to the combined pump $v' = 3$ view $v' = 2$ data with Helium buffer gas $k_v(1,0) = 2.5 (\pm 0.1) \times 10^{-11} \text{ cm}^3/\text{molec}\cdot\text{sec}$

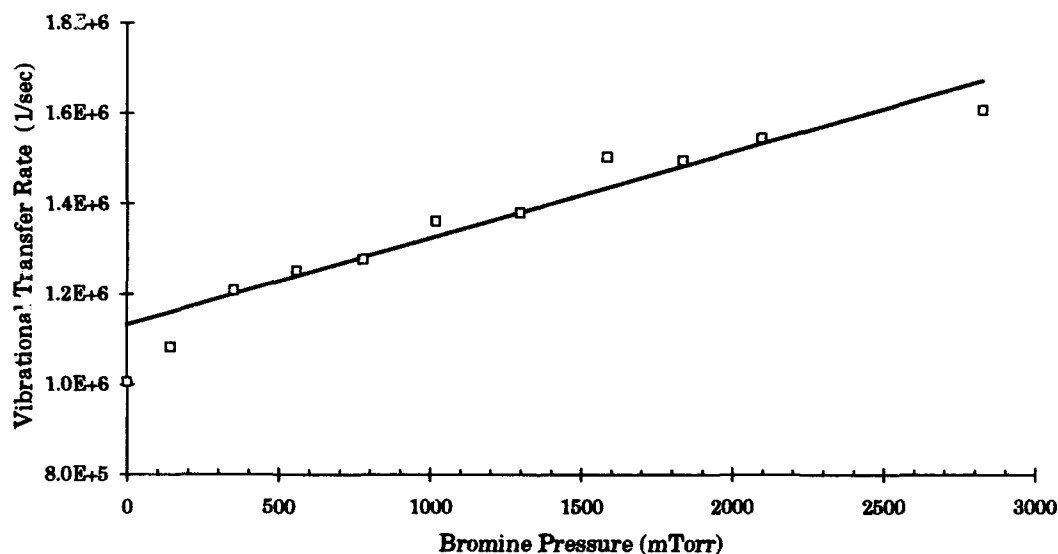


Figure D.14. Stern-Volmer plot of the Montroll-Shuler electronic quenching fits to the combined pump $v' = 3$ view $v' = 2$ data with Helium buffer gas $k_q = 7.1 (\pm 0.6) \times 10^{-12} \text{ cm}^3/\text{molec}\cdot\text{sec}$

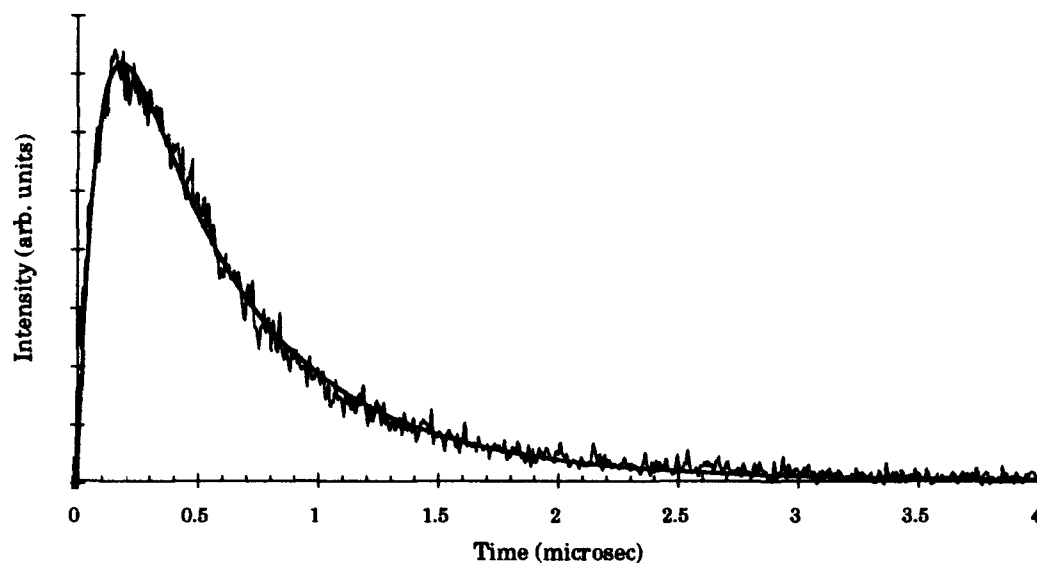


Figure D.15. Montroll-Shuler fit to emissions from the (2-11) band transition after initial excitation of $v' = 3$ with a Br_2 pressure of 700 mTorr and 360 mTorr of Neon

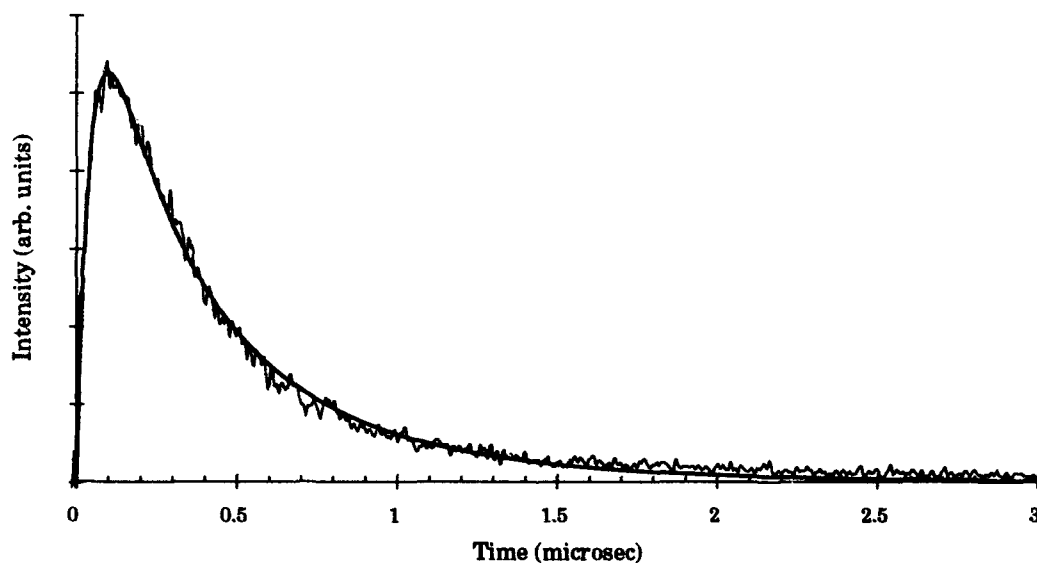


Figure D.16. Montroll-Shuler fit to emissions from the (2-11) band transition after initial excitation of $v' = 3$ with a Br_2 pressure of 700 mTorr and 2.4 Torr of Neon

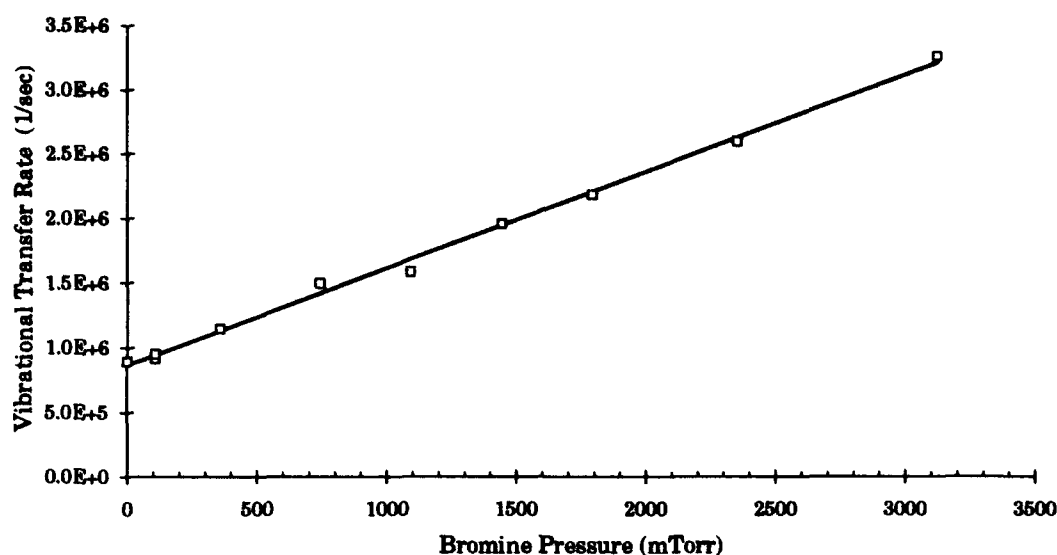


Figure D.17. Stern-Volmer plot of the Montroll-Shuler vibrational transfer fits to the combined pump $v' = 3$ view $v' = 2$ data with Neon buffer gas $k_v(1,0) = 2.8 (\pm 0.1) \times 10^{-11} \text{ cm}^3/\text{molec}\cdot\text{sec}$

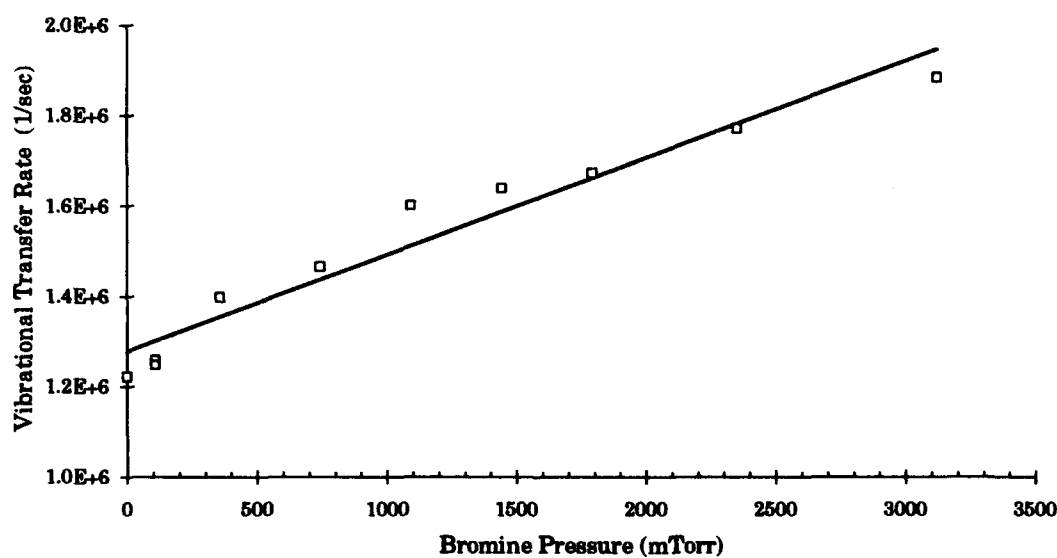


Figure D.18. Stern-Volmer plot of the Montroll-Shuler electronic quenching fits to the combined pump $v' = 3$ view $v' = 2$ data with Neon buffer gas $k_q = 7.9 (\pm 0.6) \times 10^{-12} \text{ cm}^3/\text{molec}\cdot\text{sec}$

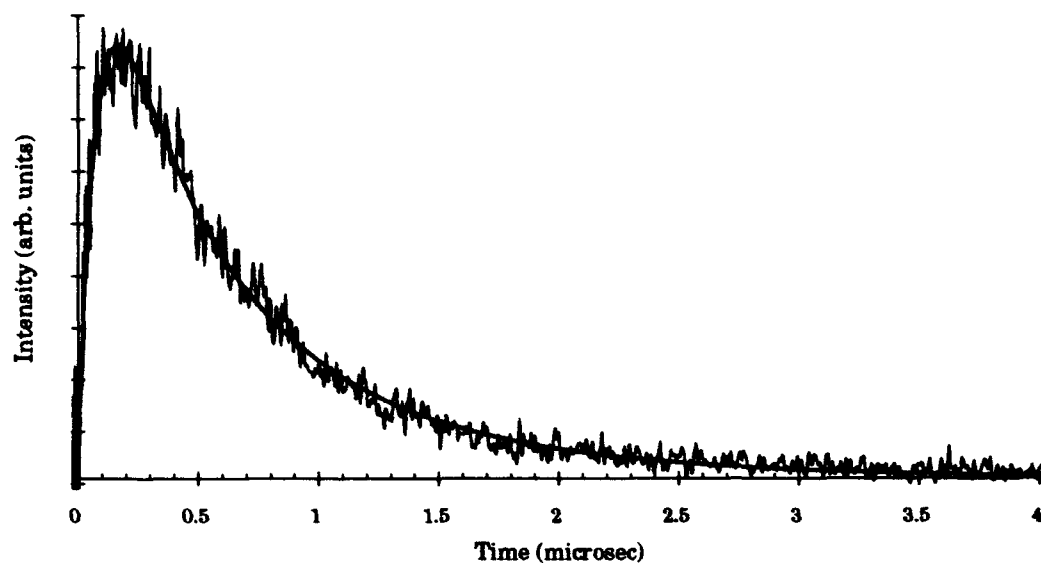


Figure D.19. Montroll-Shuler fit to emissions from the (2-11) band transition after initial excitation of $v' = 3$ with a Br_2 pressure of 640 mTorr and 410 mTorr of Krypton

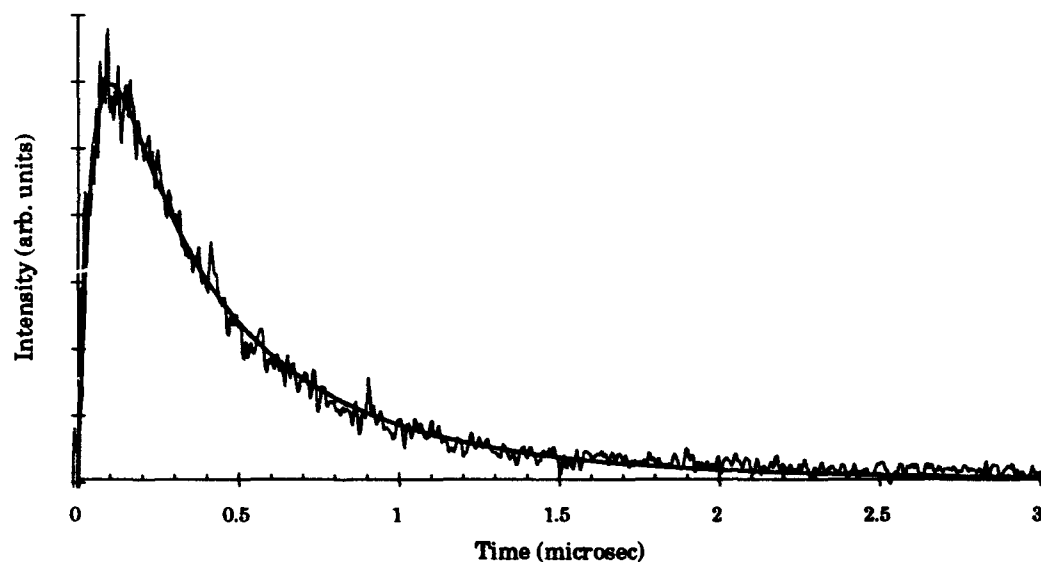


Figure D.20. Montroll-Shuler fit to emissions from the (2-11) band transition after initial excitation of $v' = 3$ with a Br_2 pressure of 640 mTorr and 2.3 Torr of Krypton

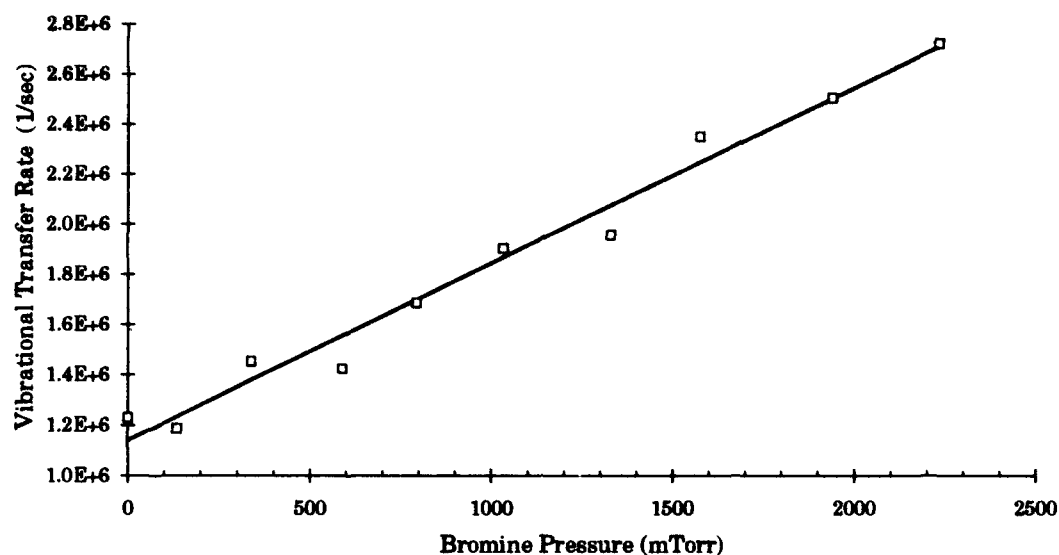


Figure D.21. Stern-Volmer plot of the Montroll-Shuler vibrational transfer fits to the combined pump $v' = 3$ view $v' = 2$ data with Krypton buffer gas $k_v(1,0) = 2.6 (\pm 0.1) \times 10^{-11} \text{ cm}^3/\text{molec}\cdot\text{sec}$

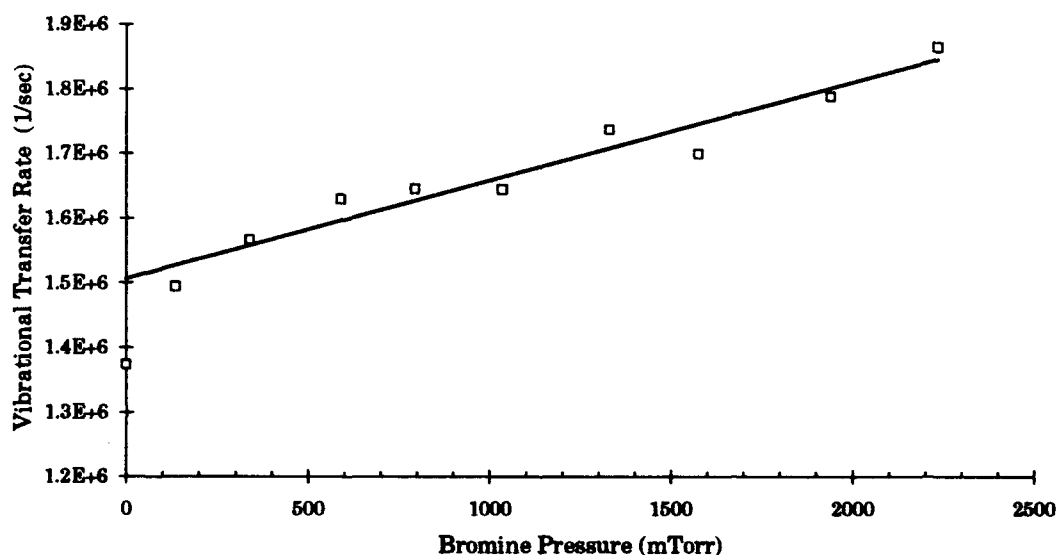


Figure D.22. Stern-Volmer plot of the Montroll-Shuler electronic quenching fits to the combined pump $v' = 3$ view $v' = 2$ data with Krypton buffer gas $k_q = 5.5 (\pm 0.5) \times 10^{-12} \text{ cm}^3/\text{molec}\cdot\text{sec}$

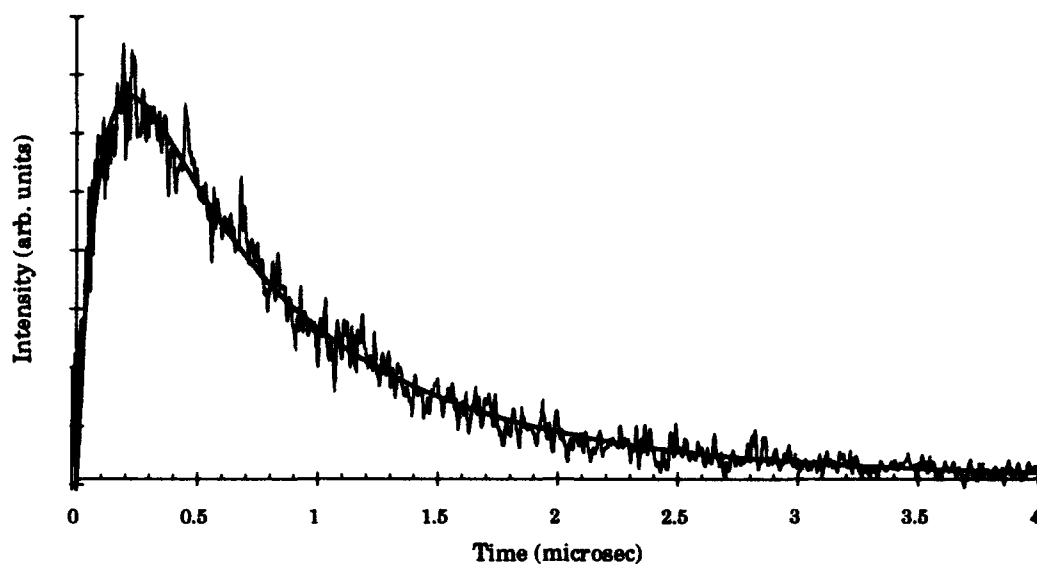


Figure D.23. Montroll-Shuler fit to emissions from the (2-11) band transition after initial excitation of $v' = 3$ with a Br_2 pressure of 420 mTorr and 500 mTorr of Xenon

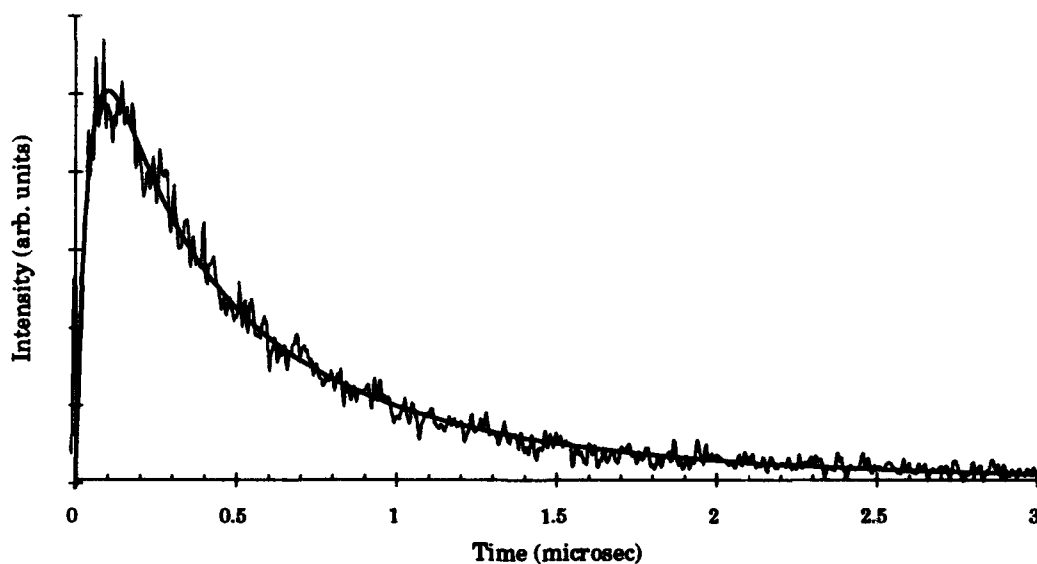


Figure D.24. Montroll-Shuler fit to emissions from the (2-11) band transition after initial excitation of $v' = 3$ with a Br_2 pressure of 420 mTorr and 2.3 Torr of Xenon

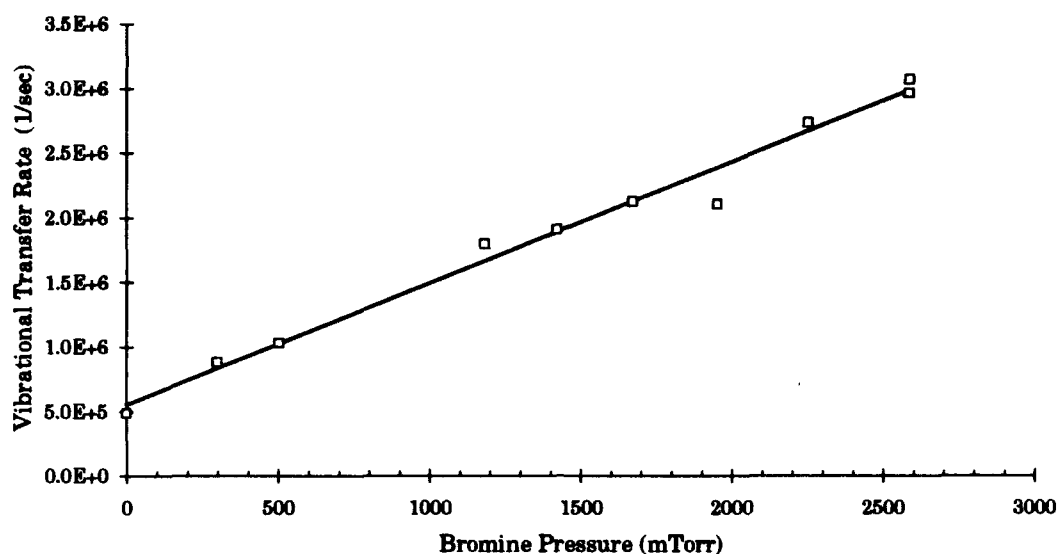


Figure D.25. Stern-Volmer plot of the Montroll-Shuler vibrational transfer fits to the combined pump $v' = 3$ view $v' = 2$ data with Xenon buffer gas $k_v(1,0) = 3.5 (\pm 0.2) \times 10^{-11} \text{ cm}^3/\text{molec}\cdot\text{sec}$

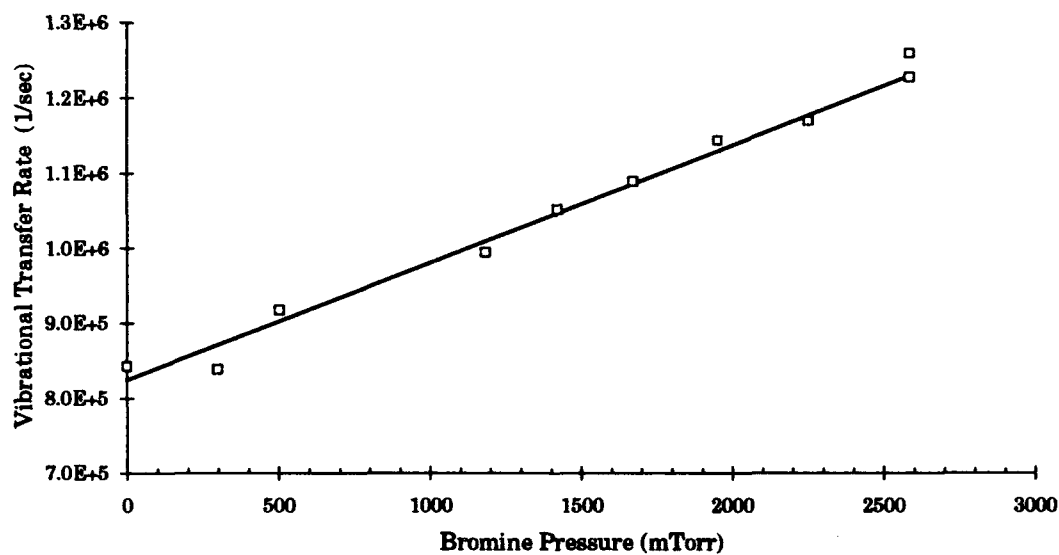


Figure D.26. Stern-Volmer plot of the Montroll-Shuler electronic quenching fits to the combined pump $v' = 3$ view $v' = 2$ data with Xenon buffer gas $k_q = 5.7 (\pm 0.3) \times 10^{-12} \text{ cm}^3/\text{molec}\cdot\text{sec}$

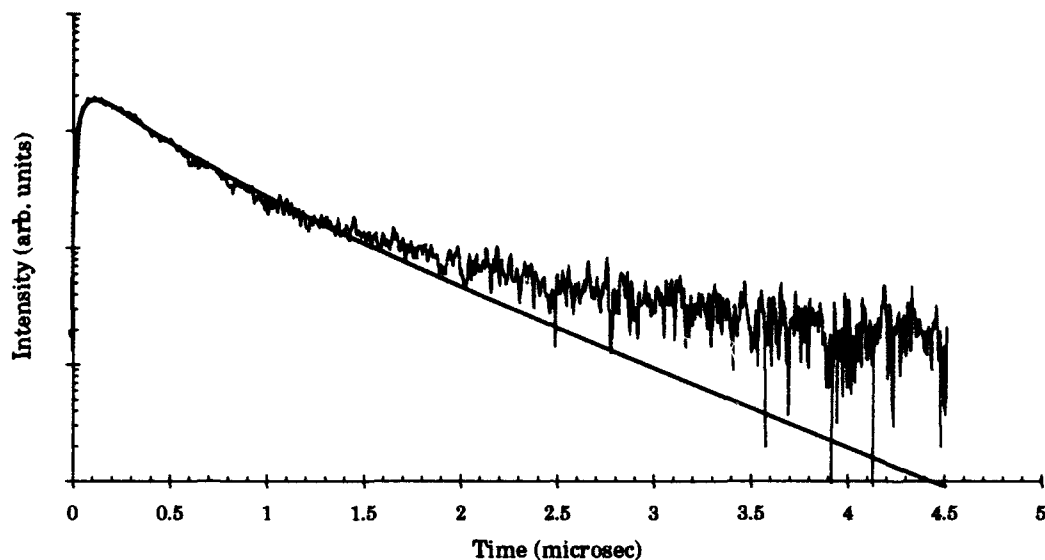


Figure D.27. Montroll-Shuler fit to emissions from the (2-11) band transition after initial excitation of $v' = 3$ with a Br_2 pressure of 650 mTorr and 2.1 Torr of Helium

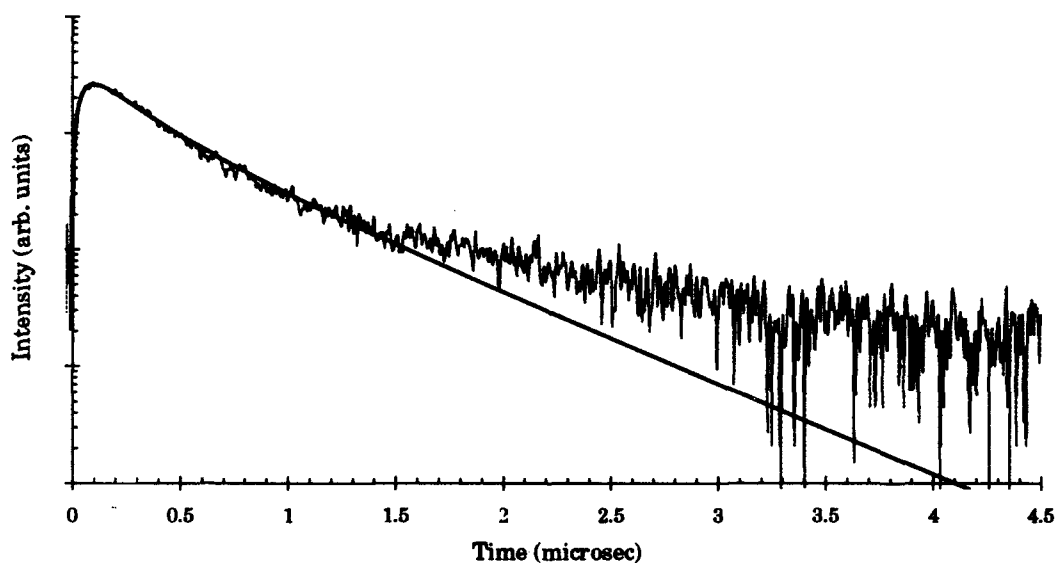


Figure D.28. Montroll-Shuler fit to emissions from the (2-11) band transition after initial excitation of $v' = 3$ with a Br_2 pressure of 700 mTorr and 2.4 Torr of Neon

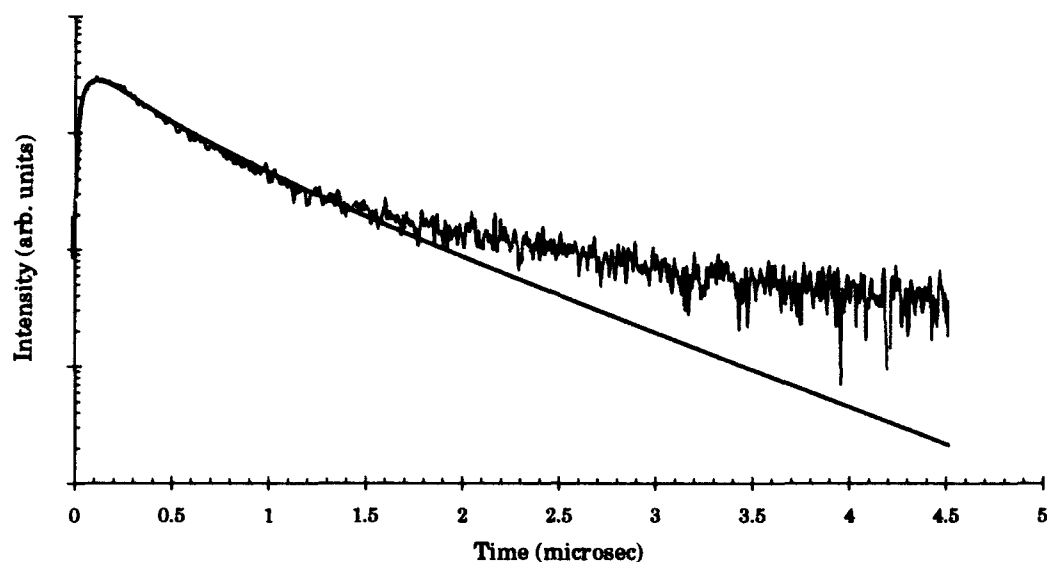


Figure D.29. Montroll-Shuler fit to emissions from the (2-11) band transition after initial excitation of $v'=3$ with 540 mTorr of Br_2 and 3.4 Torr of Argon

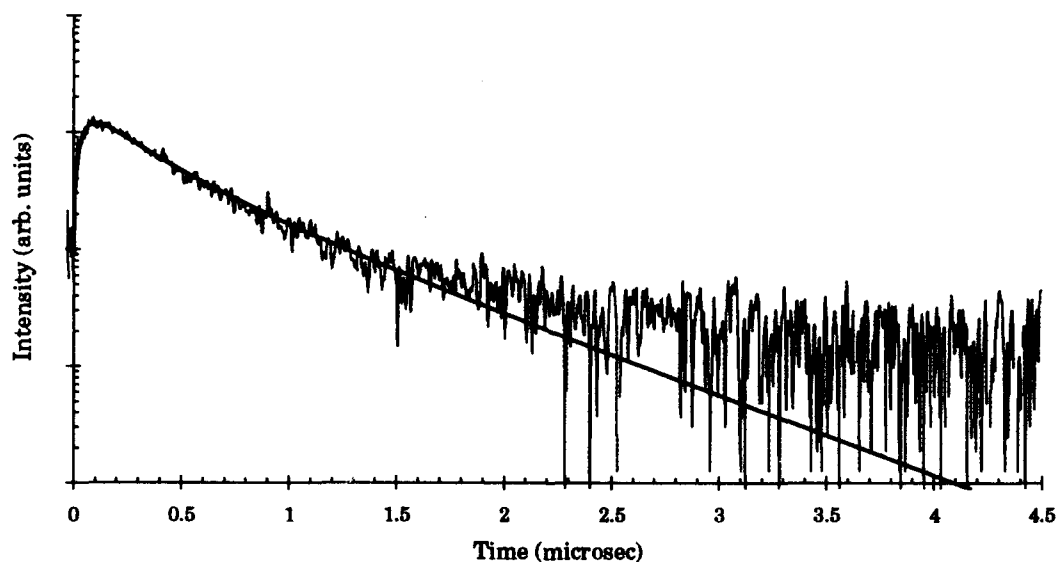


Figure D.30. Montroll-Shuler fit to emissions from the (2-11) band transition after initial excitation of $v' = 3$ with a Br_2 pressure of 640 mTorr and 2.3 Torr of Krypton

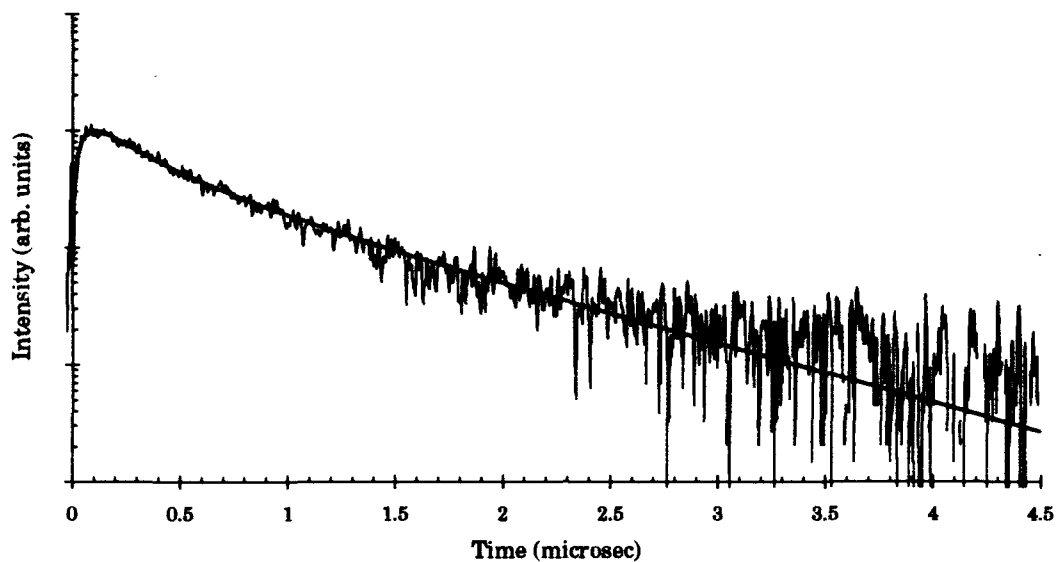


Figure D.31. Montroll-Shuler fit to emissions from the (2-11) band transition after initial excitation of $v' = 3$ with a Br_2 pressure of 420 mTorr and 2.3 Torr of Xenon

Appendix E. Systematic Error

The quoted errors for the molecular constants in chapter III are the standard deviations to the weighted least-squares fit of the three term Dunham polynomial to the second-difference ($\Delta G_v''$) plot in Figure 12. The errors are comparable to the uncertainty in obtaining exact line positions with the given monochromator resolution.

The quoted errors for rate coefficients in chapter IV for the $\text{Br}_2(\text{X})$ collision partner data are the standard deviations in the Stern-Volmer plots obtained from multiple combined data sets. Quoted errors for radiative lifetimes are the standard deviations to the zero pressure intercepts in the combined data sets Stern-Volmer plots for the electronic removal, Γ_0 . These values are obtained from rather long extrapolations and are probably subject to considerably greater error. For the rare gas collision partners, combining data sets was not possible because of differences in the partial pressure of Br_2 in the mix from data set to data set. The quoted errors for the rare gas collision partners are the standard deviations in the rates from Stern-Volmer plots determined for different data sets.

There are two primary sources of error in the vibrational transfer experiments. The first is the assumption that the vibrationally resolved fluorescence profiles were free from overlap from other vibrational levels. In general, overlaps were probably quite small, however, it is estimated that this could affect rate coefficients by $\approx 10\%$.

The second source of error results from assigning a $t = 0$ reference time to the individual waveforms. Typically, it is reasonable to assign $t = 0$ to

either the beginning of, the end of, or the peak of the laser pulse. With the current excitation system, that value could vary ≈ 20 nsec. However, because the rise times of the temporal profiles in the current data are fast, (typically ≤ 1.0 μ sec) a variation of 20 nsec in $t = 0$ can affect the rate coefficients by $\approx 10\%$. It also affects the intercept values of the Stern-Volmer plots as well. Considering both of these error sources, a total systematic error of 20% is estimated for all vibrational transfer and electronic quenching rate coefficients.

Vita

Captain Courtney D. Holmberg was born on August 18, 1959 in Clovis, New Mexico. He graduated from Lubbock High School in Lubbock, Texas in 1977. He was inducted into the USAF in October, 1979 and after attending technical training at Lowry AFB, Colorado, he was assigned to the 27th TFW at Cannon AFB, New Mexico in July, 1980. In January, 1982, he was selected for the Airman Education and Commissioning Program (AECPP) and attended Texas Tech University in Lubbock. He received his Bachelor of Science in Electrical Engineering, with high honors, in August, 1984. He was commissioned as a Second Lieutenant in the USAF in December, 1984 after completing Air Force Officer Training School as a distinguished graduate. He then returned to Texas Tech University and received a Master of Science degree in Electrical Engineering in December, 1986 through the Air Force Institute of Technology (AFIT) Civilian Institute Program. He was then assigned as an Electronic Warfare Flagging Engineer at the Air Force Electronic Warfare Center, Kelly AFB, Texas where he was responsible for computer modeling efforts to support reprogrammable aircraft electronic warfare systems. He married Connie Roten of Lubbock, Texas in 1978. They have two sons, Dustin, in 1980, Andrew, in 1982 and one daughter, Brianne, in 1986. Courtney entered the Ph.D. program at the AFIT in July, 1990 and was admitted to candidacy in 1992.

Permanent Address: 5227 17th St
Lubbock, Texas 79416

REPORT DOCUMENTATION PAGE			Form Approved GMB No. 0704 0188	
<small>THIS REPORT HAS BEEN REPRODUCED FROM THE BEST AVAILABLE COPY. IT IS THE PROPERTY OF THE NATIONAL ARCHIVES AND RECORDS SERVICE. IT IS LOANED TO YOU BY THE NATIONAL ARCHIVES AND RECORDS SERVICE. IT IS NOT TO BE REPRODUCED OR TRANSMITTED IN ANY FORM OR BY ANY MEANS, ELECTRONIC OR MECHANICAL, INCLUDING PHOTOCOPYING, RECORDING, OR BY ANY INFORMATION STORAGE AND RETRIEVAL SYSTEM, WITHOUT PERMISSION IN WRITING FROM THE NATIONAL ARCHIVES AND RECORDS SERVICE.</small>				
1. AGENCY USE ONLY (Leave blank)		2. REPORT DATE December 1993		3. REPORT TYPE AND DATES COVERED Doctoral Dissertation
4. TITLE AND SUBTITLE Spectroscopic and Vibrational Transfer Studies in Molecular Bromine				5. FUNDING NUMBERS
6. AUTHOR(S) Courtney D. Holmberg				
7. PERFORMING ORGANIZATION NAME(S) AND ADDRESS(ES) Air Force Institute of Technology, WPAFB, OH 45433-7765				8. PERFORMING ORGANIZATION REPORT NUMBER AFIT/DS/ENP-93-04
9. SPONSORING MONITORING AGENCY NAME(S) AND ADDRESS(ES) Dr. Ernest A. Dorko PL/LIDB (Bldg 618) Kirtland AFB, NM 87117-5776				10. SPONSORING MONITORING AGENCY REPORT NUMBER
11. SUPPLEMENTARY NOTES				
12a. DISTRIBUTION AVAILABILITY STATEMENT Approved for public release; distribution unlimited				12b. DISTRIBUTION CODE
13. ABSTRACT (Maximum 200 words) <p>Vibrational transfer and electronic quenching in the lower vibrational levels ($v' \leq 3$) of the $B^3\Pi(0_v^+)$ state of $^{79}\text{Br}_2$ were investigated using spectrally resolved, temporally resolved laser induced fluorescence techniques. Spectrally resolved emissions from collisionally populated $\text{Br}_2(\text{B})$ vibrational levels were observed for Br_2 and rare gas collision partners. Vibrational transfer was efficient in the non-predissociative vibrational levels and was adequately described by the Montroll-Shuler model for harmonic oscillators. A single fundamental rate coefficient for vibrational transfer from $v' = 1$ to $v' = 0$, $k_v(1,0)$, characterizes vibrational relaxation. For Br_2, the value was $k_v(1,0) = 3.6 \pm 0.4 \times 10^{-11} \text{ cm}^3/\text{molec-sec}$. For rare gas collisions, values ranged from $k_v(1,0) = 2.5 \pm 0.3 \times 10^{-11} \text{ cm}^3/\text{molec-sec}$ for helium to $k_v(1,0) = 3.1 \pm 0.4 \times 10^{-11} \text{ cm}^3/\text{molec-sec}$ for xenon. Electronic quenching rates for the observed vibrational levels were obtained from the same data. For Br_2, the quenching rate coefficient was $k_q = 3.7 \pm 1.2 \times 10^{-11} \text{ cm}^3/\text{molec-sec}$. Quenching rate coefficients for the rare gases were smaller, $k_q = 8.0 \pm 1.2 \times 10^{-12} \text{ cm}^3/\text{molec-sec}$. Additionally, the spectroscopy of high vibrational levels in the $^{79}\text{Br}^{81}\text{Br } X^1\Sigma_g^+$ ground electronic state was investigated using spectrally resolved, pulsed laser induced fluorescence from low J' levels in the $B^3\Pi(0_v^+)$ state. Over 100 bandheads were identified for transitions from $15 \leq v' \leq 21$ to $1 \leq v'' \leq 27$. The calculated spectroscopic constants, $\omega_e'' = 323.1 \pm 1.5 \text{ cm}^{-1}$, $\omega_e\chi_e'' = 1.02 \pm 0.1 \text{ cm}^{-1}$ and $\omega_e y_e'' = -3.77 \pm 0.2 \times 10^{-3} \text{ cm}^{-1}$, are valid for $v'' \leq 27$.</p>				
14. SUBJECT TERMS vibrational energy transfer, halogens, LIF, predissociation				15. NUMBER OF PAGES 174
				16. PRICE CODE
17. SECURITY CLASSIFICATION OF REPORT Unclassified		18. SECURITY CLASSIFICATION OF THIS PAGE Unclassified		19. SECURITY CLASSIFICATION OF ABSTRACT Unclassified
20. LIMITATION OF ABSTRACT				